Klemens Jantscher, BSc

Crystal structure determination in the scanning electron microscope: fundamental and experimental problems

MASTER THESIS

For obtaining the academic degree
Diplom-Ingenieur

Master Programme of
Advanced Materials Science

Graz University of Technology

Supervisor:

Univ.-Doz. Dipl.-Ing. Dr.techn. Peter Pölt

Institute of Electron Microscopy and Fine Structure Research

Graz, June 2011

Deutsche Fassung:
Beschluss der Curricula-Kommission für Bachelor-, Master- und Diplomstudien vom 10.11.2008
Genehmigung des Senates am 1.12.2008

EIDESSTATTLICHE ERKLÄRUNG

Ich erkläre an Eides statt, dass ich die vorliegende Arbeit selbstständig verfasst, andere als die angegebenen Quellen/Hilfsmittel nicht benutzt, und die den benutzten Quellen wörtlich und inhaltlich entnommene Stellen als solche kenntlich gemacht habe.

Graz, am …………………………… ………………………………………………..
(Unterschrift)

Englische Fassung:

STATUTORY DECLARATION

I declare that I have authored this thesis independently, that I have not used other than the declared sources / resources, and that I have explicitly marked all material which has been quoted either literally or by content from the used sources.

…………………………… ………………………………………………..
date (signature)

Abstract

Electron backscatter diffraction (EBSD) in a scanning electron microscope can on the one hand be used to identify different crystalline phases and on the other hand to determine the relative orientations of single crystallites - in a polycrystalline material - to each other or to a reference plane. In general this method is applied to analyze recrystallization processes, textures or grain size distributions in different materials.

In the present work both some basic experimental problems of the method and some problems of the data analysis were studied. Additionally, it was tried to fathom the limitations of EBSD using different materials and questions.

The exact positioning of the specimen surface in relation to the EBSD detector is an important experimental problem. It was shown, that already small inaccuracies of the specimen's alignment have a strong influence on the accuracy of the measured results.

The process of data analysis was studied focusing on grain size determination. The influence of fundamental, freely selectable parameters on the results of the measurement was investigated.

Using both mineral and metal particles, the influences of particle size and particle preparation on the quality of the diffraction patterns were investigated. Analyzable diffraction patterns could be recorded for particles with diameters as small as 60 nm.

Another part of this work focused on the investigation of micro-cracks in a partially recrystallized nickel based alloy. The goal was to find out whether or not the cracks always stop in recrystallized parts of the material. This required a serial sectioning method for large specimen areas which was developed, tested and successfully implemented. It could be shown, that 3D-representations of the grain structures gained with this method provide additional information which cannot be extracted from a single 2D measurement.

Kurzfassung

Mittels Elektronenbeugung im Rasterelektronenmikroskop (EBSD) können einerseits kristalline Phasen bestimmt und andererseits in einem polykristallinen Material zusätzlich die relativen Orientierungen einzelner Kristallite zueinander bzw. zu einer Referenzebene ermittelt werden. Häufig wird diese Methode für die Untersuchung von Rekristallisationsvorgängen, Texturbildung oder Korngrößenverteilungen bei verschiedenen Materialien genutzt. In der vorliegenden Arbeit wurden grundlegende experimentelle Probleme der Methode sowie der Datenauswertung studiert. Zusätzlich wurde versucht, die Grenzen von EBSD anhand verschiedener Materialien und Fragestellungen auszuloten.

Die exakte Positionierung der Probenoberfläche relativ zum EBSD-Detektor stellt ein wichtiges experimentelles Problem dar. Es wurde gezeigt, dass bereits geringfügige Fehler in der Ausrichtung der Probe einen starken Einfluss auf die Genauigkeit der Messergebnisse haben.

Im Prozess der Datenauswertung spielt die Korngrößenanalyse eine wesentliche Rolle. Daher wurde der Einfluss fundamentaler, frei variierbarer Parameter auf die Bestimmung der entsprechenden Kenngrößen untersucht.

Anhand von sowohl mineralischen als auch metallischen Teilchen wurden die Einflüsse der Größe und Vorbehandlung der Teilchen auf die Qualität der Beugungsbilder untersucht. Für Teilchen mit einem Durchmesser von 60 nm konnten noch verwertbare Beugungsbilder erzeugt werden.

Ein weiterer Teil der Arbeit beschäftigt sich mit der Untersuchung von Mikrorissen in einer teilweise rekristallisierten Nickelbasislegierung. Aufgeklärt werden soll, unter anderem, ob die Enden dieser Risse durchgehend in rekristallisiertem Material verlaufen. Dafür wurde eine für EBSD geeignete „Serial Sectioning" Methode entwickelt, getestet und erfolgreich eingesetzt. Es konnte gezeigt werden, dass mittels der damit gewonnenen 3D-Darstellungen Informationen gewonnen werden können, die aus einer einzelnen 2D Messung nicht extrahierbar sind.

Acknowledgments

I would like to thank the following people who all contributed to the realization of this master thesis:

Prof. Dipl. Ing. Dr. Ferdinand Hofer for making this master thesis possible and for giving me the chance to work in the field of electron microscopy.

Univ.-Doz. Dipl. Ing. Dr. Peter Pölt for supervising my master thesis and for always having an open door.

Dipl. Ing Dr. Stefan Mitsche for supervising the experimental part of my master thesis and for sharing his experience in electron microscopy.

Dipl. Ing. Herbert Reingruber for his help with the editing of images.

Margit Brunegger, Manuel Paller and Daniel Schreiner for teaching me the different methods of specimen preparation.

Prof. Dipl. Ing. Dr. Gernot Pottlacher, Prof. Dipl. Ing. Dr. Roland Würschum, Prof. Dipl. Ing. Dr. Christoph Sommitsch and Dipl. Ing. Dr. Petra Granitzer for providing specimens for my measurements.

My family and my girlfriend for their continuous support during my studies, especially during the final months of my master thesis.

Finally I would like to thank all members of the FELMI-ZFE team for providing a great working environment and for always being supportive.

Table of contents

Abstract ..... **i**
Kurzfassung ..... **ii**
Acknowledgments ..... **iii**
Table of contents ..... **iv**
List of symbols and abbreviations **1**
Motivation **2**
1 Fundamentals **4**
1.1 Electron backscatter diffraction 4
1.1.1 Backscattering from solid specimens 4
1.1.2 Hough transformation 8
1.2 Models for EBSD 10
1.2.1 Two-event diffraction model 10
1.2.2 Channeling in and channeling out model 11

2 Experimental methods **15**
2.1 EBSD 15
2.1.1 Equipment 15
2.1.2 Tilt and rotation of the specimen surface 18
2.1.3 Memory effect 23
2.1.4 Specimen surface preparation 25
2.2 Serial sectioning for 3D measurements 27
2.2.1 Development of the method 27
2.2.2 Testing the method 29
2.2.3 Accuracy 32

3 Grain size measurements: variation of step size, minimum misorientation angle and minimum number of points per grain **35**
3.1 Grain boundaries 35
3.1.1 Fundamentals 35
3.1.2 Measurements 36
3.1.3 Results and discussion 36
3.2 Step size 41
3.2.1 Fundamentals 41
3.2.2 Measurements 41
3.2.3 Results and discussion 42

4 Investigations of particles and bulk specimens **47**
4.1 EBSD measurements at small particles 47
4.1.1 Mineral particles 47
4.1.2 Nickel particles formed during wire explosions at different substrates 50
4.1.3 Nickel nanowires in a porous silicon matrix 58
4.2 EBSD measurements of high pressure torsion deformed nickel 63
4.2.1 Specimen 63
4.2.2 EBSD measurements 64
4.2.3 Results and discussion 65

4.3 Investigation of micro-cracks via 3D-EBSD 67
4.3.1 Specimen 67
4.3.2 Serial sectioning measurements 69
4.3.3 Results and discussion 70

5 Summary 76
6 Literature 79
Appendix 81

List of symbols and abbreviations

°C	Degrees Celsius
µm	Micrometres
3D	3 dimensional
at.%	Mole fraction
BSE	Backscattered electron
$CaCl_2$	Calcium chloride
$CaCO_3$	Calcium carbonate
cm	Centimetre
$CuSO_4$	Copper (II) sulfate
EBSD	Electron backscatter diffraction
EBSP	Electron backscatter diffraction pattern
ECP	Electron channelling diffraction pattern
EDXS	Energy dispersive X-ray spectroscopy
FIB	Focused ion beam
H_2O	Water
HAGB	High angle grain boundary
ICDD	International centre for diffraction data
IPF	Inverse pole figure
K_2SO_4	Potassium sulphate
keV	Kiloelectronvolt
kN	Kilonewton
LAGB	Low angle grain boundary
min	Minute
mm	Millimetre
nm	Nanometre
OIM	Orientation imaging microscopy
rpm	Rotations per minute
s	seconds
SEM	Scanning electron microscope
Si	Silicon
SiC	Silicon carbide
Z	Atomic number

Motivation

Electron backscatter diffraction (EBSD) in a scanning electron microscope (SEM) can be used on the one hand to identify different phases in an anorganic material and on the other hand to determine the orientations of single crystallites relative to each other in a polycrystalline material. The latter is called orientation imaging microscopy (OIM). This can, of course, also be used to determine grain size distributions or textures within a polycrystalline material. Contrary to other methods, e.g. x-ray diffraction, EBSD can be used to determine the orientations of specific grains and the relationships between neighboring grains (e.g. misorientations). The orientation spread within a single grain can provide information about the distribution of dislocations and mechanical stresses within this grain. The aim of this master thesis is to explore basic experimental problems and their influence on the accuracy of crystal orientation measurements as well as grain size measurements. Another goal is to fathom the limitations of the method based on measurements performed on different bulk materials and powders.

An important experimental problem is the exact positioning of the specimen surface relative to the phosphor screen on which the diffraction patterns are imaged. Experiments shall help to determine how small inaccuracies in the positioning (e.g. caused by an uneven specimen surface) affect the results of the orientation measurements and OIM mappings.

Grain size distributions in a polycrystalline material can be gained by etching a polished specimen surface. The etched structure then defines the grain boundaries. In an EBSD measurement there is no explicit definition of the grain boundaries. In general, a grain boundary is defined if the misorientation angle between two grains surpasses a certain more or less arbitrary selected value. The choice of this parameter will, of course, influence the measured grain size distribution. It will be investigated, how a variation of this minimum misorientation angle will affect the calculated size and number of the grains in the scanned area.

For the collection of an OIM map, the specimen surface is scanned with an electron beam. The step size between the single measurement points can also be chosen freely and therefore the value of this parameter will also affect the results of the measurements. By using a too large step size small grains will be missed and therefore

excluded from the analysis. On the other hand, a very small step size would cause long measurement times. One aim of this work was to find rules for an optimal choice of the step size.

Part of the experimental studies will focus on small particles. For such specimens, EBSD is primarily used to identify different phases. For particles within a matrix, their orientations can also be of interest, as they may influence material properties. Firstly, both mineral and metal particles will be investigated. Here the goal is to determine the influence of both the pretreatment and the size of the particles on the quality of the EBSD patterns. Secondly, the question whether nickel nanowires in a porous silicon matrix are mono- or polycrystalline will be solved.

Data gathered from an OIM map do not always give sufficient information about the three dimensional structure of certain details. Therefore, it is necessary to develop a serial sectioning method which is useable for large specimen areas. Subsequently this preparation method will be used for the investigation of micro-cracks within a partially recrystallized nickel based alloy.

1 Fundamentals

1.1 Electron backscatter diffraction

1.1.1 Backscattering from solid specimens

When an electron beam hits a specimen, part of the electrons experience a few elastic scattering events and leave the specimen again. During this process they lose only a small fraction of their primary energy. This kind of scattering is called backscattering and the fraction of primary electrons scattered this way is described by the backscattering coefficient η. The backscattering coefficient is strongly connected to the average atomic number Z in the specimen, the specimen tilt angle φ and the electron energy E.

Figure 1-1 shows the relationship between the backscattering coefficient and the atomic number at different specimen tilt angles.

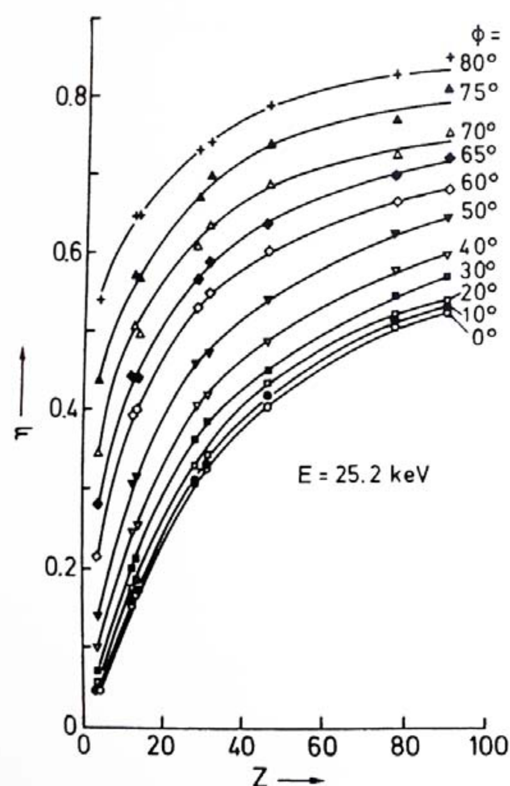

Figure 1-1: Backscattering coefficient η in dependence on the atomic number Z and the tilt angle φ (φ= 0: normal incidence). [1]

This relation is also described by an empiric formula (1-1).

$$\eta(Z,\varphi) = (1+\cos(\varphi))^{-9/\sqrt{Z}} \tag{1-1}$$

η... **backscattering coefficient**

Z... **average atomic number of the specimen**

φ... **tilt angle**

It is obvious that materials with higher atomic numbers have a higher backscattering coefficient. For multi component materials the backscattering coefficient can be calculated using equation (1-2).

$$\eta = \sum_i c_i \cdot \eta_i \tag{1-2}$$

η... **average backscattering coefficient**

c_i... **component's mass fraction**

η_i... **component's backscattering coefficient**

Figure 1-2 shows the relation between the backscattering coefficient η and the electron energy E.

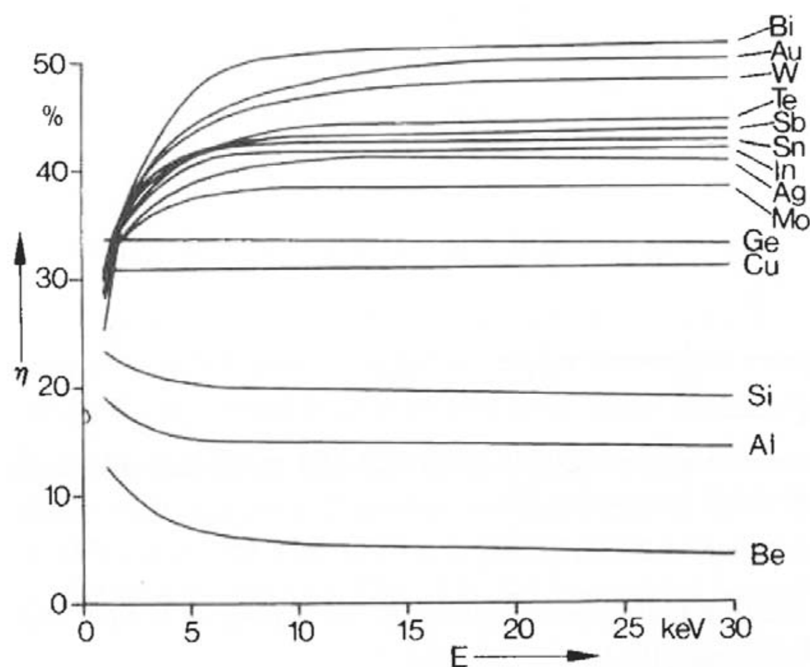

Figure 1-2: Backscattering coefficient η in dependence on the electron energy E. [1]

For energies greater than 5 keV the backscattering coefficient is approximately constant. Below this energy it increases for elements with a low atomic number and decreases for

elements with a high atomic number. This behavior is due to cross-section properties and simulations show that at lower energies Mott cross-sections have to be used for the calculation of η rather than Rutherford cross-sections.

Regarding these factors, the tilt angle remains as a very important parameter for the backscattering coefficient. The electron energy has no significant influence at higher voltages and the specimen chemistry is usually given.

Figure 1-3 illustrates the angular distribution of backscattered electrons for normal incidence (a – 0°) and oblique incidence (b – 60°, c – 80°).

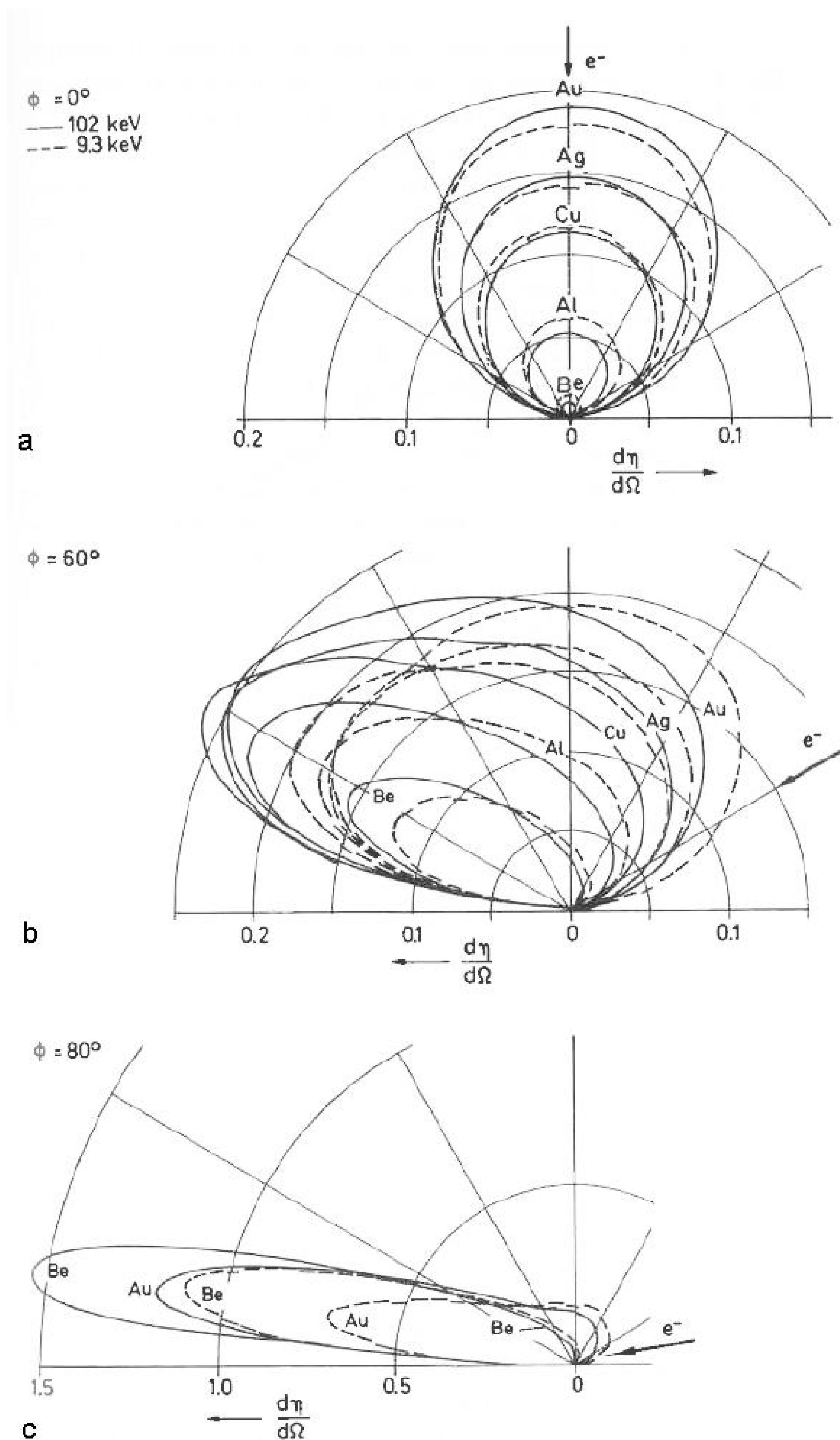

Figure 1-3: Polar diagrams of the angular distribution of backscattering for increasing tilt angles: (a) normal incident 0°, (b) oblique incident 60° and (c) oblique incident 80°; solid line – E=100 keV, dashed line – E=9.3 keV. [1]

The distribution consists of two parts. Firstly there are diffusely scattered electrons. They undergo many inelastic scatterings and lose a high amount of their primary energy. When they finally leave the specimen, they can come from regions deep within the specimen. Secondly there are the backscattered electrons which come from smaller depths and escape after a few elastic scattering events.

The fraction of electrons that is diffusely scattered is nearly constant for tilt angles below 60°. If the tilt angle is chosen bigger, it decreases. For these angles the fraction of backscattered electrons outweighs the fraction of diffusely scattered electrons. These backscattered electrons with an energy close to the primary electron energy generate the diffraction patterns used in EBSD. Figure 1-3 demonstrates that they are strongly peaked in a forward direction for a specimen tilt angle of 80°, similar to the reflection of light. This is the reason why samples are tilted strongly for EBSD measurements because then most of the backscattered electrons hit the phosphor screen used for imaging the EBSD pattern. In case of normal incidence much higher probe currents would be necessary to get analyzable diffraction patterns. [1]

1.1.2 Hough transformation

The Hough transformation is a method used to recognize circles, lines or other geometric figures within a black and white image. The simplest Hough transformation is used for detecting lines and therefore is a useful tool for the analysis of Kikuchi patterns. An example for such a Kikuchi pattern is given in Figure 1-4.

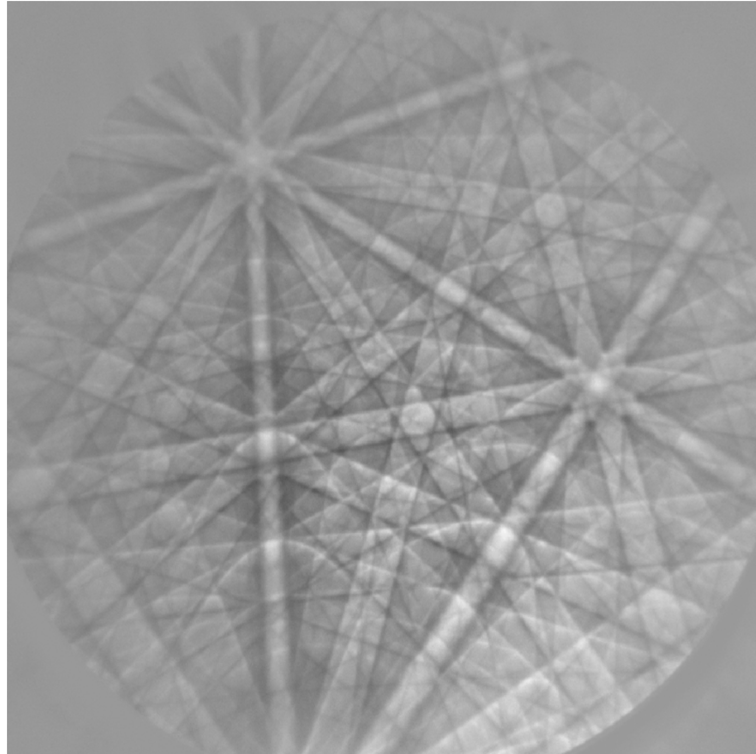

Figure 1-4: Kikuchi pattern of a nickel standard.

The linear Hough transformation defines every possible line that can be drawn through a point in the image by two Hough parameters: ρ and Θ. ρ is the line's perpendicular

distance from the origin point and Θ is the angle of the corresponding vector (Figure 1-5).

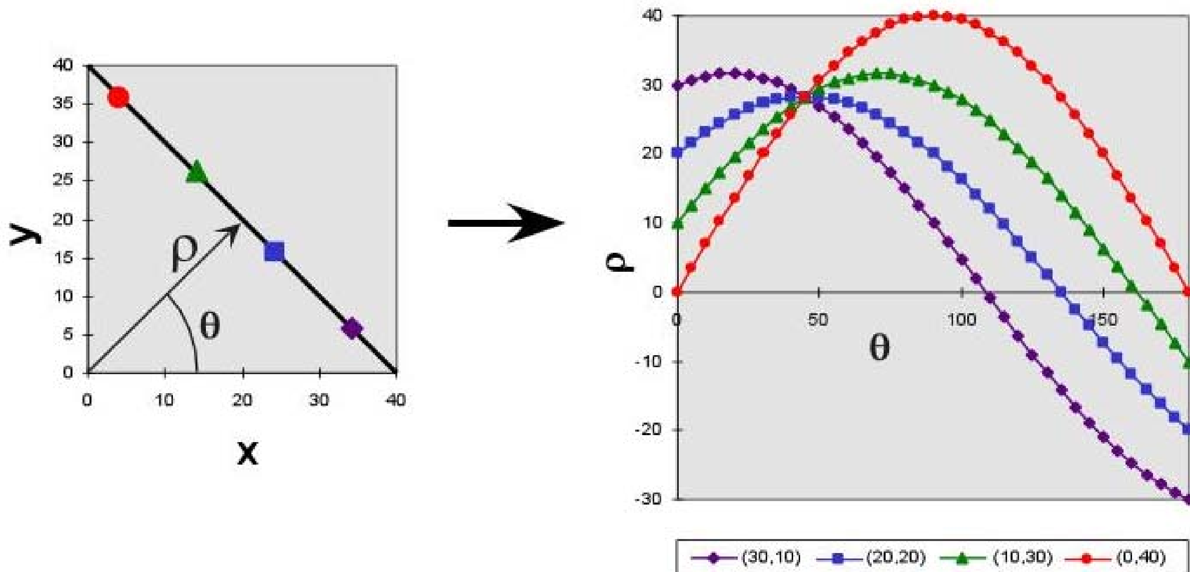

Figure 1-5: Hough transformation of a line. [2]

Subsequently the number of intersecting lines at every pixel in the Hough space is summed up and the respective value is plotted as a grey value in a chart (Figure 1-6) at the corresponding ρ and Θ values. Thus, a line in the original image transforms to a point in Hough space.

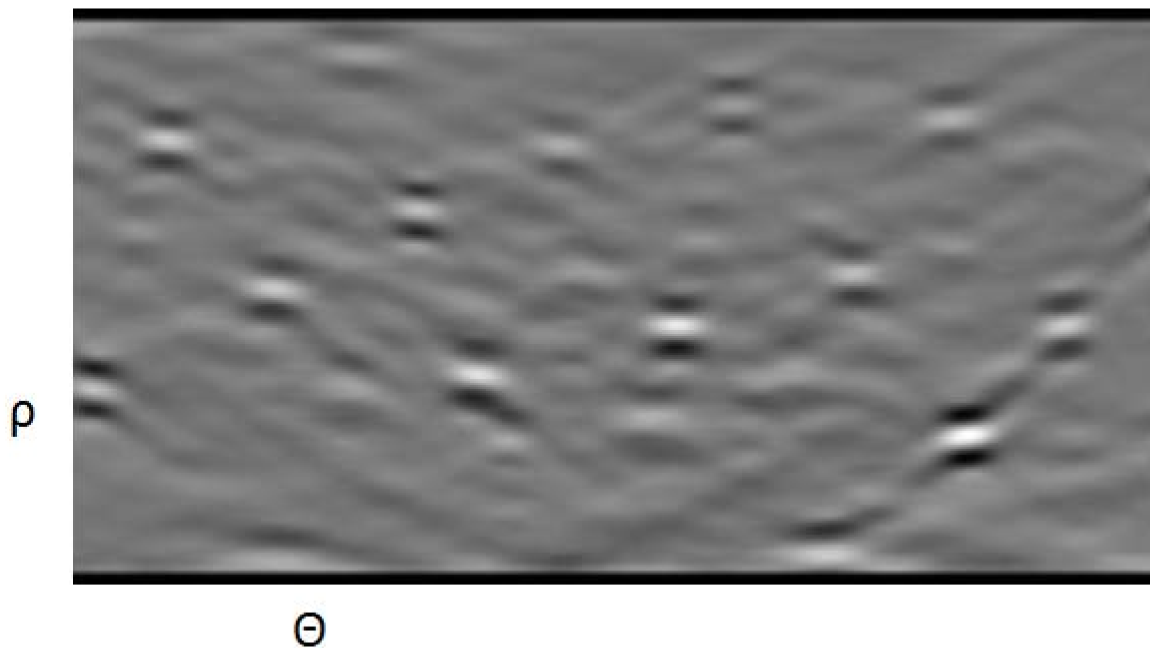

Figure 1-6: Hough transformation of the Kikuchi pattern of nickel shown in Figure 1-4.

A Kikuchi pattern is not strictly made up of lines but of high intensity bands bordered by two low intensity bands. Therefore each peak is bordered by two valleys in ρ direction. They can be located using image recognition software. Usually 7 to 12 Hough peaks are used to index a Kikuchi pattern.

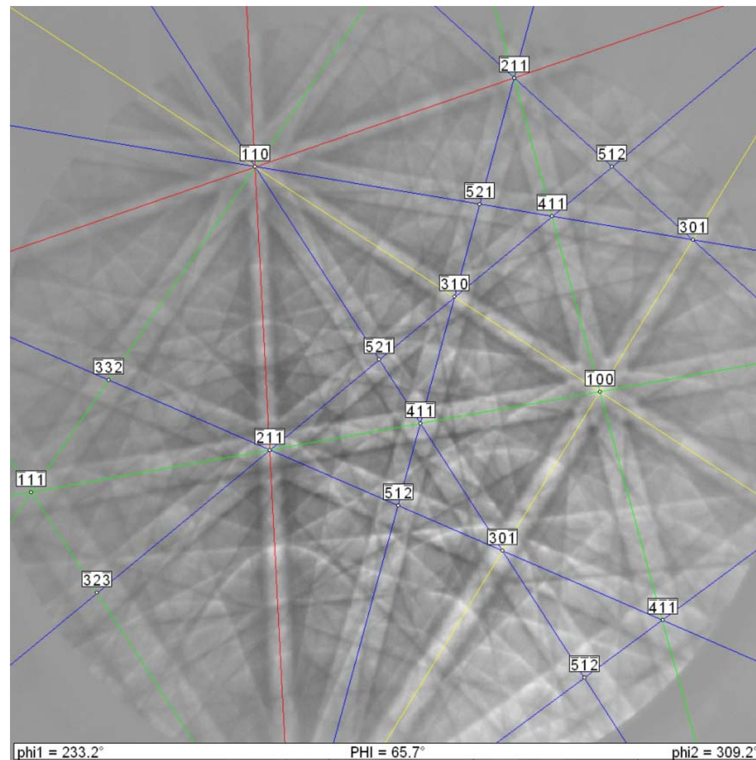

Figure 1-7: Indexed Kikuchi pattern of nickel.

1.2 Models for EBSD

1.2.1 Two-event diffraction model

In this model the electrons enter the crystal and experience several scattering events after which they have a diffuse spatial distribution. They do not necessarily lose energy although some of them do. For every lattice plane some of these diffusely scattered electrons will fulfill Bragg's law. These electrons are diffracted on the surfaces of two cones – the Kossel cone (see Figure 1-8).

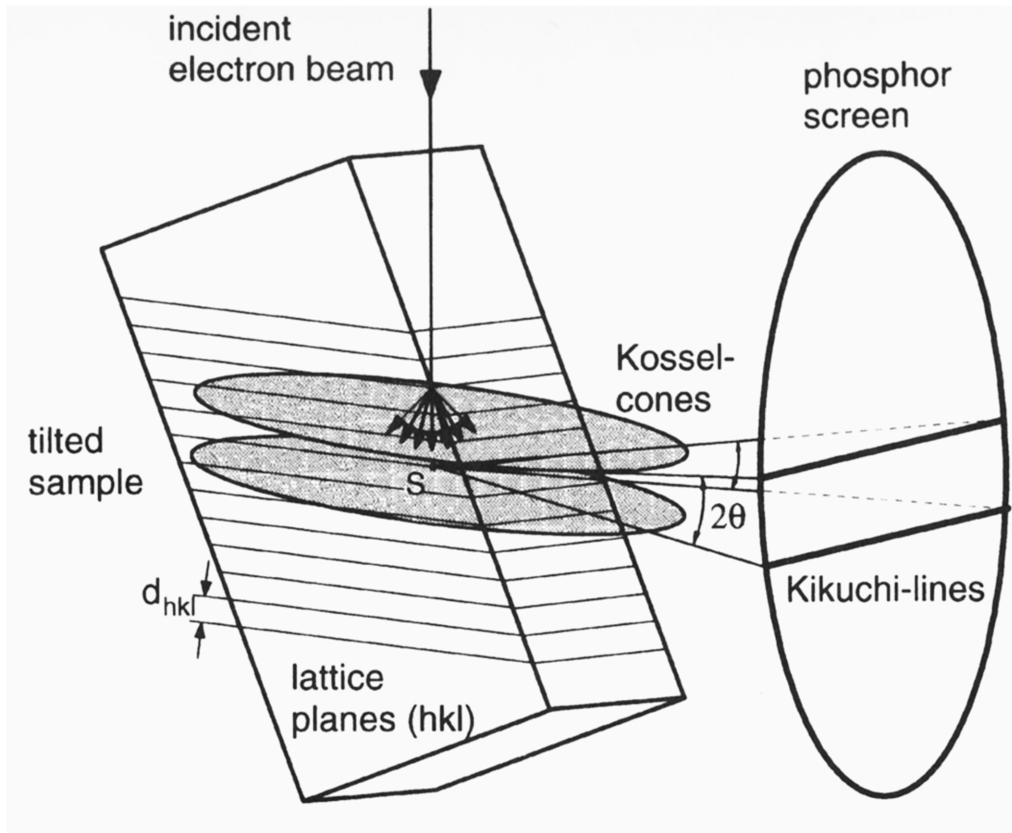

Figure 1-8: Origin of Kikuchi lines according to the two-event diffraction model. [3]

What is visible as Kikuchi bands are the intersections of different pairs of Kossel cones with the detector screen. Due to small Bragg angles (~0.5 degrees) the angles of the cones are close to 90° and therefore the bands appear to be lines rather than parabolas. [3][4][5]

1.2.2 Channeling in and channeling out model

Electron backscatter diffraction patterns (EBSP) have a very similar appearance to electron channeling diffraction patterns (ECP). For the creation of EBSPs the electron beam is stationary and the pattern is the angular distribution of the backscatter profile. For ECPs the angle of the incident electron beam is varied and the correlation between this angle and the backscattering yield composes the diffraction pattern (Figure 1-9).

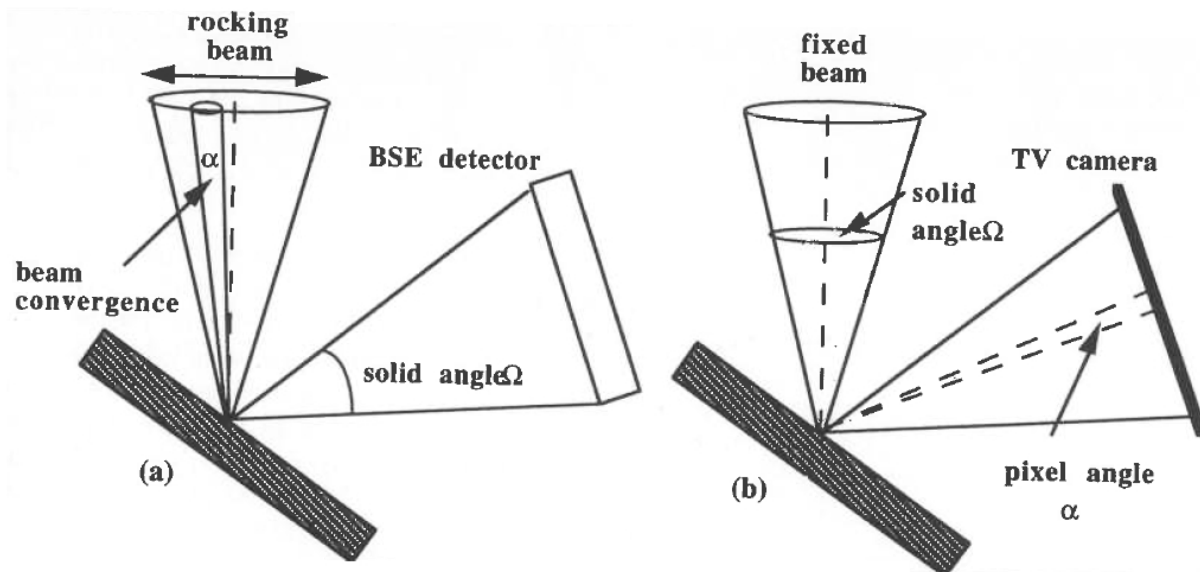

Figure 1-9: Principal methods for the creation of (a) electron channeling patterns and (b) electron backscatter diffraction patterns.[6]

These two mechanisms seem to be very different but it can be argued that the only difference between them is the direction in which the electrons pass through the specimen. This assumption is called the principle of reciprocity and if it is accurate the mechanisms that create both kinds of diffraction patterns should be the same. The two-event diffraction model mentioned previously fails the demanded reciprocity as a path for the electrons reversing the diffuse scattering seems unlikely. A different model called the channeling in and channeling out model is needed which explains ECPs. Here it is assumed that the two diffraction events described in 1.2.1 are related very closely and form a wide angle scattering event. The probability for these wide angle scattering events is assumed to be modulated by channeling processes (see Figure 1-10).

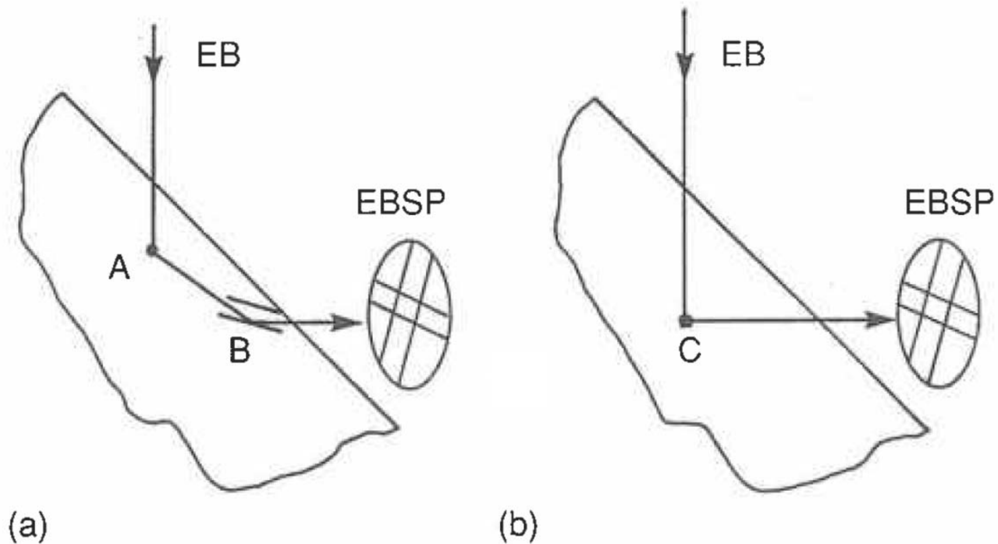

Figure 1-10: (a) Schematic for the two-event diffraction model with A = wide angle scattering event and B = Bragg diffraction; (b) schematic for the channeling in and channeling out model with C = wide angle scattering event modulated by the channeling processes. [7]

These channeling processes can be explained in terms of Bloch waves.

A plane electron wave incident on a crystal can be split up in two Bloch waves, type-1 and type-2 (Figure 1-11). These Bloch waves move parallel to the Bragg planes if the direction of the incident beam is close to the Bragg angle. This is called channeling.

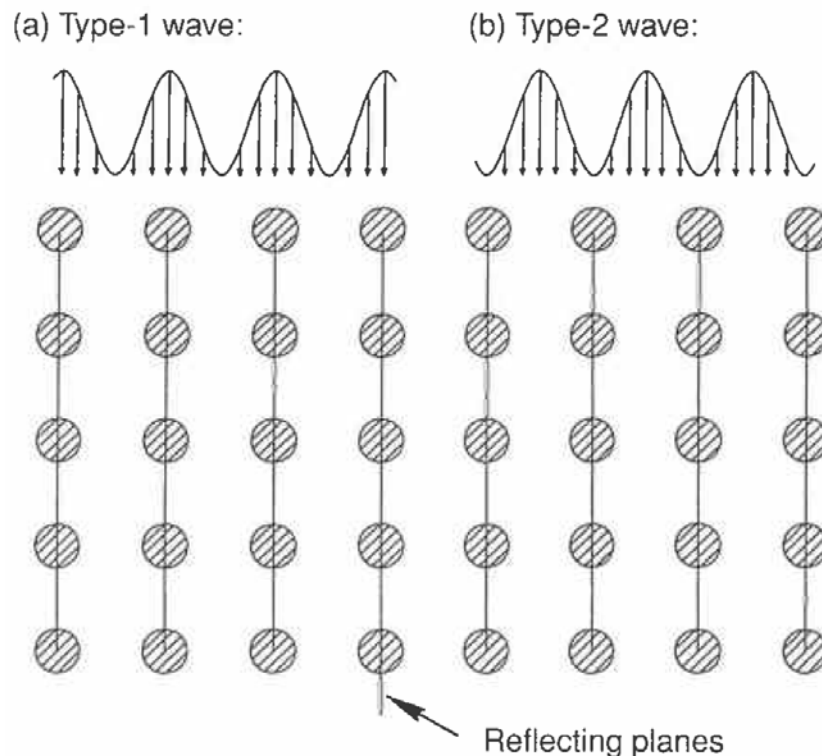

Figure 1-11: (a) Type-1 and (b) type-2 Bloch wave intensities in a simple cubic lattice. [7]

The amplitudes of the Bloch waves represent the probability to find electrons in the respective region. For type-2 Bloch waves the electrons are primarily located between lattice planes whereas for type-1 Bloch waves they are more likely to be found at the lattice planes and therefore very close to the atomic nuclei. As backscattering occurs when an electron passes by closely to a nucleus, the electrons in the type-1 Bloch wave are more likely to be backscattered. The total intensity of both Bloch waves is constant so the backscattering yield depends on the ratio between the amplitudes of both Bloch waves. This ratio is linked to the incident angle of the electron beam. If the incident angle equals the Bragg angle, both waves have the same amplitude. For smaller angles the type-1 Bloch wave has a higher intensity and therefore the backscattering yield is high as well. For angles bigger than the Bragg angle it's the opposite. This dependence between the incident angle and the amount of backscattered electrons produces the electron channeling patterns. The channeling process controls the backscattering and therefore both effects are connected and can be viewed as one. The creation of EBSPs works the same way but here the electrons pass through the specimen in the opposite direction. [6] [7]

2 Experimental methods

2.1 EBSD

2.1.1 Equipment

Assembly and EBSD detector

For the experiments an Ultra 55 SEM manufactured by Zeiss was used. Standard detectors for secondary electrons and backscatter electrons are integrated. The Ultra 55 is also equipped with an EBSD detector from EDAX – the TSL Digiview (generation 2) with an integrated forward scatter detector. The specimen chamber of the Ultra 55 can be seen in Figure 2-1.

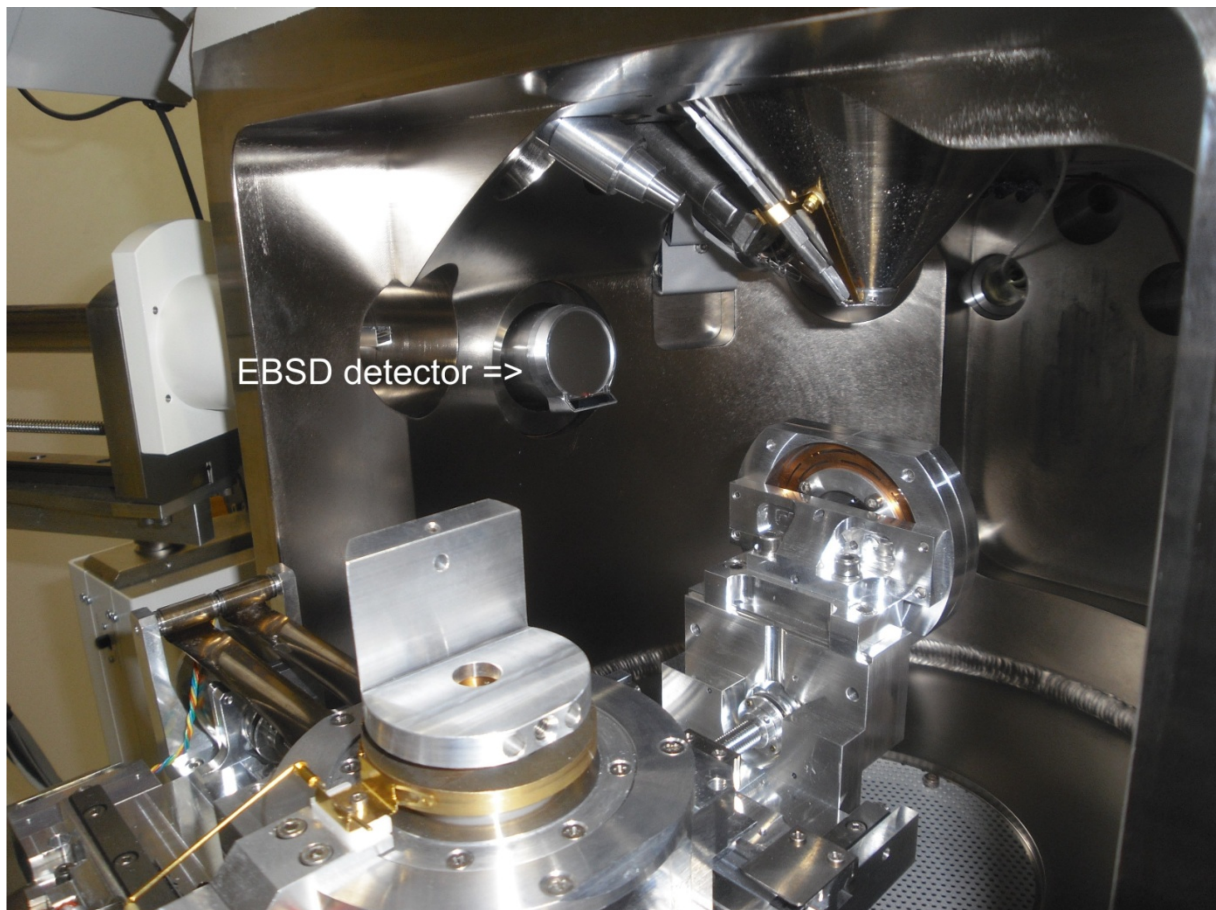

Figure 2-1: Specimen chamber of the Zeiss Ultra 55.

Figure 2-2 shows a schematic of the configuration for the recording of EBSD patterns.

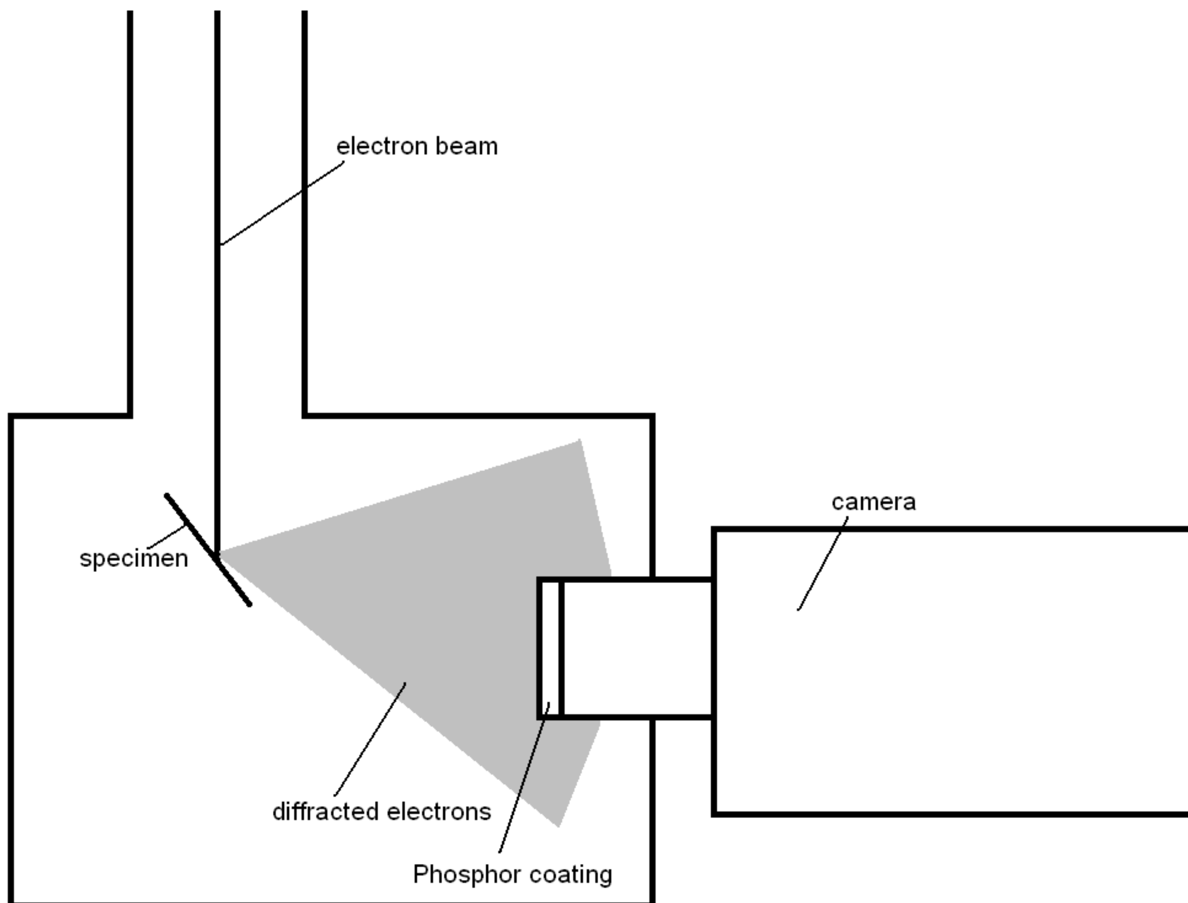

Figure 2-2: Schematic of the configuration of an EBSD measurement system.[2]

When the electron beam hits a point on the specimen surface, the electrons are scattered and form a Kikuchi pattern which can be detected by a phosphor screen. This pattern is then recorded by the camera and analyzed using the Hough transformation. The result of the analysis is the crystal orientation in relation to the polished specimen surface. Subsequently, grain size distributions, textures and many other material parameters can be calculated for a polycrystalline material. If the chemical composition of the material is known (can be analysed by EDXS in the SEM), its phase can be determined. Data bases like ICDD (international center for diffraction data) are generally used for this purpose.

OIM mapping and inverse pole figure

During an OIM mapping the electron beam scans across a selected area and for every measurement point within this area the crystal orientation in relation to the polished specimen surface is determined. The orientation distribution at the specimen surface can be displayed in an inverse pole figure in which the orientation values are depicted by colors. An inverse pole figure shows the position of a sample direction relative to the

crystal reference frame. Each pixel in the mapping represents one measurement point and its size depends on the step size between two measurement points. The TSL data collection software offers a choice between two possible measurement grids: square grids and hexagonal grids. Figure 2-3 shows the inverse pole figures of a ferrite specimen using both grids. The number of measurement points was chosen thus low that the difference in the representation of the grains by use of the two grids becomes visible.

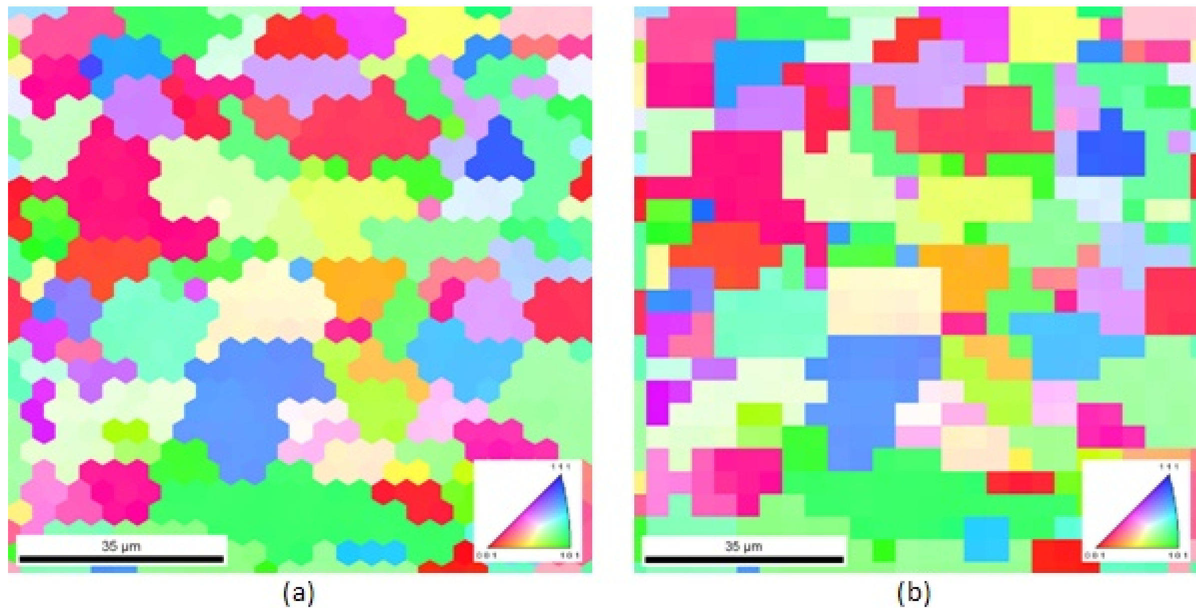

Figure 2-3: Inverse pole figure maps of ferrite recorded with a step size of 4.0 µm and (a) hexagonal grid, (b) square grid; inset: color code for crystal orientations.

In the hexagonal grid every measurement point has six nearest neighbors whereas in the square grid every measurement point has only four nearest neighbors. Because of this, the description of the shapes of the grains works better with the hexagonal grid and it is therefore preferred over the square grid. [2]

Clean up: grain dilation

Sometimes, the TSL software is not able to analyze a diffraction pattern correctly. Reasons can be a superposition of two diffraction patterns recorded at measurement points close to grain boundaries or a bad diffraction pattern due to scratches or contaminations on the specimen surface. The clean up process attempts to correct the erroneous data. For some measurements in this thesis a clean-up-method called “grain dilation” was used. This method is an iterative one but only a single iteration was used. It targets points which do not belong to grains but have neighboring points that do. If the majority of the neighboring points have a similar orientation (same grain), the

orientation value of the targeted point is changed to the orientation value of those points. If there is no majority, the targeted point's orientation is changed randomly to one of the neighbors' orientations. If the method is not stopped after some iteration steps, it continues until every point of the dataset belongs to a grain. Figure 2-4 shows a schematic of the "grain dilation" method. [2]

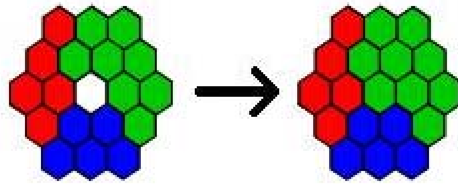

Figure 2-4: Schematic depiction of the "grain dilation" clean up method. [2]

Specimen holder

As mentioned in chapter 1, a tilt angle of the specimen surface of 70° is generally used for EBSD measurements. The Ultra 55 is equipped with a special specimen holder (Figure 2-5). Samples fixed in this holder are automatically tilted by 70°. This has the advantage that a tilt of the specimen stage itself is not necessary.

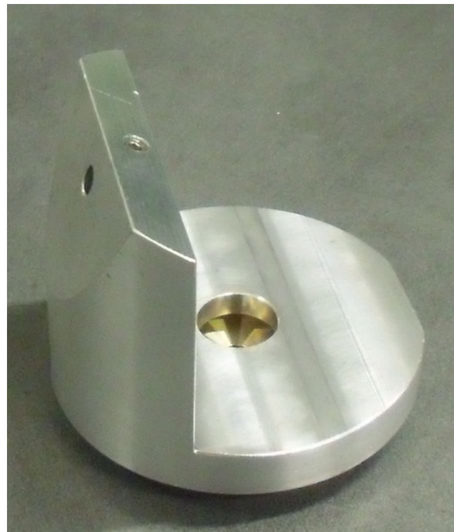

Figure 2-5: EBSD sample holder.

2.1.2 Tilt and rotation of the specimen surface

For EBSD measurements the specimen has to be positioned in such a way that its surface would be parallel to the detector surface if tilted to a corresponding angle. This can be performed by rotating the stage. Before the start of the measurements the correct angle was determined as 14°. This way a horizontal line on the specimen surface should be parallel to the EBSD detector. Figure 2-6 shows a schematic of the assembly.

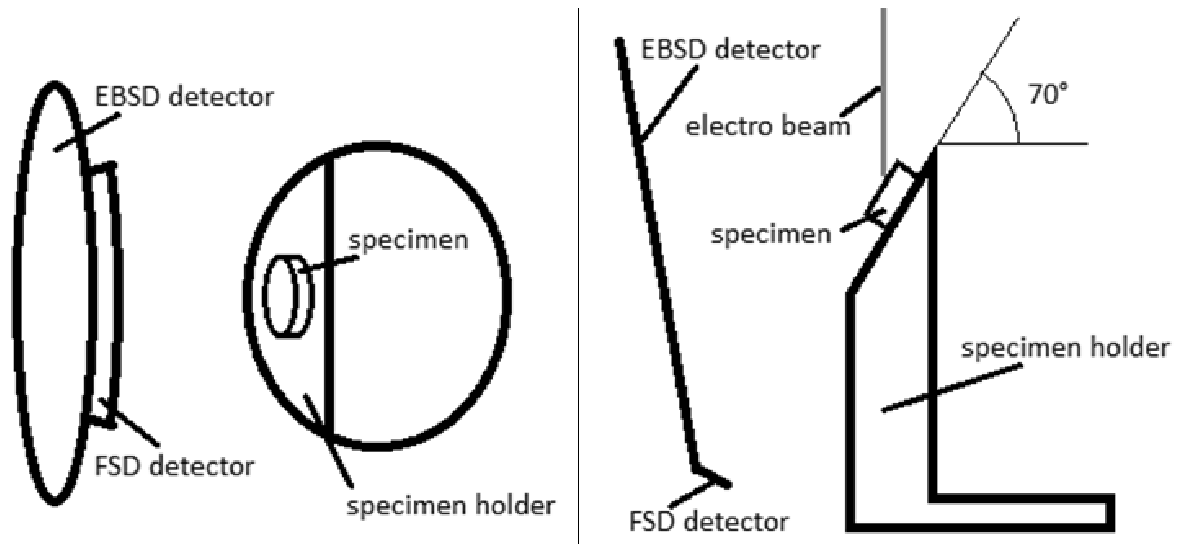

Figure 2-6: Schematic of the EBSD measurement assembly.

Compared to the standard SEM mode, the specimen is tilted by 70°. The distortions of the images caused in the respective direction during image recording are corrected by the software and the result should be a flat and undistorted OIM map. This is, of course, only the case if the rotation and the tilt angle are set correctly. A change of the tilt angle would stretch or compress the calculated height of the OIM image if the respective parameter in the software is not changed accordingly. If the rotation of the stage is not set correctly, the horizontal of the specimen surface is not parallel to the EBSD detector and the image becomes distorted angularly.

It was tested how sensitive the measurements are to errors in the tilt or the rotation angle.

Tilt

The relation between observed and calculated height is shown in equation (2-1).

$$\frac{h_0}{h_c} = \cos(70°) \qquad (2\text{-}1)$$

h_O... **observed height**

h_c... **calculated height**

Equation (2-2) shows the ratio between the actual height and the calculated height at a wrong tilt angle.

$$\frac{h_{70^\circ}}{h_x} = \frac{\cos(x)}{\cos(70^\circ)} \qquad (2\text{-}2)$$

h_{70°... **actual height**

h_x... **calculated height with a specimen tilt of x**

x... **actual tilt angle**

Even a small error of this angle greatly affects the calculated height as can be seen in Table 2-1.

Table 2-1: Relationship between tilt angle and calculated height of the OIM mapping.

tilt angle / °	ratio between calculated height and actual height / %
68°	0.91
69°	0.95
70°	1.00
71°	1.05
72°	1.11

Rotation

The calibration of the measurement system was tested using an etched silicon standard with a defined chessboard pattern (Figure 2-7).

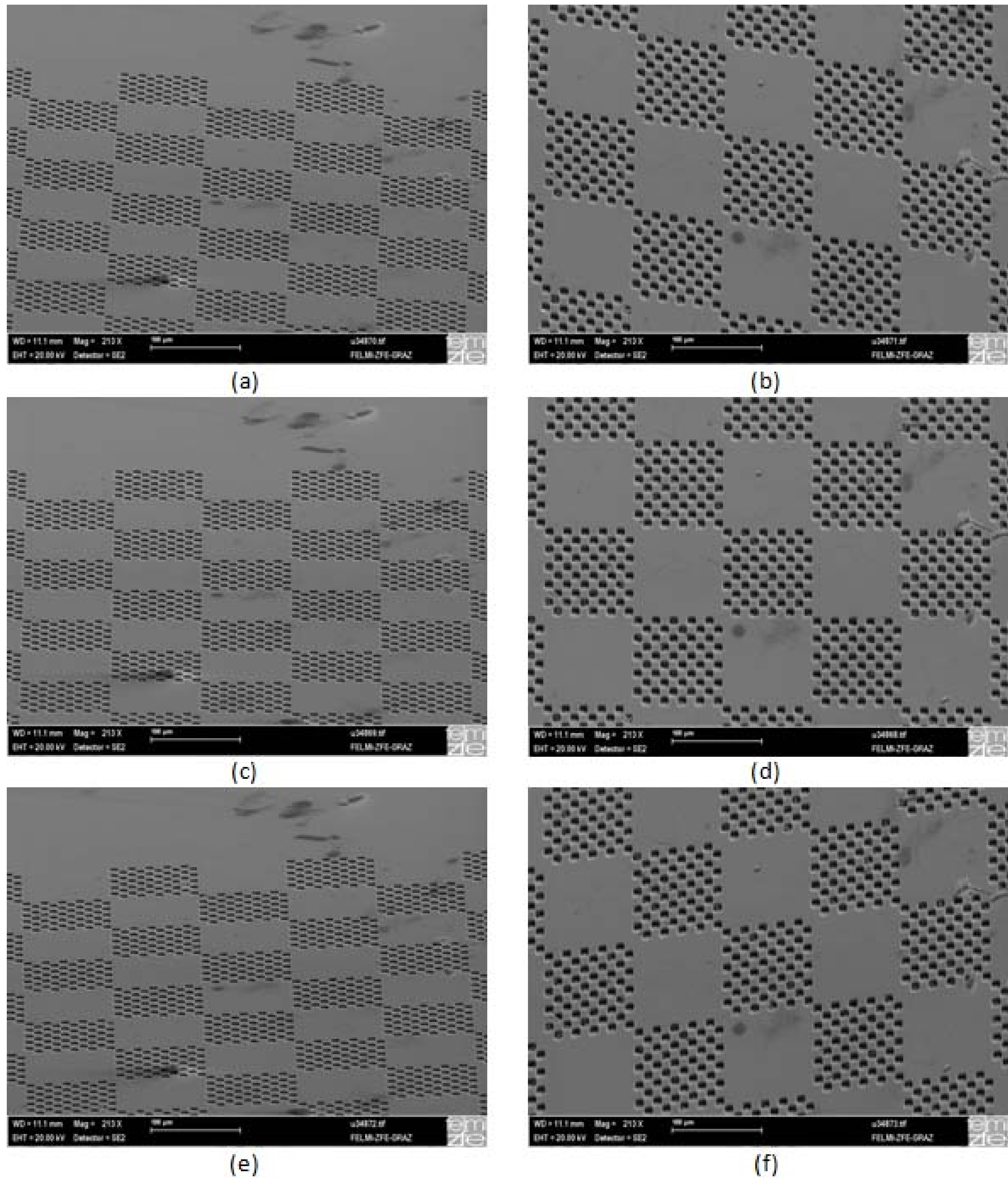

Figure 2-7: SEM images of the etched silicon standard: (a) rotation 14.0°, tilt 70°, (b) rotation 14.0°, tilt correction, (c) rotation 11.2°, tilt 70°, (d) rotation 11.2°, tilt correction, (e) rotation 8.4°, tilt 70° and (f) rotation 8.4°, tilt correction.

A stage rotation of 14° is obviously not ideal as the image shows strong angular distortion. Variation of the parameter showed an undistorted image at a rotation value of 11.2°. In addition an OIM mapping of the standard's surface was made (Figure 2-8).

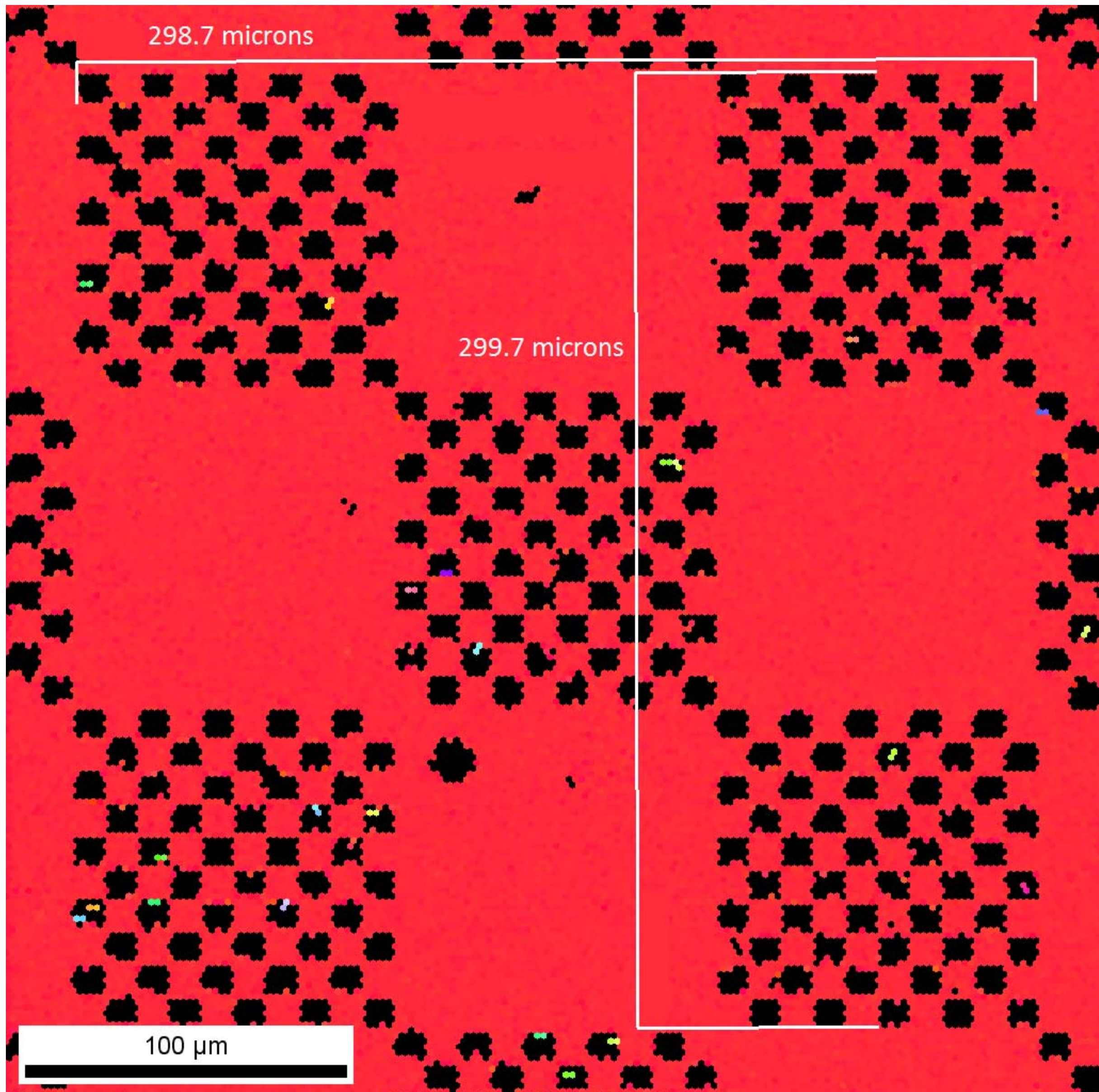

Figure 2-8: OIM map of the checked silicon standard; the large squares have a size of 100 µm x 100 µm.

The OIM map of the silicon standard shows no angular or linear distortion. Height and width were measured and their deviation from the nominal value of 300 µm is less than 0.5% which is within the range of the measurement error.

It is obvious that an error of the rotation angle would also affect the values of the measured orientations. To investigate this, the orientation of the silicon standard was measured for different rotation angles. The results are shown in Table 2-2.

Table 2-2: Change of measured orientation in dependence of the rotation angle of the sample.

rotation angle variation / °	change of the measured orientation / °
1.0	1.3
2.0	2.0
3.0	2.4

Orientation values were measured in the center of the viewed area. A calibration was performed after every change of the rotation angle. It seems that at least for small variations of the rotation angle the change of the measured orientation values equals the change of the rotation angle.

2.1.3 Memory effect

During an OIM mapping it was observed that the EBSD detector has a certain memory effect. It appears that all scanned pixels are shifted by one step. This also means that the last pixel of a row is moved to the first pixel of the following row. Additionally, the first few pixels of the mapping have the same orientation as the center point of the scan which is where the electron beam rests before the mapping.

The memory effect is clearly visible on the left side of an OIM mapping (e.g. Figure 2-9). One can see that the left and right borders of the picture fit together.

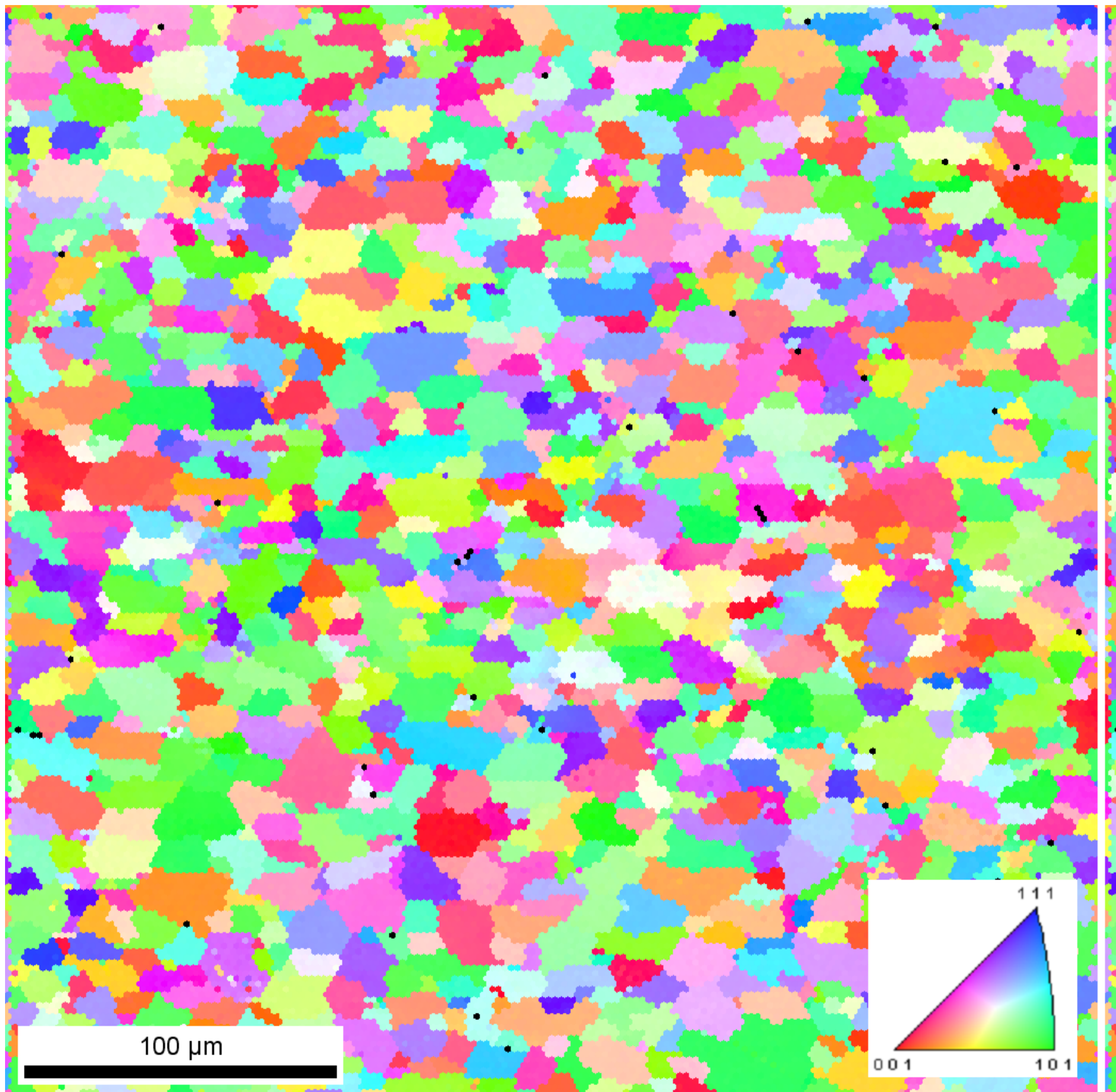

Figure 2-9: Memory effect in an inverse pole figure map of ferrite; on the right is a copy of the left border of the image; inset: color code for crystal orientations.

As the first column of the mapping usually does not fit together with the second column due to this memory effect, the software defines a grain boundary between them. As a consequence the edge grains on the left side of the mapping are not identified as such but as complete grains. This, of course, affects the result of the grain size analysis. This error can be avoided if the OIM map is cropped before a grain analysis is done. Table 2-3 shows the results of the grain analysis of the map of Figure 2-9.

Table 2-3: Memory effect and grain size analysis.

	number of grains	mean grain diameter / µm
scan with memory effect	1622	8.75
cropped scan	1560	8.77

The difference between the analyses is small in this case but it should not be ignored.

Further measurements showed that the memory effect disappears if the exposure time per pixel chosen for the recording of the OIM map is bigger than 0.08 seconds. Measuring with this setting would take nearly three times longer, as the standard value for the exposure time is 0.03 seconds.

2.1.4 Specimen surface preparation

For EBSD measurements a high surface quality is needed. To guarantee this, the samples are C-polished and Silica-polished.

C-polishing is performed by using the LaboPol-5 (Figure 2-10). The specimen is cleaned with distilled water and ethanol and placed in the sample holder of the polishing machine. The abrasive medium is diamond powder (DP-Spray P, 1/4 µm), which is sprayed on a polishing cloth.

The rotation speed is set to 400 rpm and the timer is set to 4 minutes. C-polishing is done under a steady flow of distilled water. After this step the specimen is placed in an ultrasonic bath for several minutes to remove remaining diamond particles from the surface. Then it is cleaned again.

Figure 2-10: The LaboPol5 grinding and polishing machine.

Silica-Polishing is done in two steps using the Minimet Polisher (Figure 2-11). For the first step a DP-NAP polishing cloth is used. The polishing is performed in a plastic bowl filled with OP-U suspension, which is a suspension of colloidal silica particles in 1,3-butandiol, water and sodium hydroxide [8]. It has additionally an etching effect which reduces stresses on the surface as induced by mechanical grinding and polishing. After 90 minutes the specimen is cleaned again.

Figure 2-11: The Minimet Polisher.

2.2 Serial sectioning for 3D measurements

2.2.1 Development of the method

Part of the experimental section of this master thesis is the development of a serial sectioning method used in combination with OIM mappings. It should be possible to map several surface areas of a specimen, remove a thin layer of the surface and map the same areas again. The procedure has to be repeated until a volume big enough to deliver the desired results has been processed. The layers removed from the specimen should have thicknesses smaller than the grain size of the recrystallized grains, thus smaller than 5 µm. The final result should give a 3D-representation of the interior structure of the respective material.

The method will be used to investigate the propagation of cracks and the progress of the recrystallization process (see 4.3).

The specimens used for the development of the serial sectioning method and the subsequent investigations were embedded pieces of a nickel based alloy (alloy 80A). The use of a focused ion beam (FIB) was not possible, because it does not enable the removal of such big volumes of material as was necessary in this investigation.

The sectioning consisted of several steps:

- Grinding,
- C-polishing,
- Silica-polishing and height measurement of the removed layer using Vickers indentations.

For the grinding SiC grinding paper was used. The embedded specimen was cleaned with distilled water and ethanol and then placed in the sample holder of a LaboPol-5 grinding and polishing machine. The rotation speed was set to 250 rpm. The grinding happened under a steady flow of regular water. After the grinding the specimen was cleaned again.

C-polishing and Silica polishing was performed as described in 2.1.4.

For measuring the thickness of the removed layer the heights of Vickers indentations in the material were determined before and after polishing using a light microscope (Figure 2-12). A similar method was used by Sharma et al. [9].

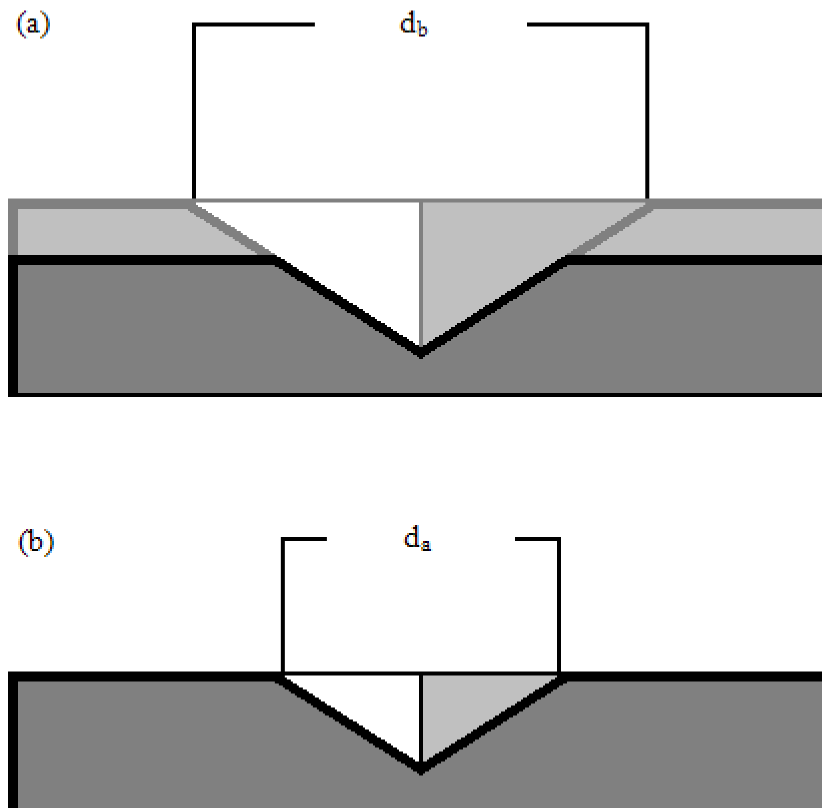

Figure 2-12: Schematic diagram of the determination of the thickness of the removed layer by Vickers indentation measurements: (a) Vickers indentation with diagonal d_b before polishing; (b) Vickers indentation with diagonal d_a after polishing.

The Vickers indentations were made by using a EMCO-TEST M4C 025 G3M (Figure 2-13).

Figure 2-13: EMCO-TEST M4C 025 G3M.

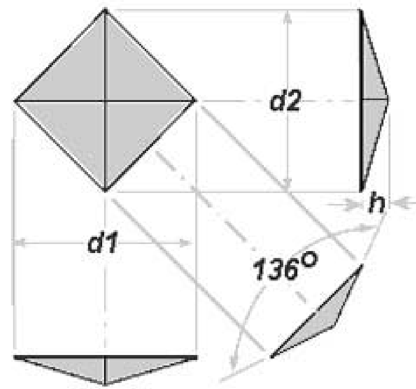

Figure 2-14: Geometry of a Vickers indentation.

Both diagonals were measured. Looking at the geometry of the Vickers pyramid (Figure 2-14), the depth of the indentation can be calculated using the following equation:

$$h = \frac{d_1 + d_2}{2} \cdot \frac{\tan(22°)}{\sqrt{8}} \qquad (2\text{-}3)$$

d_1, d_2... **diagonals of the Vickers indentation**

h... **depth of the Vickers indentation**

The thickness of the removed layer is the difference in the depth of the indentation before and after sectioning:

$$a = h_1 - h_2 \qquad (2\text{-}4)$$

h_1... **depth of the Vickers indentation before sectioning**

h_2... **depth of the Vickers indentation after sectioning**

a... **thickness of the abraded layer**

2.2.2 Testing the method

To test the method and also to investigate the rate of material removal by the different preparation steps, several measurements were done in two series. For the first series (Table 2-4) five Vickers indentations were made on the specimen surface as marked in Figure 2-15. For the second series (Table 2-5) four Vickers indentations were made as shown in Figure 2-16.

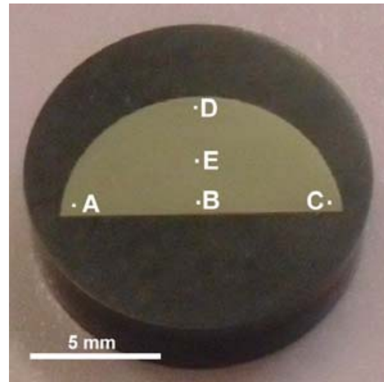

Figure 2-15: Test specimen with the first series of Vickers indentations.

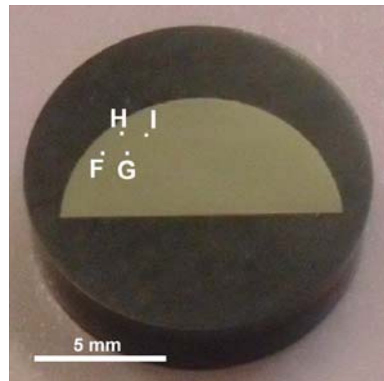

Figure 2-16 : Test specimen with the second series of Vickers indentations.

Table 2-4: Abrasion values for different preparation steps, series 1.

preparation type	preparation time / min	abrasion A / µm	abrasion B / µm	abrasion C / µm	abrasion D / µm	abrasion E / µm
C-polishing	4	0.2	0.4	0.3	-0.2	0.4
grinding P4000	4	6.1	7.4	5.3	5.7	4.3
C-polishing	4	-0.5	-0.5	0.1	0.3	0.8
grinding P4000	2	2.3	2.1	1.2	1.0	0.3
grinding P4000	2	1.5	1.9	0.9	0.8	0.8
grinding P4000	2	2.0	2.0	1.5	1.2	0.6
grinding P4000	4	2.7	2.3	1.6	1.5	1.0
grinding P2500	2	>30.0	>30.0	>30.0	>30.0	>30.0

Table 2-5: Abrasion values for different preparation steps, series 2.

preparation type	preparation time / min	abrasion F / µm	abrasion G / µm	abrasion H / µm	abrasion I / µm
grinding P4000	16	9.8	11.5	7.3	7.4
grinding P4000	4	1.1	1.4	1.3	1.2
C-polishing Si-polishing	4 30	-0.2	-0.1	-0.2	0.0
grinding P4000	20	5.7	6.2	5.8	6.1
C-polishing Si-polishing	4 30	1.8	1.6	1.3	1.3
grinding P4000	20	5.4	5.4	5.8	5.7
C-polishing	4	0.4	0.3	0.3	0.3
Si-polishing	30	0.4	0.6	0.3	0.3
grinding P4000	12	2.8	2.7	3.5	3.6
grinding P4000	8	1.6	1.1	2.4	2.0
C-polishing	4	0.3	0.5	0.3	0.2
Si-polishing	30	1.2	1.1	0.6	0.7
grinding P4000	4	0.8	0.9	0.8	0.8
C-polishing	4	0.1	0.3	0.3	0.0
Si-polishing	30	0.5	0.5	0.3	0.5
grinding P4000	4	0.7	0.5	0.8	0.7
C-polishing	4	0.1	0.2	0.1	0.2
Si-polishing	30	0.3	0.3	0.2	0.2

The measurements showed several aspects that had to be considered for the experiment:

- Only the finest grinding paper available in the laboratory (P4000) was useable for this method. Using a P2500 grinding paper would grind down the specimen too fast.
- The abrasions varied at different measurement points. Measurement points near the edge of the specimen tended to have higher abrasions.
- The abrasion values for equally performed preparations fluctuated beyond the measurement error.
- The abrasive effects of C-polishing and Silica-polishing are small and not constant.

It was clear now that some non controllable parameters affected the results of the sectioning steps. Repeated height measurement during sectioning should still allow a controllable sectioning process.

2.2.3 Accuracy

Before calculating the error of the height measurement, the measurement error of the light microscope and its software had to be determined first. Features of different lengths in two standards were measured as shown in Figure 2-17 and Figure 2-18. The measurement error never exceeded 0.9 µm.

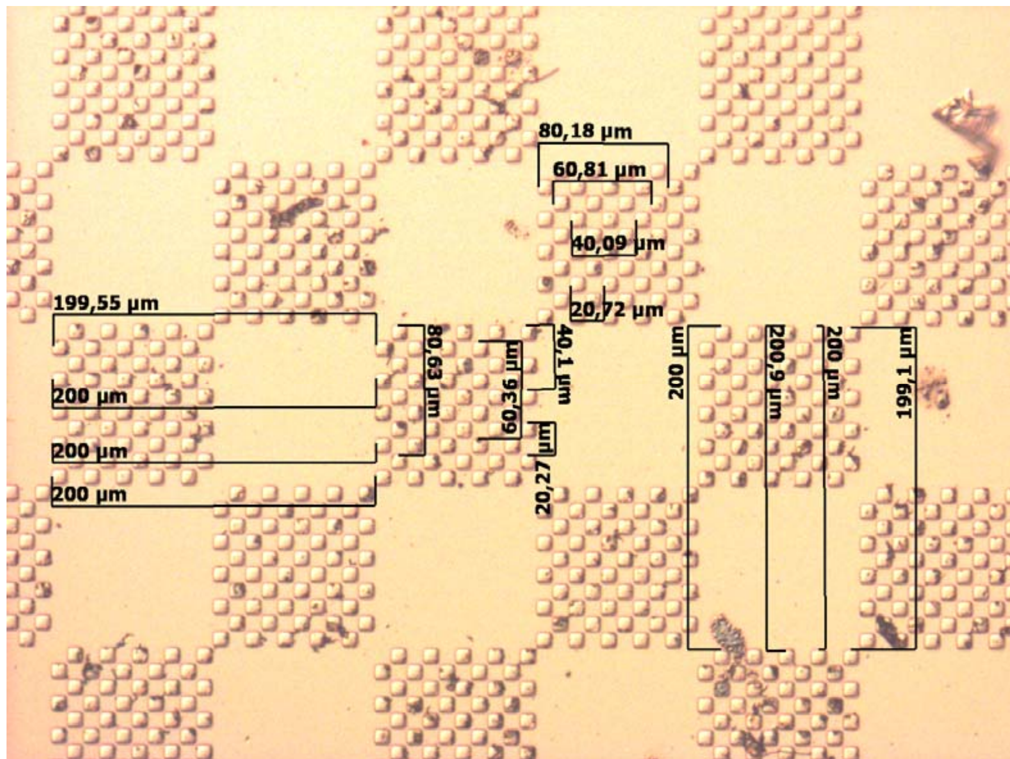

Figure 2-17: Etched Si-standard.

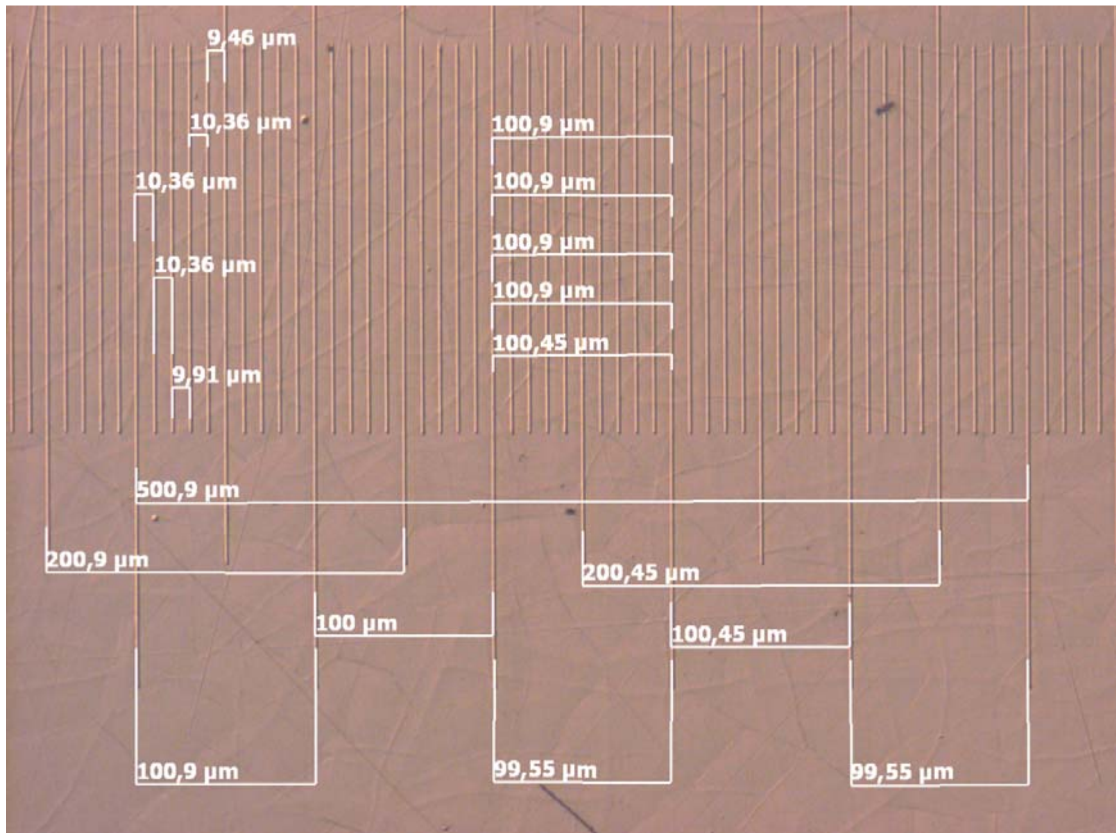

Figure 2-18: Ruler standard.

As the sharpness of the edges of the Vickers indentations varied, a certain reading error had to be assumed. It was estimated to have a maximum value of 1.0 µm. Adding measurement error and reading error, the maximum error for the diagonals of the Vickers indentations is

$$\Delta d = 1.9\ \mu m.$$

In the following calculations the Gauss' method for the error propagation (equation (2-5)) is used.

$$\Delta y = \sqrt{\left(\frac{\partial y}{\partial x_1} \cdot \partial x_1\right)^2 + \left(\frac{\partial y}{\partial x_2} \cdot \Delta x_2\right)^2 + \cdots} \qquad (2\text{-}5)$$

The error for the height measurement given by equation (2-3) is shown in equation (2-6).

$$\Delta h = \frac{\sqrt{\Delta d_1 + \Delta d_2}}{2} \cdot \frac{\tan(22°)}{\sqrt{8}} \qquad (2\text{-}6)$$

Δd_1, Δd_2... measurement error for the diagonals of the Vickers indentation

Δh... measurement error for the depth of the Vickers indentation

The errors for the diagonals of the Vickers indentations are $\Delta d_1 = \Delta d_2 = 1.9$ µm and therefore the error for the height is

$$\Delta h = 0.4\ \mu m.$$

The error for the thickness of the abraded layer (equation (2-4)) is calculated.

$$\Delta a = \sqrt{\Delta h_1^2 + \Delta h_1^2} \tag{2-7}$$

Δh_1... **error for the depth measurement of the Vickers indentation before sectioning**

Δh_2... **error for the depth measurement of the Vickers indentation after sectioning**

Δa... **error for the thickness measurement of the abraded layer**

Using Δh from above, the measurement error for the abrasion is:

$$\Delta a = 0.6\ \mu m.$$

3 Grain size measurements: variation of step size, minimum misorientation angle and minimum number of points per grain

3.1 Grain boundaries

3.1.1 Fundamentals

Grain boundaries are interfaces between the grains of a polycrystalline material. With orientation imaging microscopy (OIM) grain boundaries can be detected by comparing the orientations of neighboring measurement points. If the misorientation between two measurement points exceeds a certain preset angle, the minimum grain boundary misorientation, a grain boundary is defined between these points. Low angle grain boundaries (LAGB) and high angle grain boundaries (HAGB) are distinguished. In theory, LAGBs are made up completely of dislocations whereas HAGBs tend to have a more irregular structure. Up to a relative misorientation angle of 15° the type made up of dislocations is energetically stable, above it is not. Therefore LAGBs and HAGBs are typically distinguished at 15°. [10]

There is no real convention how the minimum grain boundary misorientation angle should be chosen and if LAGBs should be included or not. But the choice of this angle influences, of course, the grain size measurements: The smaller the minimum misorientation angle is, the smaller is in general the average grain diameter. As grain size distributions that on the one hand were measured by OIM and on the other hand gained from etched specimens should match, such a comparison could be a means for the "correct" choice of the minimum misorientation angle.

With TSL OIM Analysis 5 software it is possible to choose the grain boundary misorientation limits for HAGBs and LAGBs. It was examined how a variation of these parameters would affect the results of the analysis (total grain boundary length, average grain diameter).

3.1.2 Measurements

The two specimens used for the investigation were made of steel and ferrite. Three scans were recorded from the steel and one from the ferrite. The measurement parameters for the scans are listed in Table 3-1. The minimum misorientation angle was changed between 5° and 25° in steps of 5°. For all analyses a cleanup was performed using the respective minimum misorientation angles (5° - 25°) and a minimum grain size of 2 pixels.

Table 3-1: Parameters for grain boundary measurements.

specimen	scan area / μm^2	step size / µm
Steel A	400x400	0.7
Steel B	400x400	0.7
Steel C	400x400	0.7
Ferrite	350x350	1.0

3.1.3 Results and discussion

Figure 3-1 shows the distribution of the misorientation angles for ferrite and steel. Steel has a remarkable peak at 60° which is due to twin grain boundaries. Apart from that, the distributions are similar.

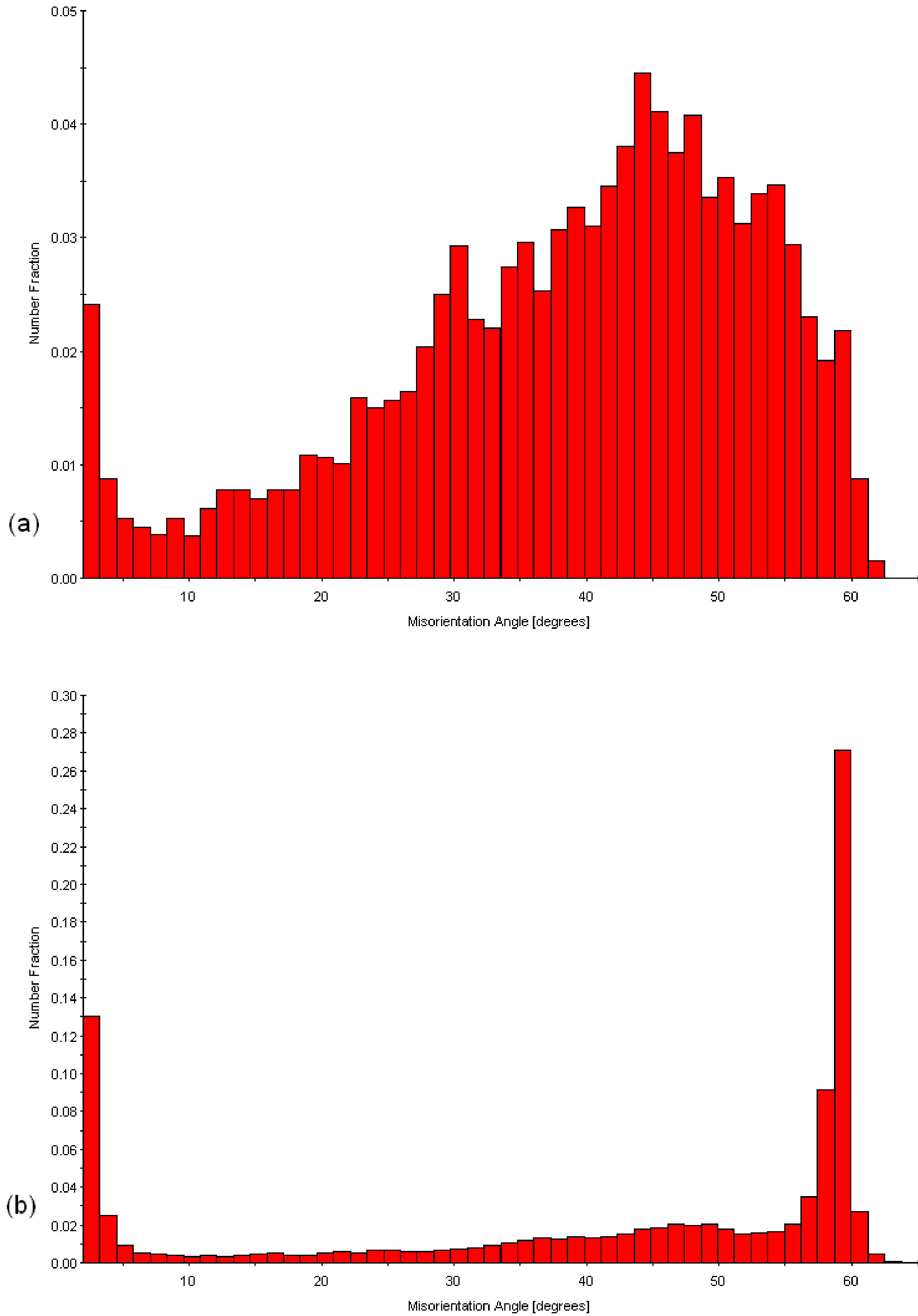

Figure 3-1: The distribution of the misorientation angles for (a) ferrite and (b) steel A.

The changes in the number of grains, the average grain diameter and the total grain boundary length in dependence on the minimum misorientation angle are shown in Table 3-2 and Figure 3-2. Twin grain boundaries were included in the analysis.

Table 3-2: Results for grain boundary measurements.

Steel A			
minimum misorientation angle / °	number of grains	average grain diameter / µm	total grain boundary length / cm
5°	971	10.38	3.17
10°	917	10.69	3.10
15°	850	10.95	3.04
20°	775	10.90	2.97
25°	683	11.04	2.89
Steel B			
minimum misorientation angle / °	number of grains	average grain diameter / µm	total grain boundary length / cm
5°	1117	9.85	3.54
10°	1055	10.12	3.44
15°	994	10.25	3.38
20°	917	10.34	3.31
25°	802	10.33	3.21
Steel C			
minimum misorientation angle / °	number of grains	average grain diameter / µm	total grain boundary length / cm
5°	1017	9.94	3.09
10°	961	10.18	3.04
15°	896	10.36	2.99
20°	817	10.48	2.93
25°	713	10.51	2.85
Ferrite			
minimum misorientation angle / °	number of grains	average grain diameter / µm	total grain boundary length / cm
5°	1450	8.77	3.36
10°	1394	8.91	3.29
15°	1269	9.22	3.20
20°	1113	9.66	3.08
25°	868	10.37	2.90

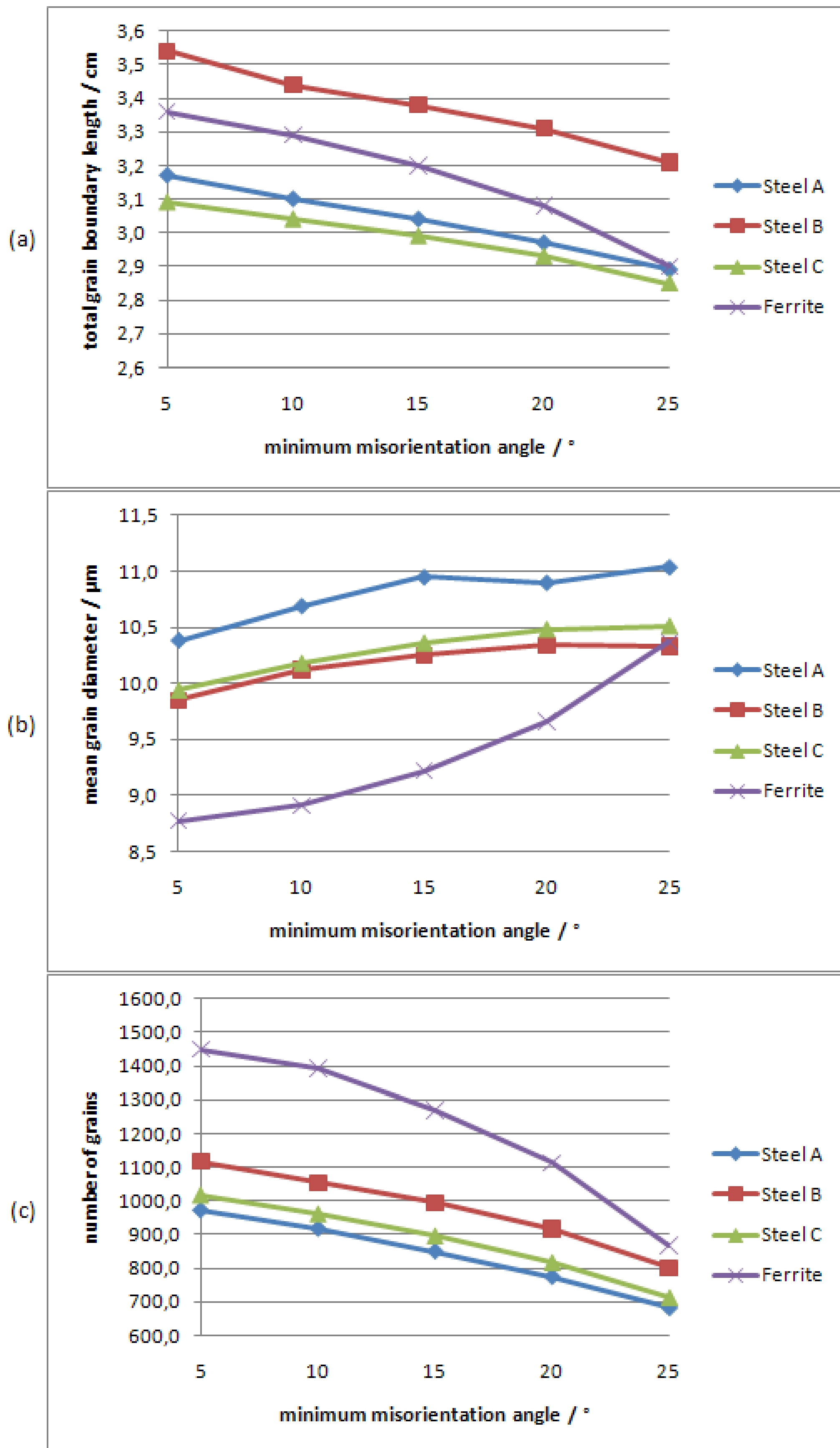

Figure 3-2: Results for grain boundary measurements: Dependency of the minimum misorientation angle on (a) total grain boundary length, (b) mean grain diameter, (c) number of grains.

The higher the minimum misorientation angle is chosen, the fewer grain boundaries will appear. The total grain boundary length and the number of grains decrease whereas the mean grain diameter increases. Contrary to this, there is a small decrease of the mean grain diameter for steel B (Figure 3-2-(b)). The reason for this effect could be that some large grains grow together with edge grains, which are excluded from the analysis.

Apart from that, the three measurements for steel show the same behavior. Ferrite shows a faster decrease in the total grain boundary length and the number of grains and a stronger increase for the mean grain diameter. This means that ferrite has a larger amount of grain boundaries with misorientation angles between 5° and 25° than steel. The probable reason is twin grain boundaries with a misorientation angle of 60° which appear in steel but not in ferrite (Figure 3-3).

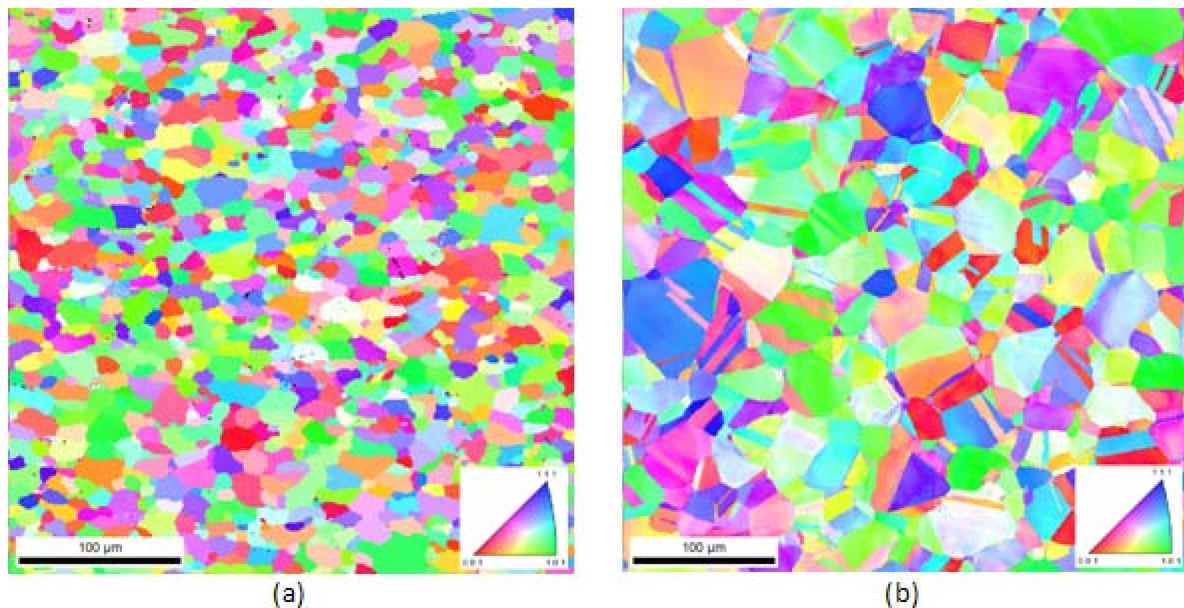

Figure 3-3: Inverse pole figure maps of (a) ferrite and (b) steel A; inset: color code for crystal orientations.

For the steels A, B and C the behavior of the three measured quantities is almost linear between 5° and 15°. For misorientation angles between 15° and 25° the gradient increases slowly.

Conclusively the choice of the misorientation angle of course affects the results of the analysis, with the maximum deviations depending on the material. The maximum variation of the measured mean grain diameter within the range of 5° to 25° was 18% for the ferrite specimen. This variation cannot be neglected and it seems obvious that a standard procedure for the choice of the minimum misorientation angle should be defined in order to increase the comparability of measurements from different sources.

3.2 Step size

3.2.1 Fundamentals

The step size is the distance between neighboring measurement points in an OIM scan. The data collection software (TSL OIM Data Collection) allows to choose between two kinds of measurement grids – hexagonal or square.

It is obvious that the choice of the step size can greatly affect the measurement results such as the mean grain diameter or the number of grains. If the step size is chosen too large, small grains could be missed. If it is chosen very small, no grains should be missed but the measurement time would be very long. There could be an ideal step size where no grains would be missed and where the measurement time would be as short as possible. In theory a scan with an even shorter step size should produce the same results.

3.2.2 Measurements

The specimen used for the OIM scans was ferrite. Table 3-3 shows the measurement parameters for all scans.

Table 3-3: Parameters for step size measurements.

scan	scan area / µm²	step size / µm	grid
1	100x100	4.0	hexagonal
2	100x100	4.0	square
3	100x100	3.5	hexagonal
4	100x100	3.5	square
5	100x100	3.0	hexagonal
6	100x100	3.0	square
7	100x100	2.5	hexagonal
8	100x100	2.5	square
9	100x100	2.0	hexagonal
10	100x100	2.0	square
11	100x100	1.5	hexagonal
12	100x100	1.5	square
13	100x100	1.0	hexagonal
14	100x100	1.0	square
15	100x100	0.5	hexagonal
16	100x100	0.5	square
17	100x100	0.25	hexagonal
18	100x100	0.25	square
19	100x100	0.10	hexagonal
20	100x100	0.10	square
21	100x100	0.05	hexagonal

3.2.3 Results and discussion

As parameters for the first analyses a minimum of two pixels per grain and a minimum misorientation angle of 5° were chosen. A cleanup of the OIM scans was carried out using the same parameters but it had only a small effect. Figure 3-4 shows the relation between the chosen step size and the measured mean grain diameter for both types of measurement grids.

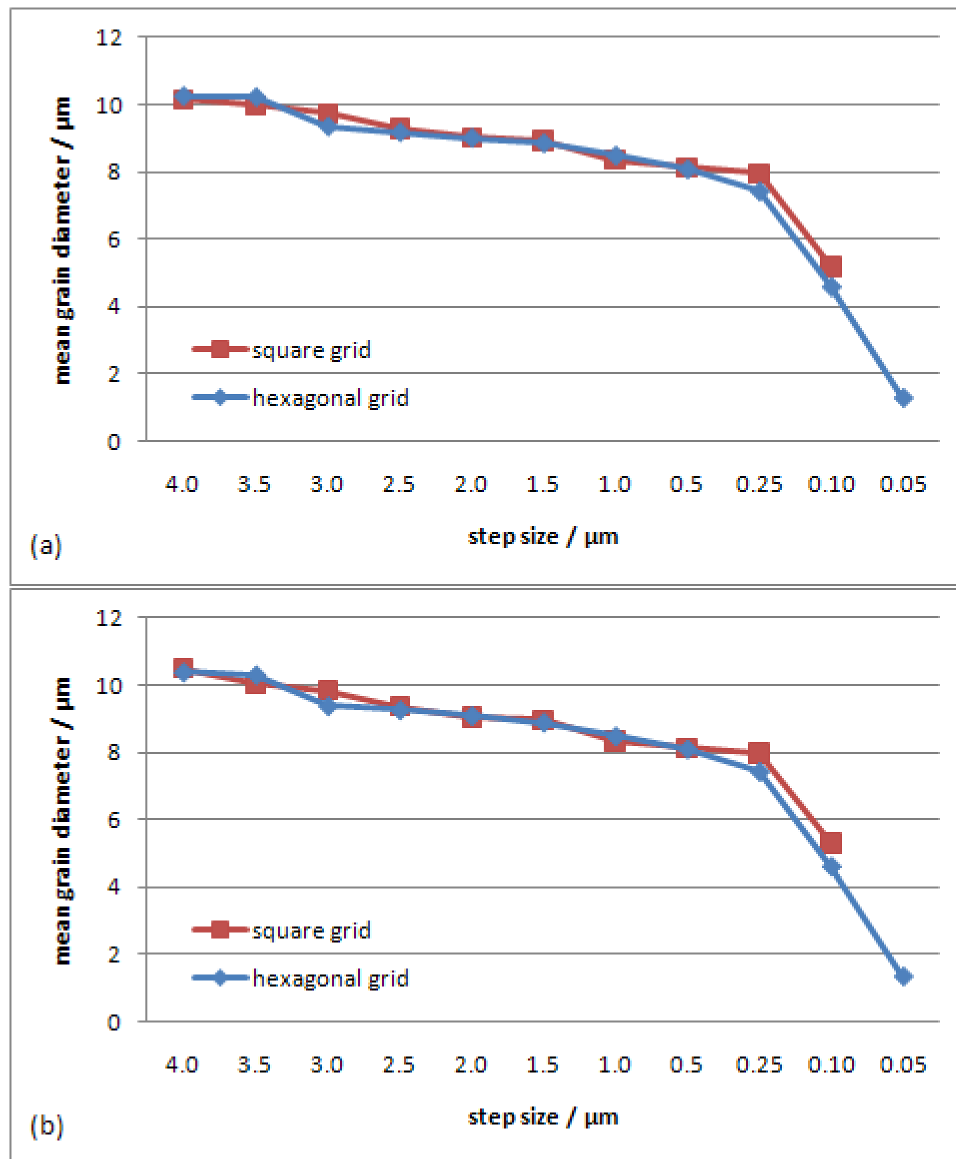

Figure 3-4: Measured mean grain diameter for hexagonal and square grids in dependence on the step size; (a) no cleanup, (b) cleanup with minimum 2 pixels per grain and 5° minimum misorientation angle; the scaling for the step size is irregular.

The results of the analysis were unexpected. With a reduction of the step size a decrease of the mean grain diameter was expected, but below a certain value of the step size it should stay at a constant value. Contrary to this, the measured mean grain diameter decreases strongly for step sizes smaller than 0.25 µm. The reasons for this behavior are measurement inaccuracies close to the grain boundaries and the minimum numbers of pixels with the same orientation chosen for the formation of a grain. Near grain boundaries the EBSD diffraction patterns from the adjacent grains can superpose, resulting in an incorrect calculation of the orientation at the respective pixel. For small step sizes this can affect a region of a few measurement points surrounding the grain boundaries as can be seen in Figure 3-5-(a). As the calculated orientations at the pixels

within this region are random, there can be neighboring measurement points with similar albeit incorrect orientations.

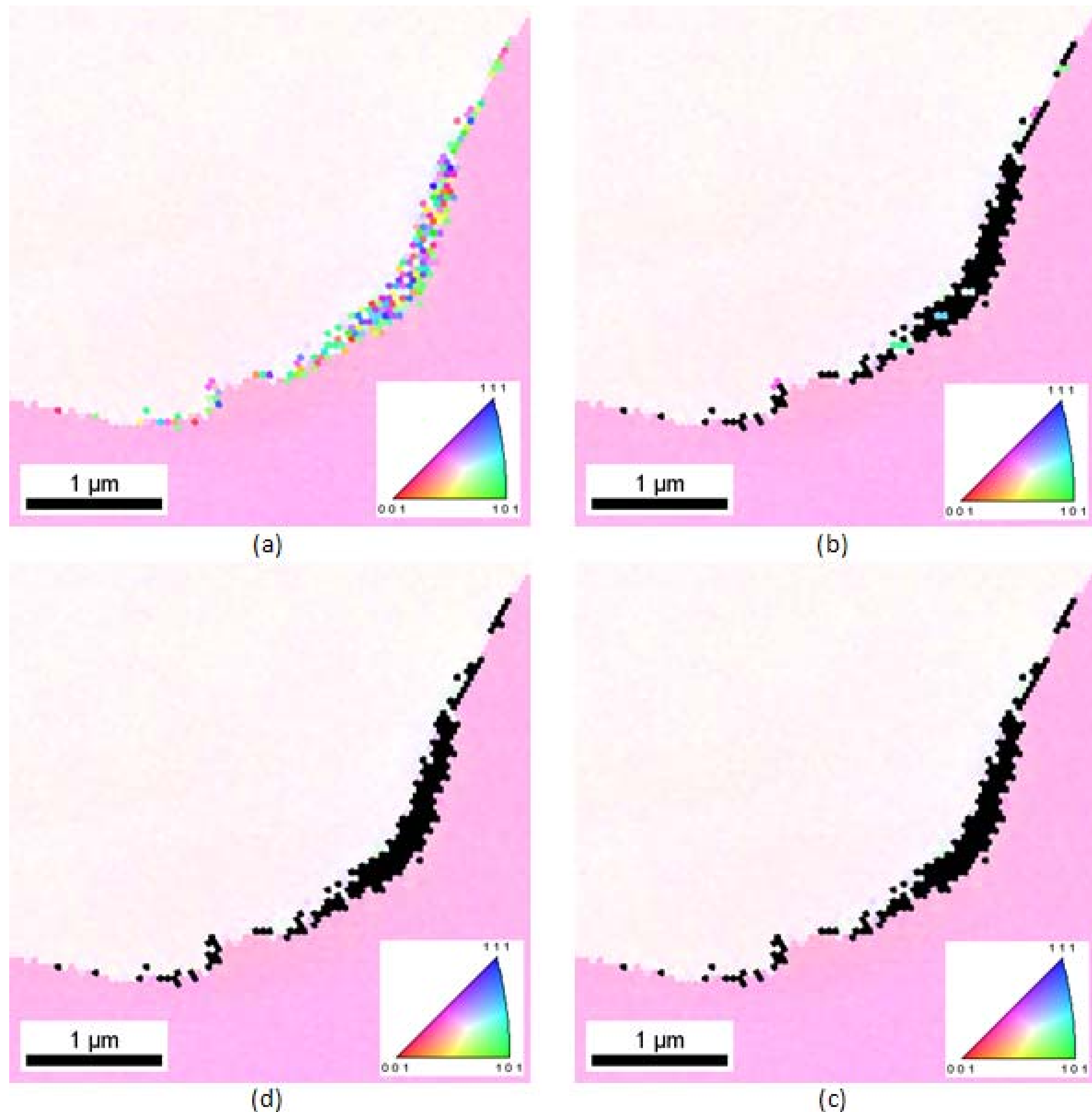

Figure 3-5: Inverse pole figure maps of the area surrounding a grain boundary; (a) all measured orientations, (b) orientations of grains with a minimum of two pixels per grain, (c) orientations of grains with a minimum of four pixels per grain and (d) orientations of grains with a minimum of six pixels per grain; inset: color code for crystal orientations; the black points are not assigned to a grain.

Figure 3-5 shows the area surrounding a grain boundary with different values for the minimum number of pixels per grain. In (b) there are several small grains visible at the grain boundary. They disappear in (c) and (d) where for the recognition of a grain a higher number of pixels is necessary. If the minimum number of pixels per grain is chosen high enough, the probability of finding sufficient neighboring pixels with a similar orientation to form a grain becomes very small. Keeping this in mind, another analysis was performed. All scans were evaluated with a minimum number of 4 and 6

pixels per grain and compared to the earlier results with a minimum number of 2 pixels per grain. The new results are shown in Figure 3-6.

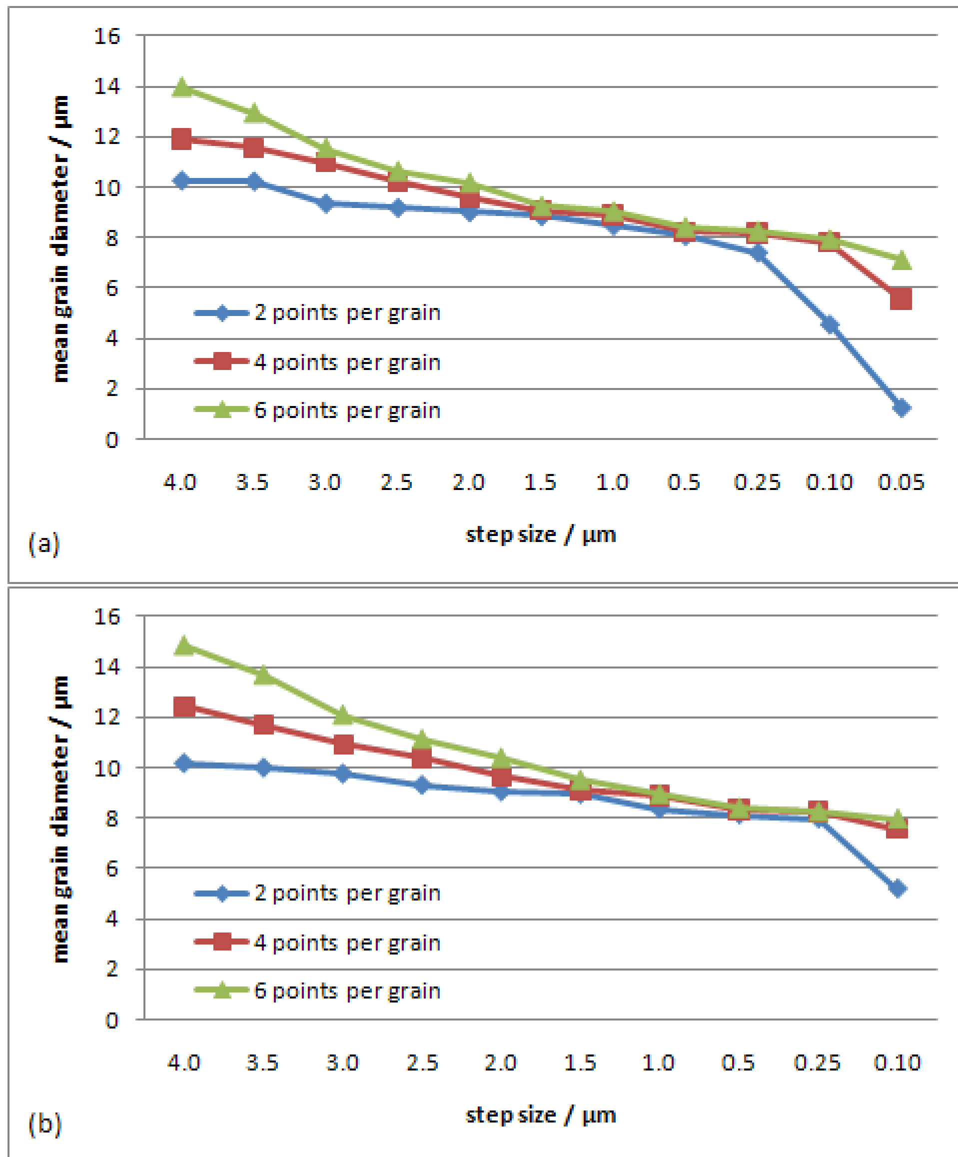

Figure 3-6: Measured mean grain diameter for a minimum number of 2, 4 and 6 pixels per grain in dependence on the step size; (a) hexagonal grid, (b) square grid; the scaling for the step size is irregular.

One can see that the 3 graphs drift apart at very big and very small step sizes. For big step sizes it is more likely to miss smaller grains if the minimum number of pixels per grain is too high. In this case the measured mean grain diameter tends to be higher. For small step sizes wrong orientation measurements are not likely to be interpreted as small grains if the minimum number of pixels per grain is chosen high enough. The mean grain diameter should be more accurate in this case. Nearly no dependence of the results on the minimum number of pixels can be observed for step sizes between 0.5 µm and 1.5 µm. But this would, of course, not be true in cases where the average diameter of the

grains is much smaller than in the present case. A step size chosen within this range should give good results for comparable grain structures. A look at the measurement times shows, that it took 9 times as long to scan a specified area with a step size of 0.5 µm than with a step size of 1.5 µm.

If the range of this ideal step size is compared to the mean grain diameter of ~9 µm, one can calculate the optimal ratio between the mean grain diameter and the step size:

$$\frac{d}{S_{opt}} \approx 6\ to\ 18 \qquad (3\text{-}1)$$

S_{opt} **optimal step size**

d **mean grain diameter**

Of course this empiric rule can only be used for materials with a grain size distribution similar to the analyzed sample (Figure 3-7).

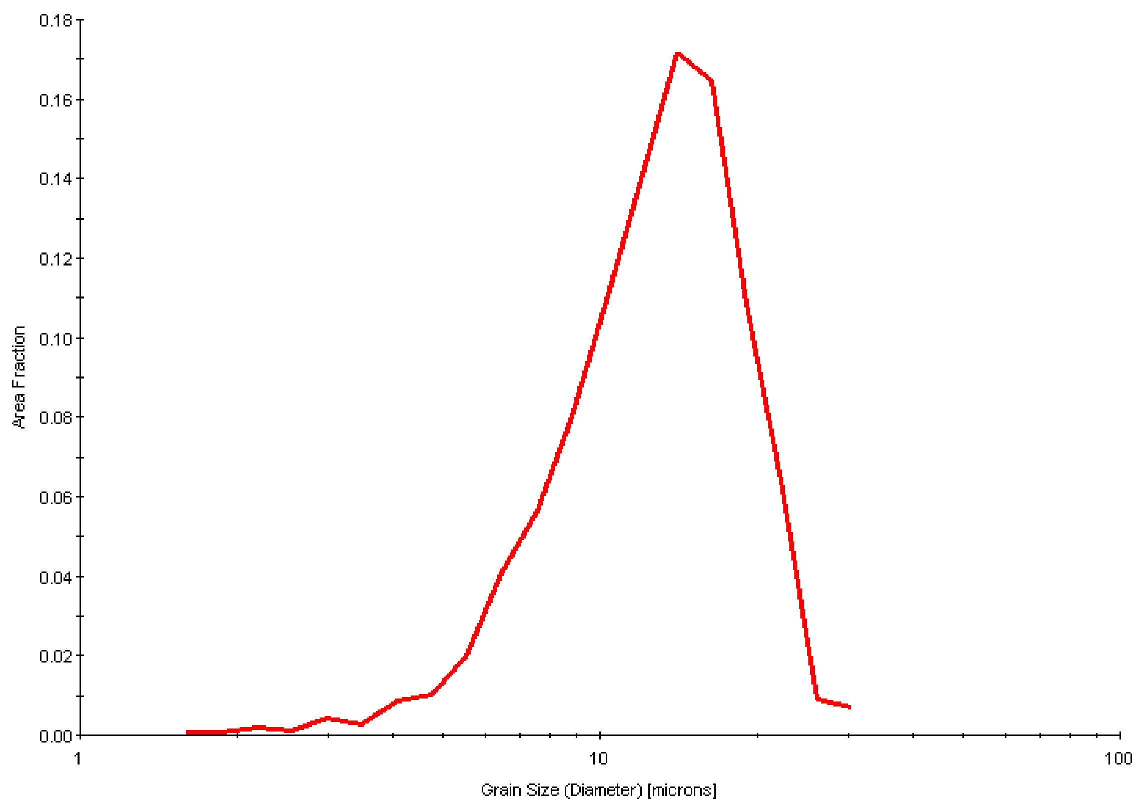

Figure 3-7: The distribution of the grain diameters for the ferrite sample.

If the distribution of the grain sizes is substantially broader, the step size should be chosen smaller to prevent missing small grains.

4 Investigations of particles and bulk specimens

4.1 EBSD measurements at small particles

In this part of the experimental section the influences of both the size and the preparation of the particles on the quality of the EBSD patterns were investigated. Different materials on varying substrates were chosen in order to gain experience in the analysis of small particles. After some basic measurements nickel nanowires in a porous silicon matrix (specimen by courtesy of P. Granitzer) were analyzed.

4.1.1 Mineral particles

Specimen

For the quality of the EBSD patterns the average atomic number of the sample is very important, because the backscattering coefficient increases with an increase of this number. The average atomic number can be calculated using equation (4-1).

$$Z = \sum_i c_i \cdot Z_i \quad (4\text{-}1)$$

Z.... **average atomic number of a mineral**

c_i... **elements' mass fractions for the mineral**

Z_i... **elements' atomic numbers**

The higher the mean atomic number is, the better in general the quality of the diffraction patterns will be. The following minerals were chosen for the investigations: $CuSO_4$, K_2SO_4, $CaCO_3$, $CaCl_2$ and $CaCl_2*2H_2O$. They have different average atomic numbers which are listed in Table 4-1. $CaCl_2$ was chosen because it was available with and without crystallization water. The intention was also to find the smallest particle size for which EBSD measurements are possible.

Table 4-1: Mineral samples and their average atomic numbers.

mineral	average atomic number
$CaCO_3$	12.6
K_2SO_4	14.4
$CuSO_4$	18.0
$CaCl_2$	18.1
$CaCl_2*2H_2O$	15.4

All these chemicals are neither toxic nor difficult to handle which was also a reason for their choice. They were then milled in a “Fritsch Pulverisette” ball mill for 15 minutes (see Figure 4-1). The original mineral particles as well as the milled ones were fixed on sample holders using conductive carbon tape.

Figure 4-1: Fritsch Pulverisette ball mill.

Measurement and results

First the untreated $CaCO_3$, $CuSO_4$ and K_2SO_4 particles were investigated. These particles had diameters greater than 1 µm. Figure 4-2 shows the diffraction patterns for the three samples.

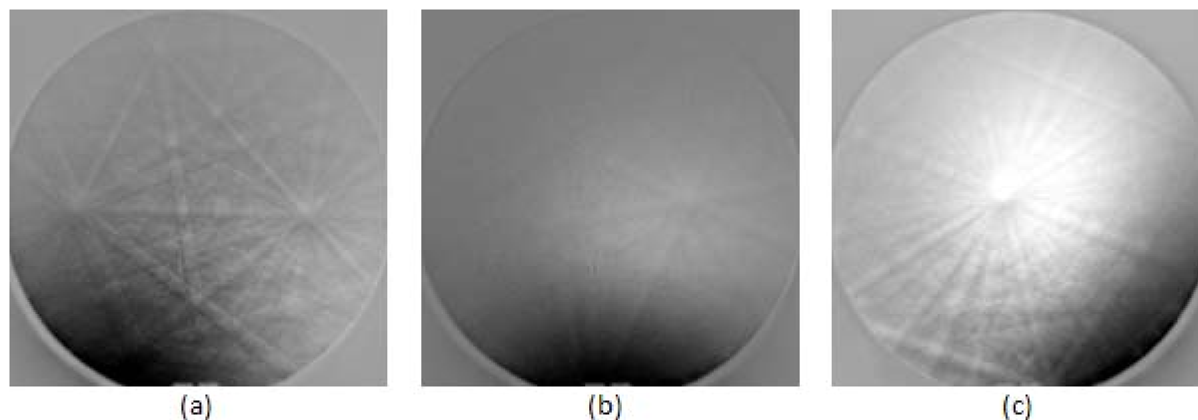

Figure 4-2: Diffraction patterns of (a) $CaCO_3$, (b) $CuSO_4$ and (c) K_2SO_4.

The diffraction patterns of K_2SO_4 and $CaCO_3$ have a good quality. Surprisingly the pattern quality for $CuSO_4$, which has the highest average atomic number of the three samples, is inferior to the others. This could be due to irradiation damage caused by the electron beam. All measurements were performed by spot analysis using the same measurement parameters (electron energy: 20keV, exposure time: 0.08s). It was also suspected that $CuSO_4$ contained crystallization water which would reduce the average atomic number and therefore the backscattering coefficient.

The measurements for the milled particles were unsuccessful. For $CuSO_4$ and K_2SO_4 no patterns could be produced. For $CaCO_3$ a pattern with about the same quality as in Figure 4-2 was measured. Again the measured particle diameters were greater than 1 µm because the particles were not filtered and the smaller particles formed agglomerates.

The most probable reason why no useful patterns could be recorded after milling is the presence of strains in the surface of the particles caused by the milling. The milling process is comparable to mechanical polishing.

To investigate the presence of crystallization water, $CuSO_4$ was analyzed using the EDXS system of a Quanta 200 SEM. Table 4-2 shows the results of the analysis.

Table 4-2: Results of the EDXS analysis of milled $CuSO_4$ particles.

element	calculated rate / at.%	measured rate / at.%
Cu	16.7	16.1
S	16.7	13.2
O	66.6	70.7

There is no indication of crystallization water. It was speculated that the electron irradiation might be the cause for the loss of the crystallization water. To investigate this further, $CaCl_2*2H_2O$ was analyzed via EDXS. The results are visible in Table 4-3.

Table 4-3: Results of the EDXS analysis of $CaCl_2$ particles.

element	calculated rate / at.%	measured rate / at.%
Ca	20.0	19.0
Cl	40.0	38.3
O	40.0	42.7

It seems that the crystallization water is still present in the mineral. Moreover it has to be noted that $CaCl_2$ is extremely hygroscopic and during the time it took to mount the particles on a sample holder, they absorbed so much humidity that water droplets became visible. For this reason no EBSD measurements were done with $CaCl_2$.

At this point it became obvious that some minerals were unsuitable for EBSD measurements, especially after milling, which was performed in order to create sub-µm particles. It was decided to cancel further measurements using filtered mineral particles. The investigations were continued using metal particles as described in the following section. Still the results are an indication that difficulties might rather often arise if EBSD is performed on environmental particles. Because of friction of particles to one another or rapid cooling down (e.g. volcanic particles) stresses in the surface of the particles might develop, similar to grinding. As the information depth of EBSD is lower than 100 nm, also contamination layers on environmental particles can prevent a successful EBSD analysis.

4.1.2 Nickel particles formed during wire explosions at different substrates

Specimen

Nickel particles produced in two wire explosion experiments (specimens by courtesy of G. Pottlacher, Institut für Experimentalphysik, TU Graz) and collected on different substrates were investigated. As substrates both amorphous and crystalline materials were chosen: Nucleopore filters (pore diameter 0.05 µm), a polished ferrite plate and silicon wafers. The Nucleopore filter was chosen because it is amorphous and therefore does not produce a diffraction pattern that could superpose with the diffraction patterns

of the small particles. On the other hand, ferrite and silicon were chosen because their diffraction patterns might superpose with those of the particles and because these systems were similar to specimens that should be investigated within the framework of research projects.

At all substrates two kinds of particles could be found: big spherical particles with diameters in the micrometre range (see Figure 4-3) and agglomerates of spherical particles with diameters smaller than 100 nm (see Figure 4-4). The latter were the more interesting ones for the measurements.

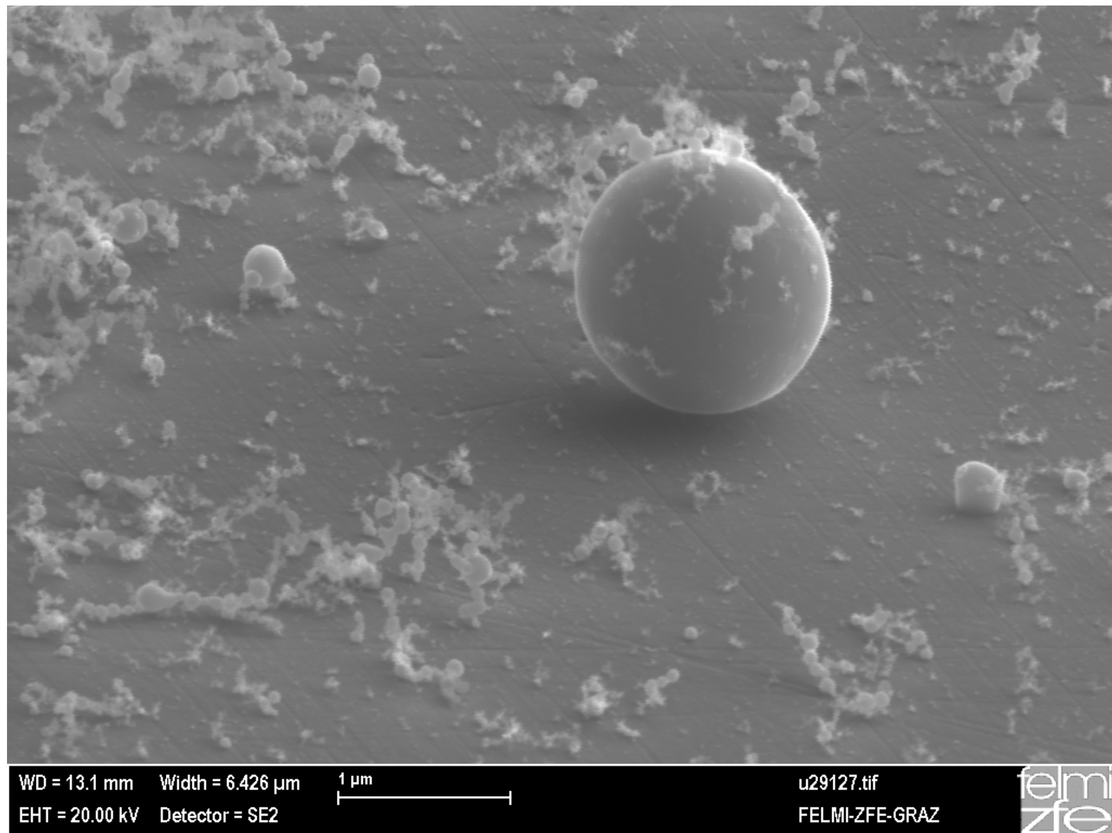

Figure 4-3: SE image of nickel particles on a ferrite substrate.

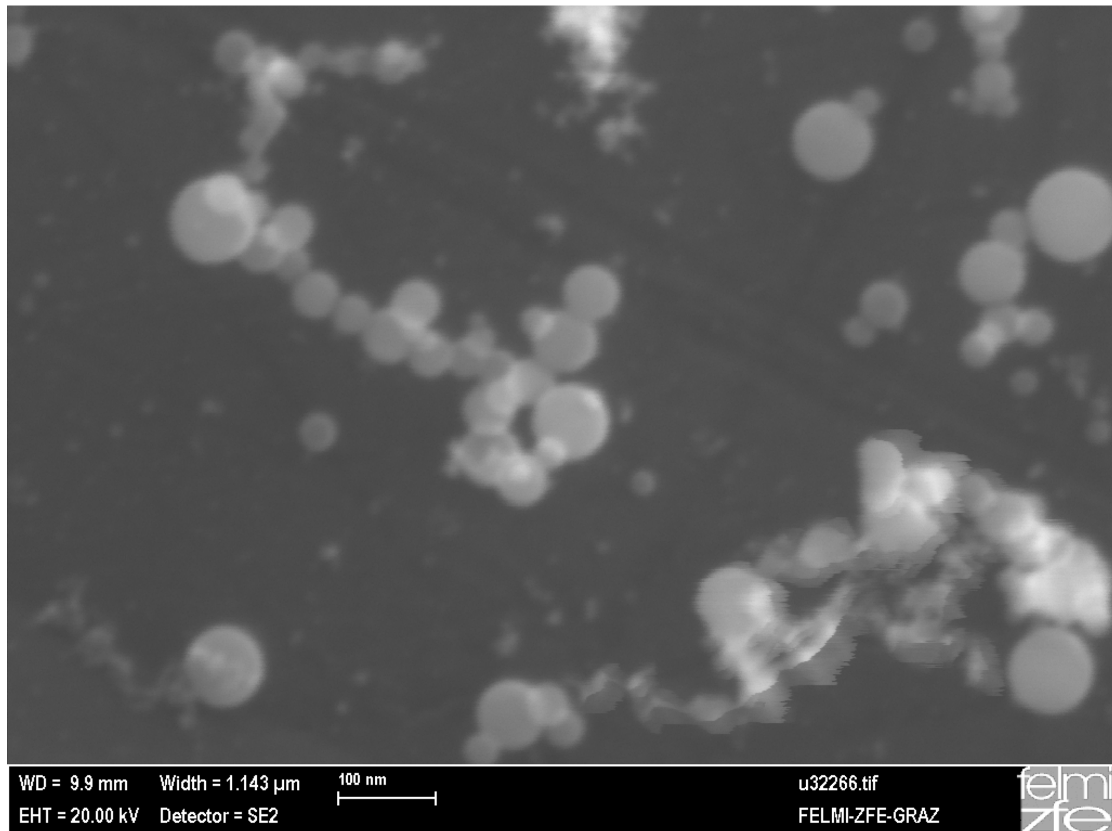

Figure 4-4: Agglomerates of small nickel particles on a silicon substrate.

Measurements and results

First measurements with the particles on ferrite and on the Nucleopore filter produced unsatisfactory diffraction patterns. The reason was that the SEM parameters were not chosen properly. Especially the electron energy of 20 keV used for recording the patterns proved to be too high. An electron energy this high entails an interaction volume between electrons and sample that is much bigger than the size of the nickel particles. This reduces the pattern quality as many of the electrons interact with the substrate and not with the particle itself.

Figure 4-5 shows two Monte Carlo simulations (performed with Casino [11]) for two different electron energies illustrating the depth distributions of the backscattered electrons. In the simulation a 100 nm thick nickel layer on a silicon substrate was used as a model for the specimen. The sample was tilted by 70°, which is the same angle as used for EBSD.

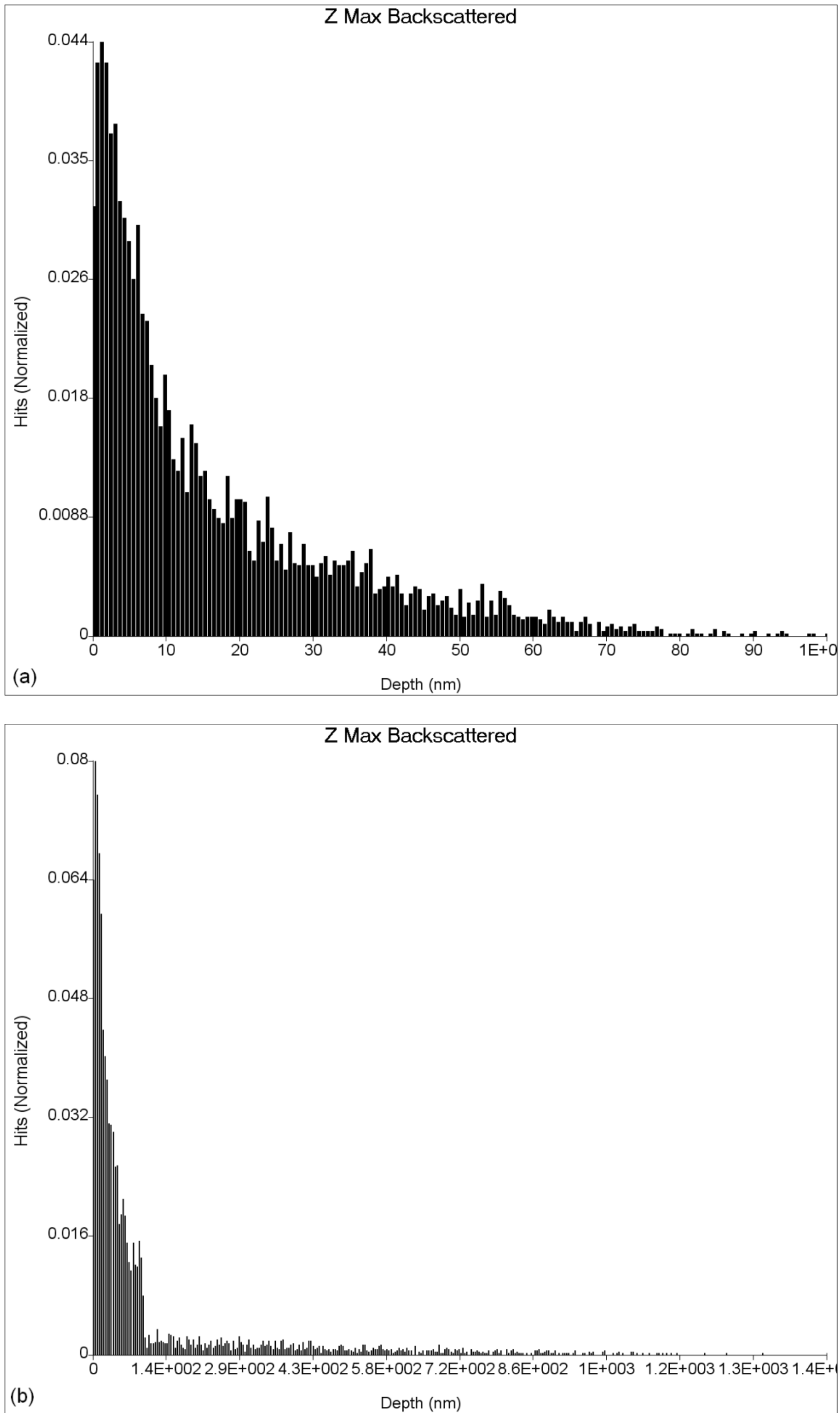

Figure 4-5: Monte Carlo simulation illustrating the depth of the backscattered electrons contributing to the diffraction pattern at an electron energy of (a) 8 keV and (b) 20 keV.

The simulation shows that for an electron energy of 8 keV practically all electrons are scattered within the nickel layer. For 20 keV many electrons pass through the nickel layer and are scattered in the silicon substrate, causing a superposition of the nickel and silicon patterns

To optimize the measurement parameters, the effect of their variation on the quality of the diffraction patterns was investigated using a polished nickel standard.

Figure 4-6 shows the diffraction patterns recorded at different electron energies. The measurement parameters for these diffraction patterns are listed in Table 4-4.

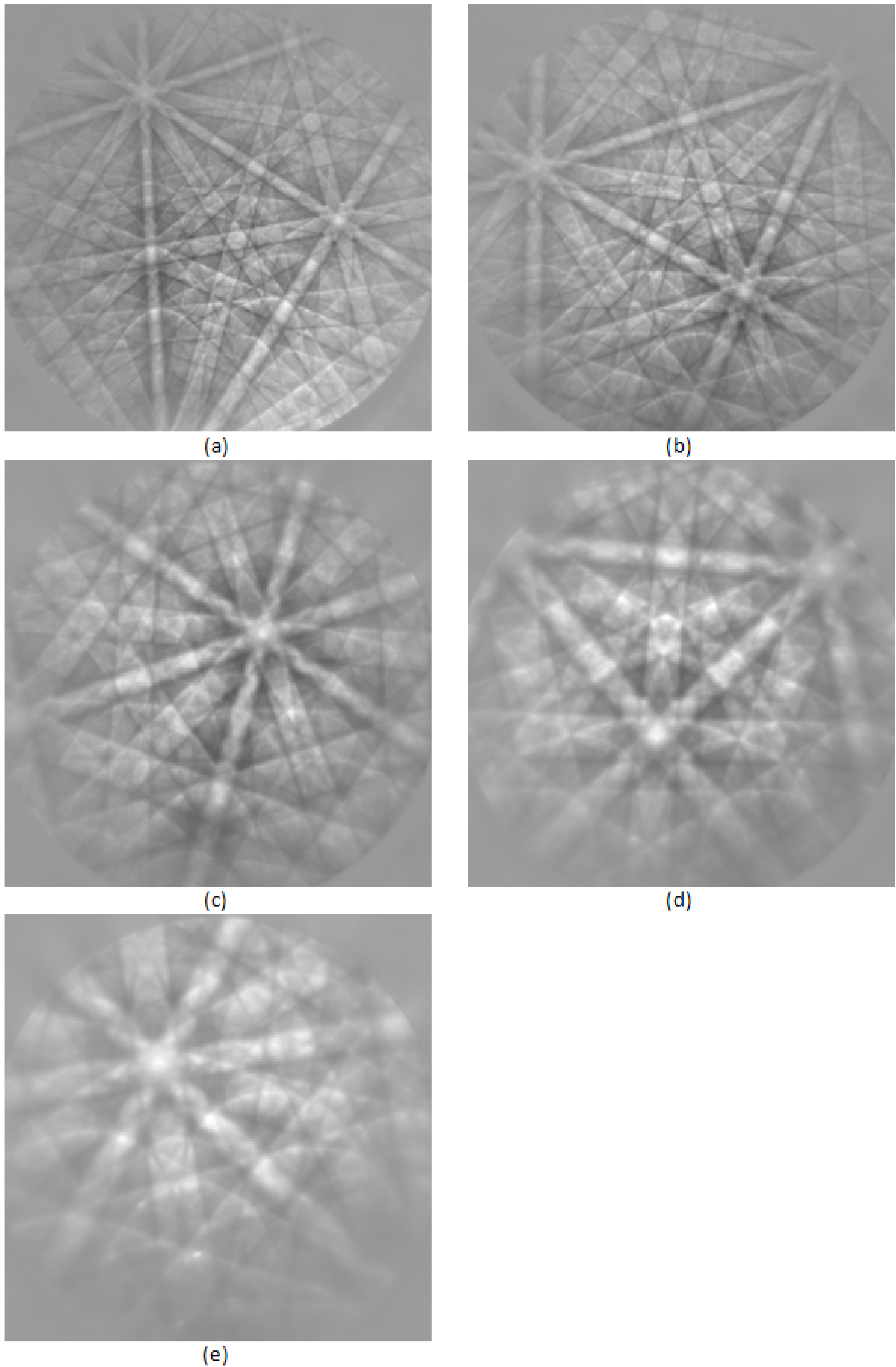

Figure 4-6: Diffraction patterns of a nickel standard recorded with an electron energy of (a) 30 keV, (b) 20 keV, (c) 10 keV, (d) 7 keV and (e) 5 keV.

Table 4-4: Recording parameters for the nickel diffraction patterns.

electron energy / keV	aperture	exposure time / s	picture averaging	background correction	recording time / s
30	60	6.00	46	yes	276
20	120	4.37	64	yes	280
10	60	6.00	64	yes	384
7	60	14.01	16	yes	897
5	240	9.01	64	yes	577

Although Figure 4-6 proves that patterns of a high quality can be recorded with electron energies even as low as 5 keV, it has to be noted that the quality of the diffraction patterns of small particles cannot be expected to be this high. It took several minutes to record a single pattern, which, because of specimen drift, is far too long for recording an EBSD pattern of a small particle. A drift of the electron beam of 80 nm per minute was measured at an electron energy of 10 keV. This clearly limits the possible measurement time.

At this point a second wire explosion experiment had been finished and a new sample was available with a silicon wafer as substrate. Further measurements were performed with this new specimen. Figure 4-7 shows the diffraction pattern of the silicon wafer itself recorded with an electron energy of 10 keV.

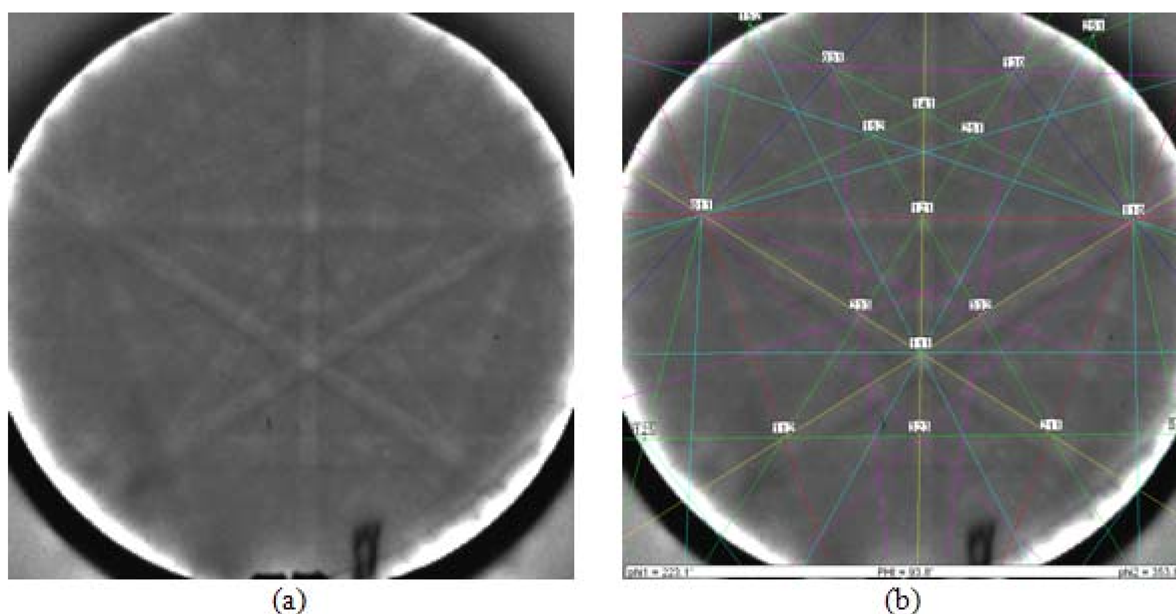

Figure 4-7: (a) Diffraction pattern of silicon recorded with an electron energy of 10 keV and an exposure time of 0.86 s; (b) indexed diffraction pattern of silicon.

Subsequently EBSD patterns of nickel particles were recorded (Figure 4-8).

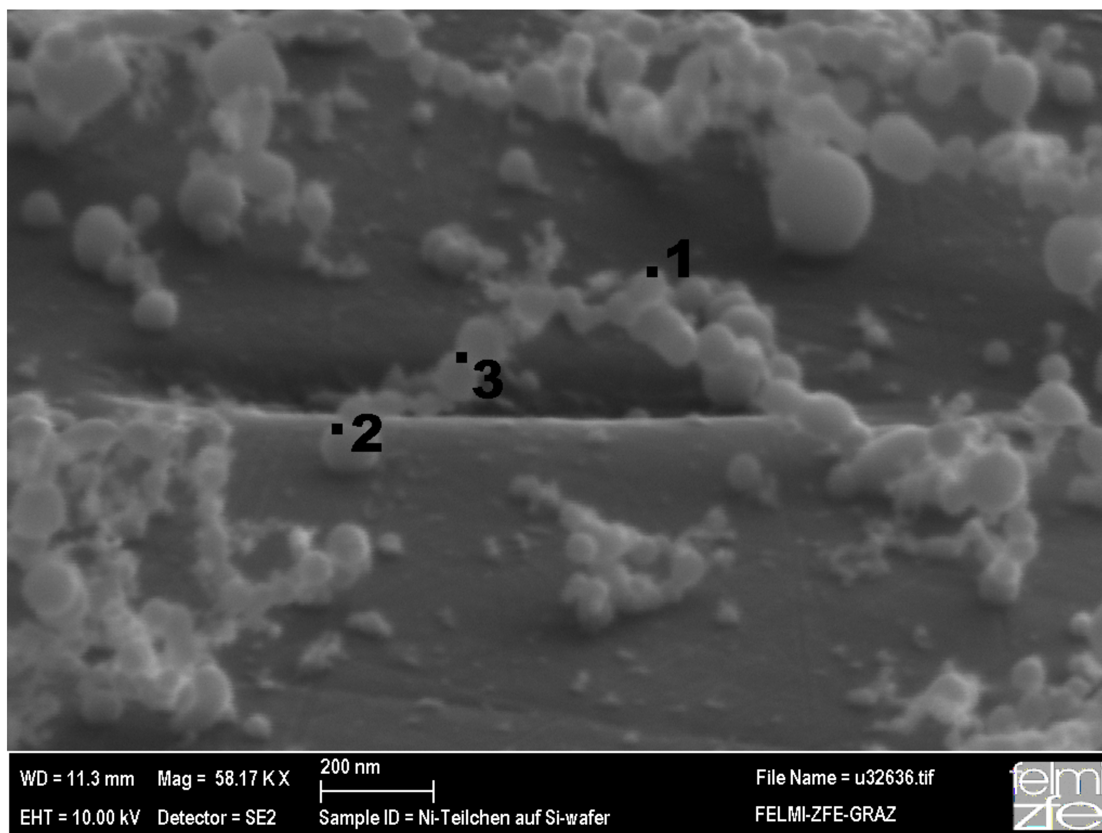

Figure 4-8: SEM image of a nickel particle conglomerate.

The particle at measurement point 3 has a diameter of 80 nm. This is the smallest particle for which a recognizable diffraction pattern could be recorded. This diffraction pattern is shown in Figure 4-9. In similar measurements done by Small et al., it was possible to obtain useable diffraction patterns from Fe-Co Particles with diameters as small as 120 nm. [12]

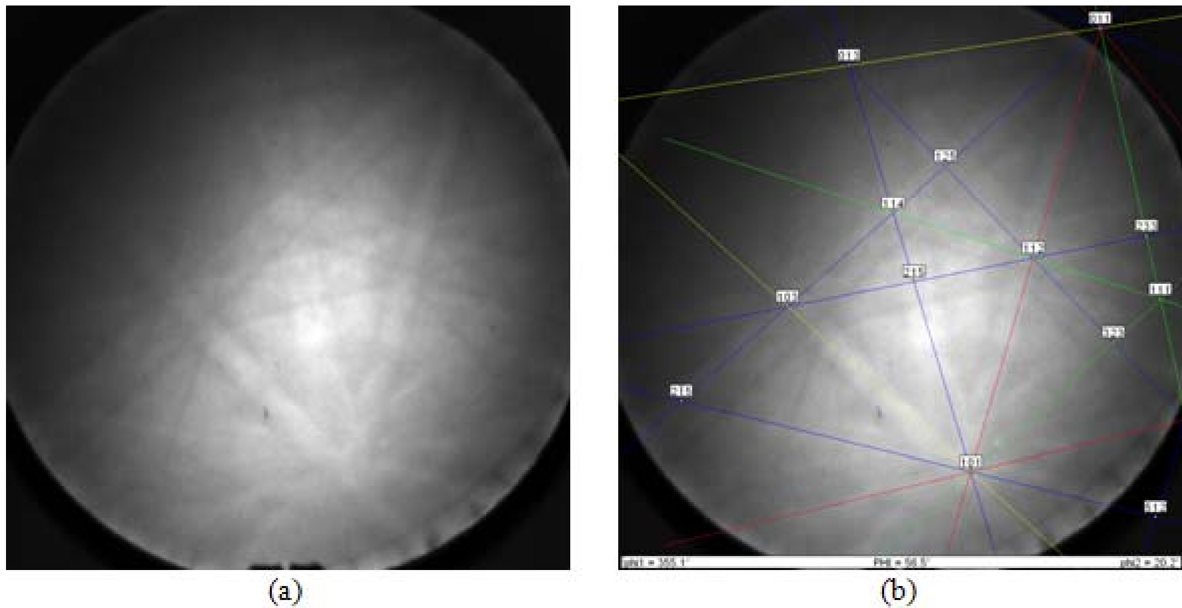

Figure 4-9: (a) Diffraction pattern of nickel taken with an electron energy of 10 keV and an exposure time of 0.86 s; (b) indexed diffraction pattern of nickel.

4.1.3 Nickel nanowires in a porous silicon matrix

Specimen

The specimen was an etched silicon wafer with spatially homogenous distributed pores oriented perpendicularly to the surface. The samples are by courtesy of P. Granitzer [13], [14]. The pores are generally 20 to 30 micrometres long and have diameters in the range of 60 nm. The pores were partially filled with nickel in an electrochemical precipitation process. The result is a nanocomposite system consisting both of the silicon matrix and Nickle nanowires as can be seen in Figure 4-10. The goal was to examine if EBSD patterns can be recorded from the nanowires as their sizes are close to that of the smallest Nickle particles that could be indexed in the previous chapter, and to find out whether they are monocrystalline or polycrystalline.

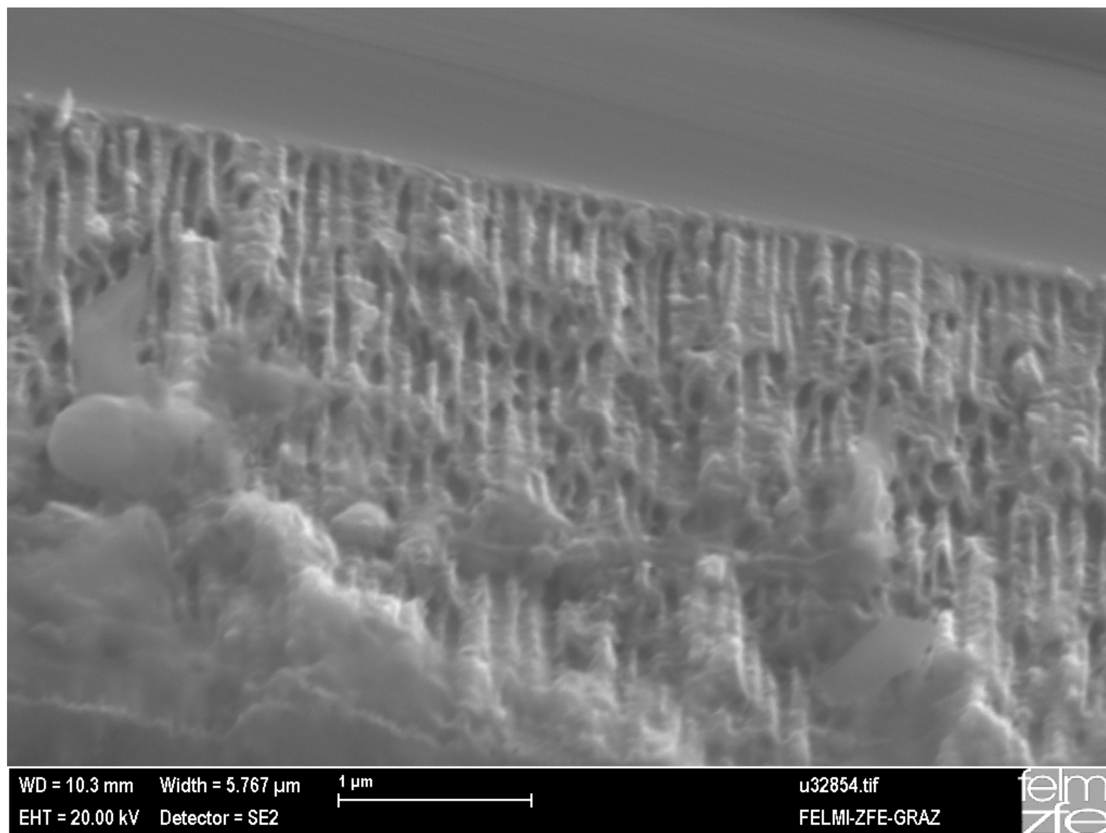

Figure 4-10: Porous silicon with nickel nanowires.

Measurements and results

Measurements were carried out with an electron energy of 8 keV. Figure 4-11 shows a BSE image of the specimen with the labeled locations of two measurement points on a nanowire.

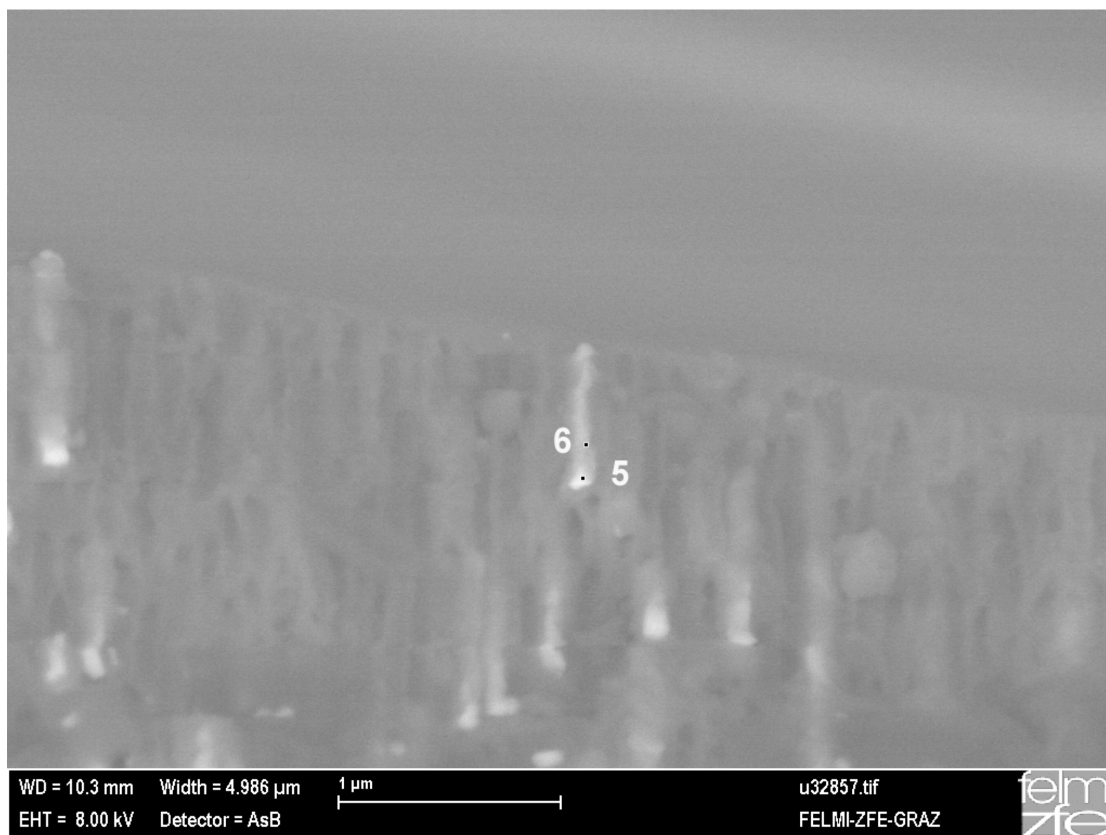

Figure 4-11: BSE image of nickel nanowires (bright streaks) in a porous silicon matrix.

Due to the small size of the particles and the short integration times (specimen drift!) the contrast in the patterns is weak. Because of their irregular structure the diffraction patterns gathered from the nanowires (see Figure 4-12) could not be clearly identified as nickel diffraction patterns by the automated indexing software. They also show a clear superposition with the diffraction pattern of silicon (Figure 4-13).

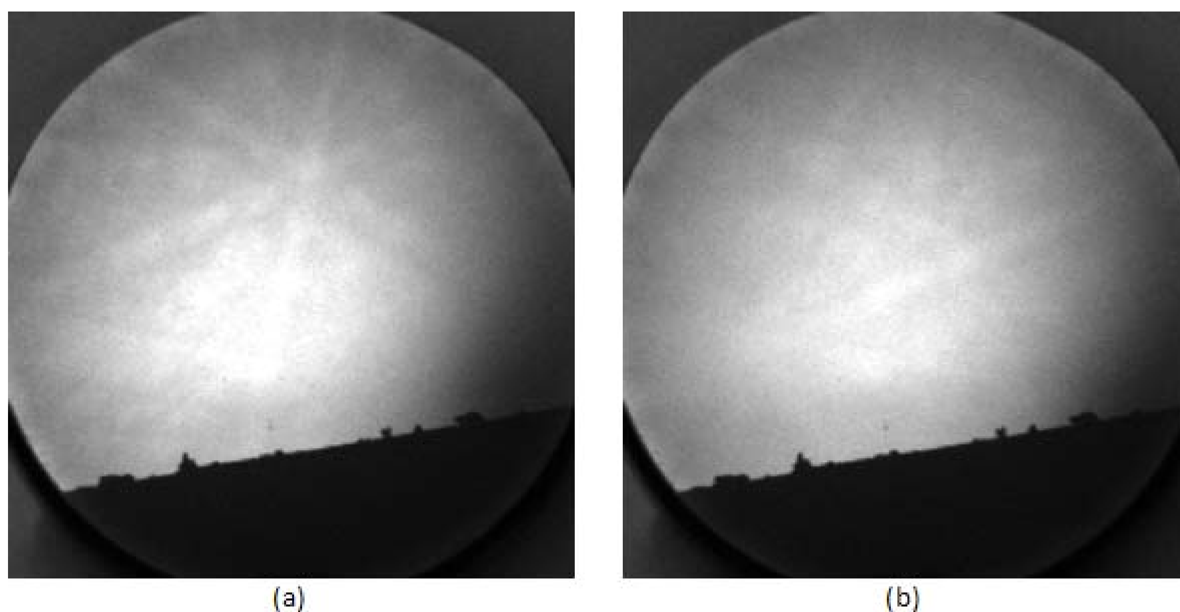

Figure 4-12: Diffraction patterns of a nickel nanowire taken at point (a) 5 and (b) 6.

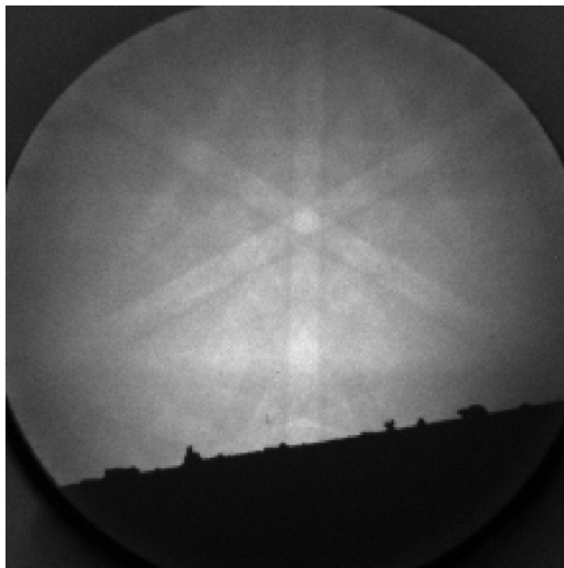

Figure 4-13: Diffraction pattern of the porous silicon matrix.

The quality of the diffraction patterns was enhanced by the use of image processing:

- Background subtraction by Fourier transformation (high pass filtering with a cutoff frequency of 5)
- Contrast and brightness enhancement
- Filtering with a mean filter (mask size: 5)

Subsequently, after manually defining some of the bands in the patterns, the indexing of both the patterns of the nickel particles and the silicon substrate was possible. The results are shown in the following pictures (Figure 4-14, Figure 4-15 and Figure 4-16).

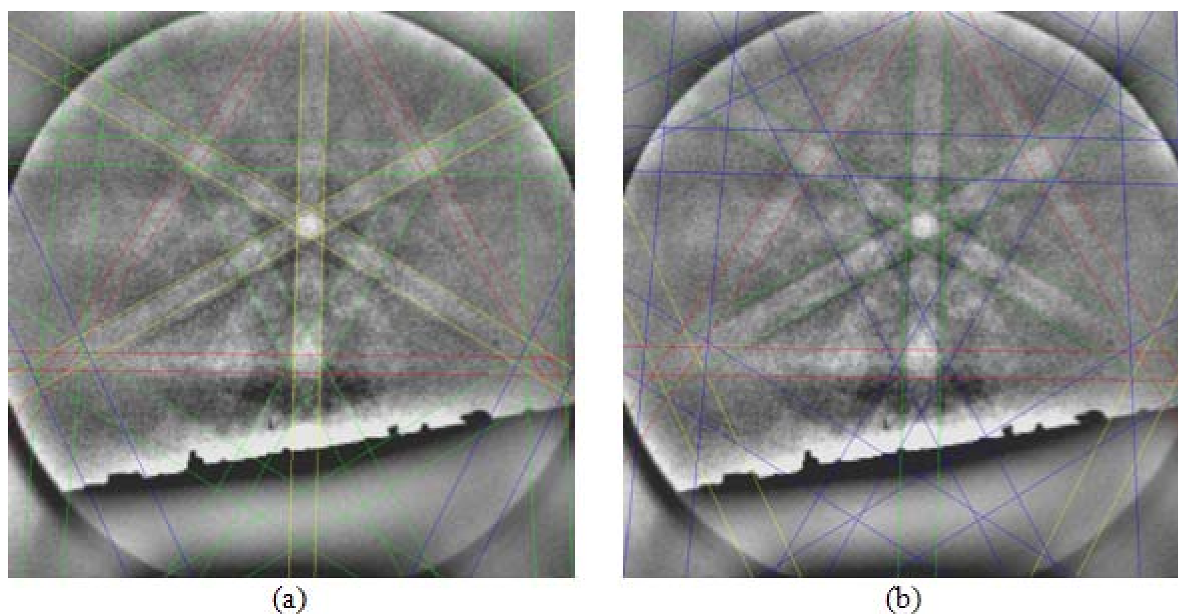

Figure 4-14: Diffraction pattern of the porous silicon matrix after image processing indexed for (a) silicon and (b) nickel.

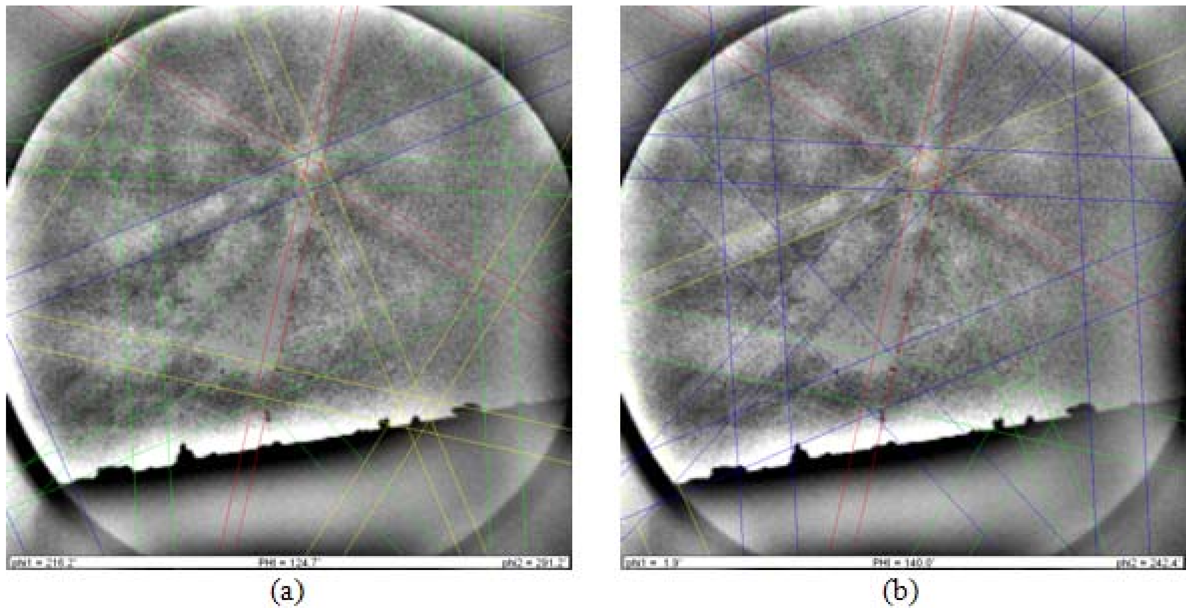

Figure 4-15: Diffraction pattern of the nickel nanowire at point 5 after image processing indexed for (a) silicon and (b) nickel.

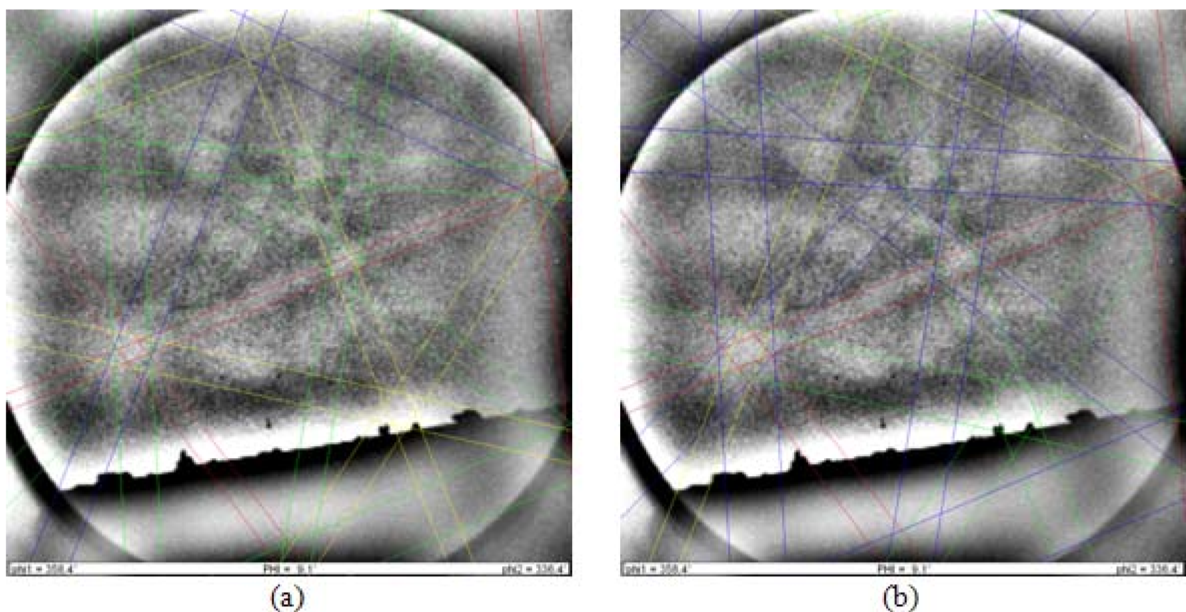

Figure 4-16: Diffraction pattern of the nickel nanowire at point 6 after image processing indexed for (a) silicon and (b) nickel.

Although the positions of the nickel and silicon bands are very similar, their bandwidths are different. A closer look at the diffraction pattern of silicon (Figure 4-14) shows that the indexation with nickel does not work because some of the bandwidths are too high. The indexation with silicon on the other hand seems to fit the measured pattern.

The two diffraction patterns gathered from the nickel nanowire cannot be indexed as silicon because some of the bandwidths here are too small. The indexations with nickel seem to be a better match in these cases.

Even though the indexing of the diffraction patterns of the nickel nanowire is difficult, they are distinguishable from each other and from the diffraction pattern of the silicon matrix.

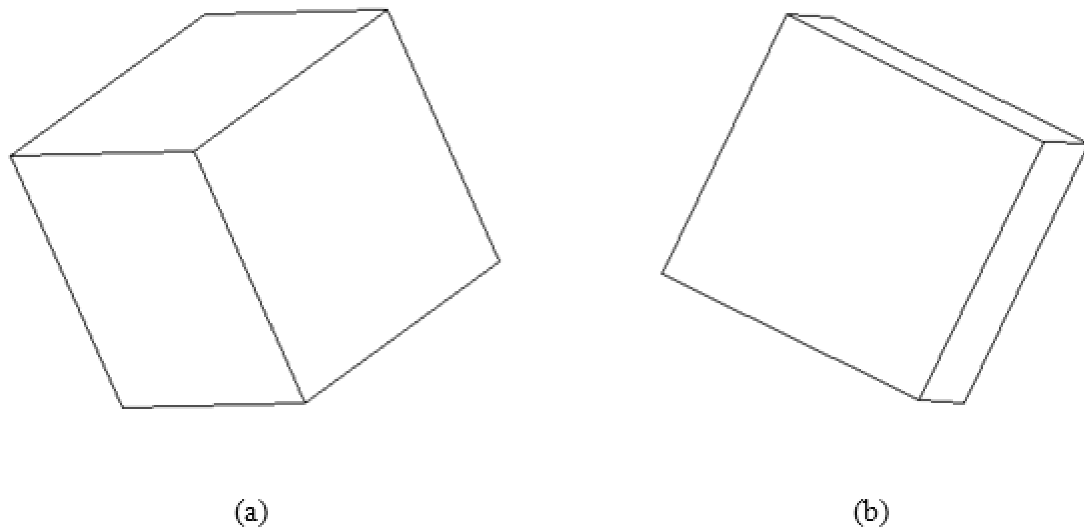

Figure 4-17: Wireframes showing the crystal orientations of the nanowire at the measurement points (a) 5 and (b) 6.

Figure 4-17 shows a wireframe representation of the crystal orientation of the nanowire at the points 5 and 6. These results indicate that the nickel nanowires are not monocrystalline but polycrystalline. Still, one has to be aware that these nanowires are not flat specimens and thus the tilt angle during EBSD measurement is not necessarily 70°. This could influence the orientation measurements.

4.2 EBSD measurements of high pressure torsion deformed nickel

4.2.1 Specimen

All four specimens were made of nickel with a purity of 99.99+%. They were deformed using the method of high pressure torsion (see [15]) and reached high Mieses strains ($\varepsilon = 30$) and small average grain diameters (260 nm). The four specimens experienced different temperature treatments and therefore had different grain structures. The specimens are by courtesy of R. Würschum, Institut für Materialphysik, TU Graz. [16]

The embedded specimens were Silica-polished and partly coated with electrically conductive paint to reduce charging effects in the SEM caused by the resin (see Figure 4-18).

It was tried to determine the average grain diameters by analysis of BSE images, using image processing. These images could not be analyzed using automated pattern recognition and therefore the grain boundaries had to be thickened manually with a pen. In order to get good statistics for the grain diameter distribution, the number of measured grains had to be high and so those analyses were quite time-consuming.

It was tested whether EBSD measurements could be a useful alternative for the determination of the grain size distribution. The main challenges were the small grain size and the assumed high stresses within these grains. It was not clear if EBSD could produce useable results for these specimens.

Figure 4-18: Embedded high pressure torsion deformed nickel specimens labeled 1 to 4.

4.2.2 EBSD measurements

EBSD area scans were performed for all four specimens. The parameters for these scans are listed in Table 4-5.

Table 4-5: EBSD measurement parameters.

specimen	scan area / µm²	step size / µm
1	20x20	0.05
2	10x10	0.05
3	30x30	0.10
4	40x40	0.25

For reasons of comparison a BSE image was taken at the same area of the specimen where an EBSD map was recorded.

4.2.3 Results and discussion

Figure 4-19 shows the EBSD scans of the four specimens. The measurements and the determination of the average grain diameter could be performed without any problems. Stresses within the grains were not as high as assumed and therefore the measurements went more smoothly than expected. The mean grain diameters are listed in Table 4-6 together with the mean grain diameter for specimen 1 which was obtained using BSE images. [16]

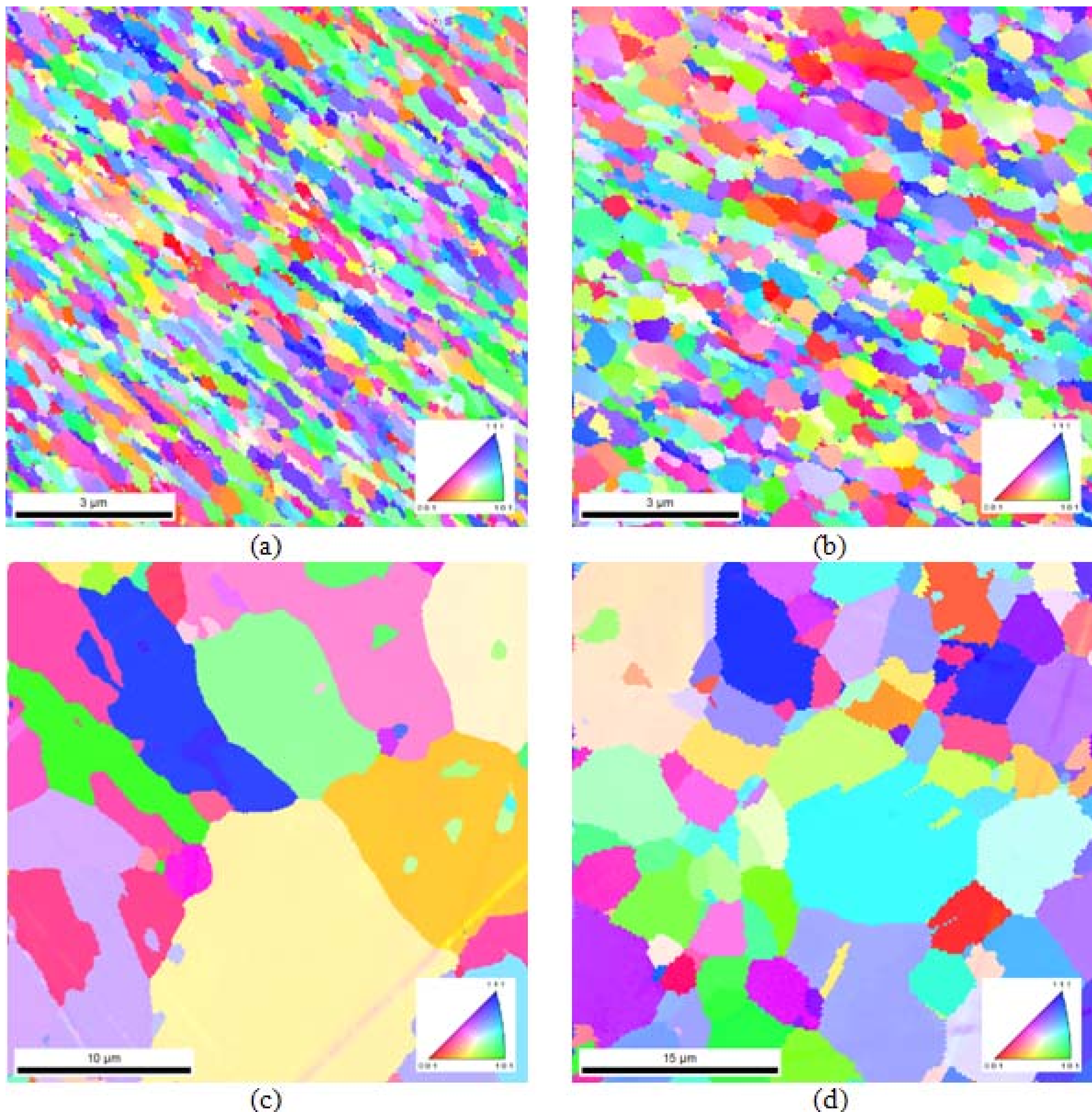

Figure 4-19: Inverse pole figure maps of (a) specimen 1, (b) specimen 2, (c) specimen 3 and (d) specimen 4; inset: color code for crystal orientations.

Table 4-6: Mean grain diameters of four high pressure torsion deformed nickel specimens.

specimen	EBSD mean grain diameter / nm	BSE mean grain diameter / nm	number of analyzed grains
1	250	260	5456
2	260	-	1210
3	*	-	79*
4	*	-	143*

* number of analyzed grains to small for grain size determination

Specimens 1 and 2 have about the same grain size. The mean grain diameter for specimen 1 fits to the results obtained from BSE images. Figure 4-20 shows the grain orientation spread for both specimens. High grain orientation spread is usually related to stresses within the grains. The spread is similar for both samples and it is rather low.

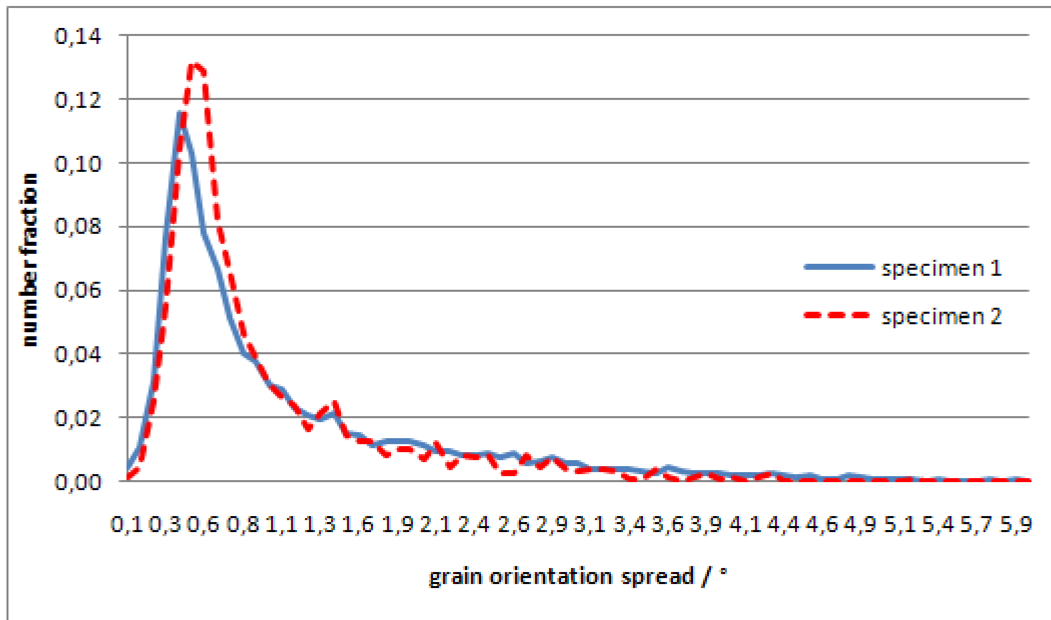

Figure 4-20: Distribution of the grain orientation spread for specimen 1 and 2.

Figure 4-21 shows a comparison between an EBSD map and a BSE image taken at the same area of specimen 1.

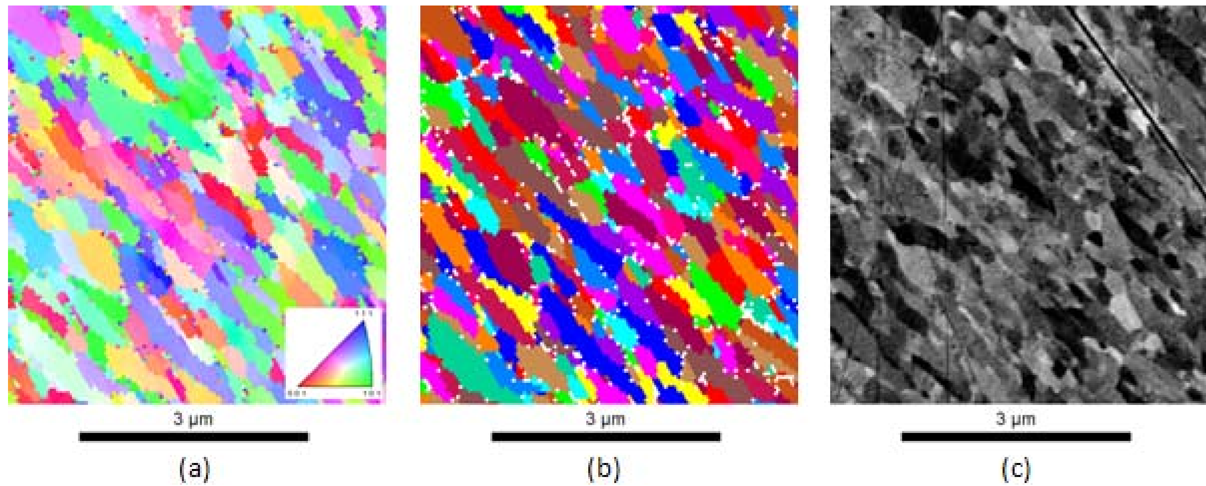

Figure 4-21: Specimen 1: Comparison between (a) inverse pole figure map from EBSD, (b) grain distribution map from EBSD and (c) BSE image. The inset in (a) is the color code for the crystal orientations.

With EBSD mapping the grains can be distinguished easily. In the BSE image the contrast differences between grains are not always big enough to allow a clear identification of grain boundaries. Although the results for the mean grain diameter are nearly the same with both methods, the better quality of the EBSD images suggests that the results obtained by the use of EBSD are generally more accurate.

In addition this method is often less time consuming than the analysis of BSE images.

4.3 Investigation of micro-cracks via 3D-EBSD

4.3.1 Specimen

The specimen used was cut from an alloy 80A disc, which had undergone a compression test at a temperature of 1000°C (see Table 4-7). Before this compression test it had a diameter of 16 mm and a height of 24 mm.

Table 4-7: Processing parameters of the compression test for alloy 80A. [17]

temperature / °C	final height / mm	maximum force / kN	die speed / mm/s	true strain	average true strain rate / 1/s
1000	13.7	75.9	6.7	0.56	0.39

After testing, the compressed disc was cut to a transversal cross section at half its height. The disc was cut in half again (transversal cross section) and was embedded in resin for further preparation (Figure 4-22).

20 Vickers indentations were made on the surface marking several micro-cracks. An EBSD scan was made of the area surrounding crack C1 (Figure 4-23) [17].

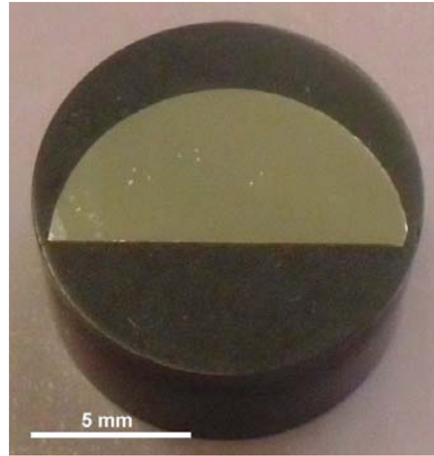

Figure 4-22: Embedded alloy 80A specimen.

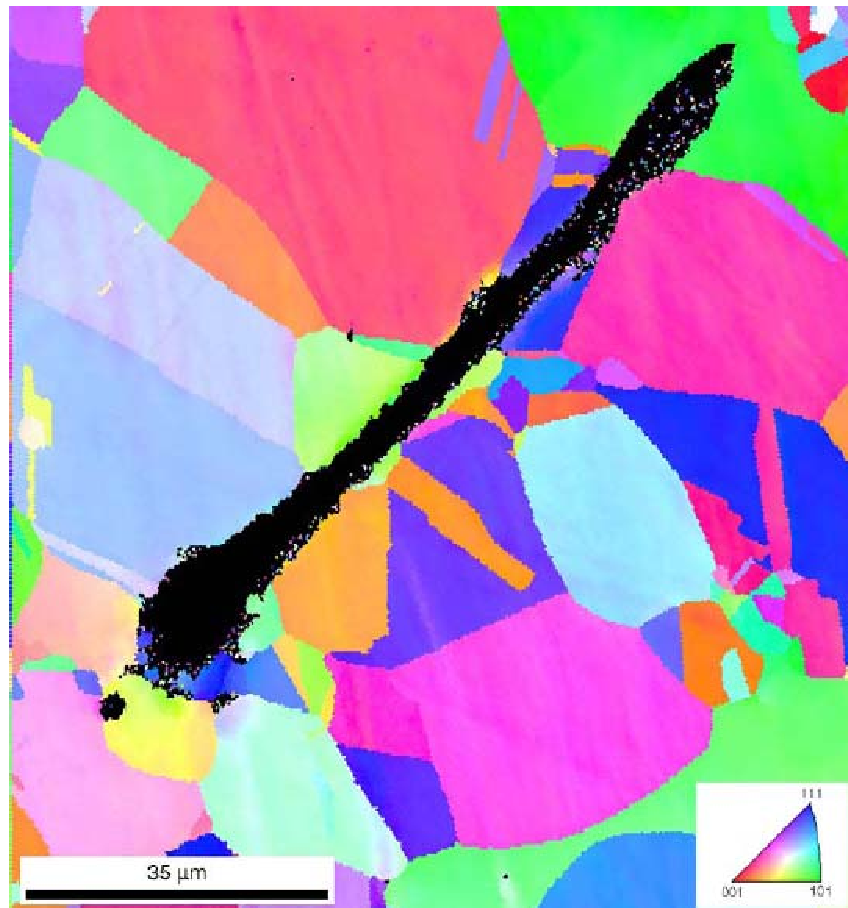

Figure 4-23: Inverse pole figure map at a transversal cross section of the specimen; inset: color code for crystal orientations. [17]

The crack C1 seems to pass through several recrystallized grains. Also the crack stops in recrystallized grains. This indicates that recrystallization had happened before the formation of the crack.

Figure 4-24 shows the recrystallization mechanism according to literature starting at grain boundaries of mother grains. The recrystallization continues regularly until the mother grains are “eaten up”. This is called necklace or cascade recrystallization. [18]

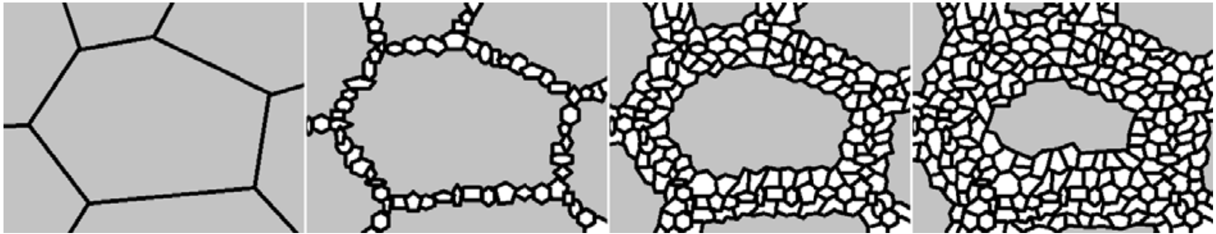

Figure 4-24: Schematic of the necklace type recrystallization mechanism.

Figure 4-25 shows the schematic of a similar mechanism. The difference here is that the recrystallization happens irregularly and “fingers” of recrystallized grains are formed that reach into the mother grains.

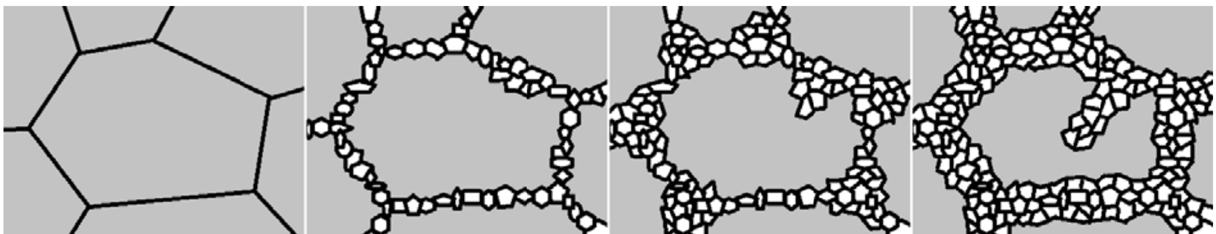

Figure 4-25: Schematic of the finger type recrystallization mechanism.

If such structures are observed at a single cross section cut at an angle approximately perpendicular to that finger, one might assume, that recrystallization happened also in the middle of a mother grain. With 3D-EBSD measurements such a faulty conclusion could be prevented.

4.3.2 Serial sectioning measurements

The specimen was sectioned 21 times. The progresses of the crack in Figure 4-23 (labeled C1) and 8 additional cracks (labeled C2 to C9) were investigated. After each sectioning step EBSD scans were made for the areas surrounding the cracks. The size of the scanned areas for C1, C2, C4, C6, C7 and C8 was 200x200 µm, that of the scanned areas for C3, C5 and C9 was 300x300 µm. All scans were performed with a step size of 1.0 µm. In addition to the 20 already existing indentations, 19 new Vickers indentations

were made in 4 series. As described above these indentations were essential for the determination of the thickness of the removed layers.

As the cracks C1 to C9 were on different surface areas, the abrasion values differed. All preparation parameters and abrasion values are summarized in Table 4-8. Due to unsatisfactory surface qualities in earlier sectioning steps longer preparation times were chosen in later sectioning steps.

Table 4-8: Preparation parameters and abrasion values for alloy 80A.

step	preparation time / min			abrasion / µm								
	grinding	C-polishing	Si-polishing	C1	C2	C3	C4	C5	C6	C7	C8	C9
0	0	0	30	-	-	-	-	-	-	-	-	-
1	4	4	30	3.0	-	-	-	-	-	-	-	-
2	12	4	30	1.3	5.3	1.3	2.9	-	4.6	-	-	-
3	6	4	90	1.7	4.5	-	2.8	1.5	3.8	4.5	4.7	-
4	4	4	60	0.4	1.7	-	1.2	0.5	1.7	2.0	1.7	-
5	4	8	90	1.4	2.1	3.3	1.9	1.3	2.1	2.3	2.3	-
6	4	4	90	0.4	1.8	0.2	1.0	0.2	1.6	1.9	2.2	-
7	4	8	90	0.3	1.5	2.6	0.5	0.8	0.6	0.8	2.0	-
8	4	12	90	-	1.7	2.0	0.6	0.8	1.1	2.0	-	-
9	4	12	90	-	3.7	4.4	2.6	1.9	2.9	3.3	-	-
10	4	12	90	-	1.2	2.3	1.0	1.6	0.9	1.6	-	-
11	4	12	90	-	-	-	5.3	3.5	7.1	8.2	-	7.1
12	4	12	90	-	-	-	3.5	3.8	3.9	4.2	-	3.9
13	4	12	90	-	-	-	1.2	1.4	1.9	2.9	-	1.9
14	4	12	90	-	-	-	0.8	0.3	1.1	1.5	-	1.1
15	4	12	90	-	-	-	0.7	1.3	-	-	-	1.6
16	4	12	90	-	-	-	2.3	2.7	-	-	-	2.3
17	4	12	90	-	-	-	0.9	-	-	-	-	1.1
18	4	12	90	-	-	-	1.5	-	-	-	-	2.5
19	4	12	90	-	-	-	2.2	-	-	-	-	2.3
20	4	12	90	-	-	-	0.7	-	-	-	-	1.0
21	4	12	90	-	-	-	1.7	-	-	-	-	-

4.3.3 Results and discussion

In this chapter only some exemplary pictures are shown. The complete picture series for the cracks C1 to C9 are presented in the Appendix.

Crack C1

Looking at Figure 4-23, one can see that the crack propagates through some recrystallized grains. Following scans showed that none of these grains are torn apart completely, which was unexpected (see Figure 4-26). The fact that these grains were not completely fractured indicates that they might have had a stopping effect on the crack propagation. This is an example that shows the benefits of a 3D-representation compared to a single 2D-image. The latter might lead to faulty conclusions.

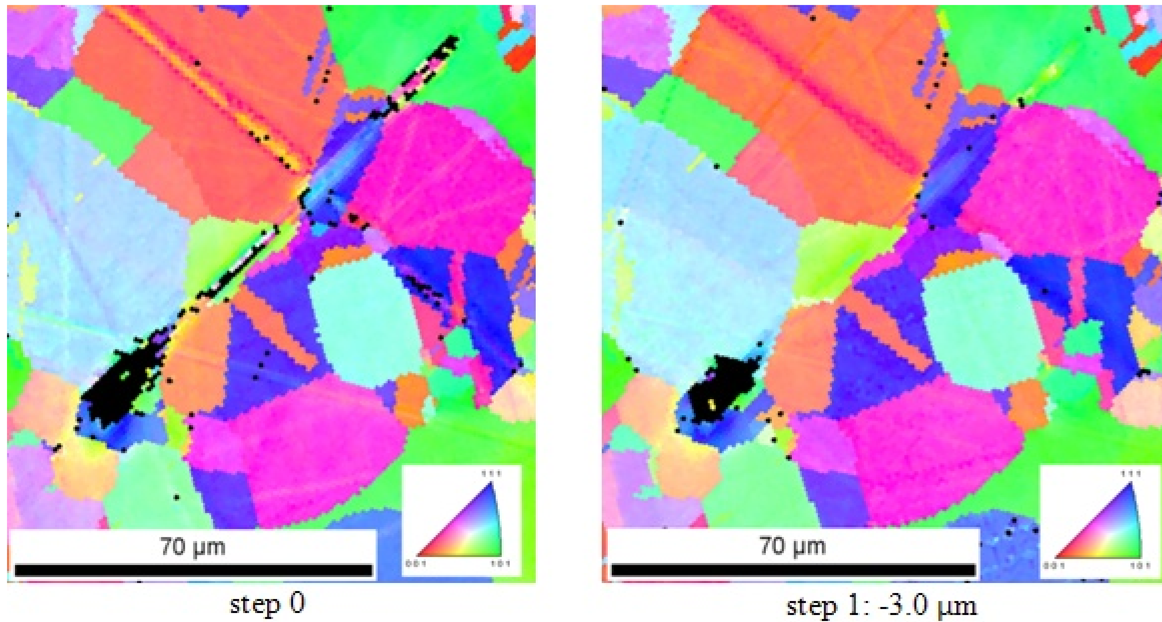

Figure 4-26: Inverse pole figure maps of the area surrounding crack C1 at step 0 and step 1; inset: color code for crystal orientations.

Cracks C2 to C9

There are always recrystallized grains at the tips of the cracks (see for example Figure 4-27). This also supports the theory presented above that the recrystallized grains have a stopping effect on the cracks.

The cracks are always lokcated between unrecrystallized grains (see e.g. Figure 4-27).

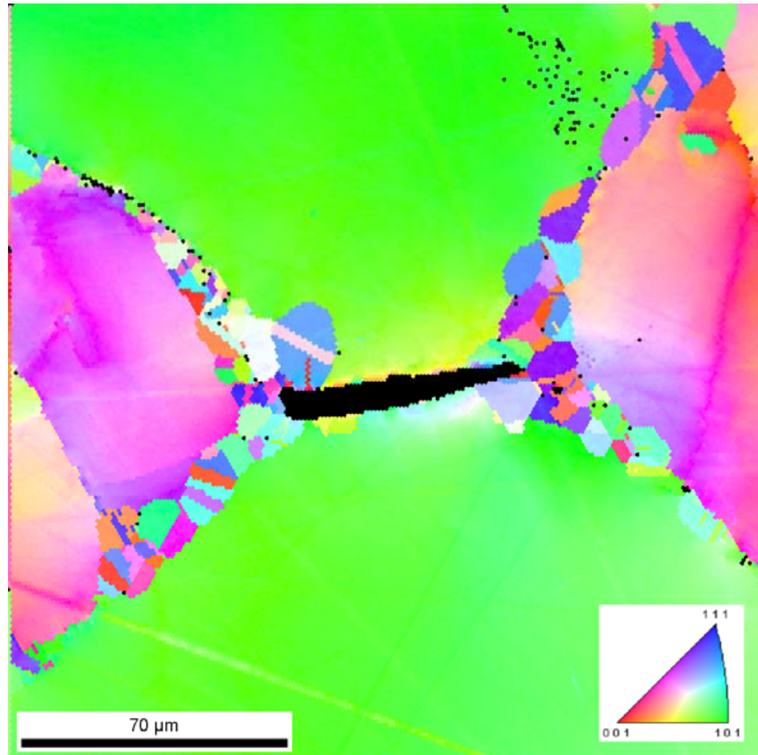

Figure 4-27: Inverse pole figure map of the area surrounding crack C6 at step 3; inset: color code for crystal orientations.

The cracks are not completely surrounded by recrystallized grains. Unrecrystallized grains in direct neighborhood of cracks nearly always show a strong grain orientation spread close to the crack. This is generally caused by high strains linked with high numbers of dislocations in the crystal lattice of the grain. The formation of the crack did not reduce the stress in its surrounding. This strong grain orientation spread does not appear if already recrystallized grains have formed between the crack and the nearest still unrecrystallized grain.

An example is given by crack C7, visible in Figure 4-28.

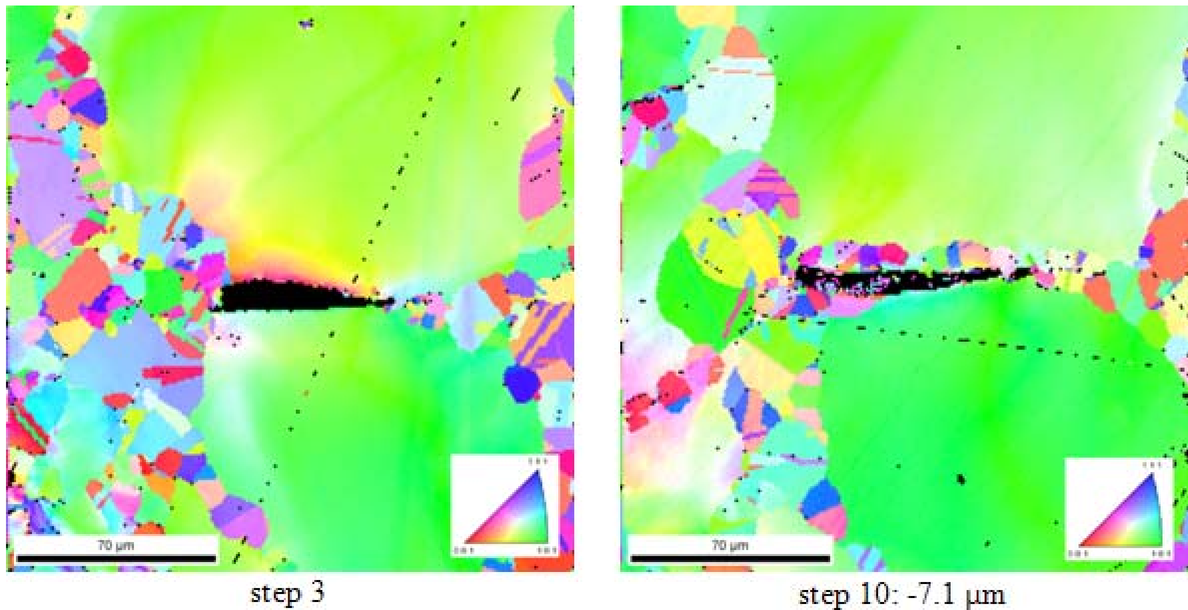

Figure 4-28: Inverse pole figure maps of the area surrounding crack C7 at step 3 and step 10; inset: color code for crystal orientations.

The recrystallization mainly took place at the grain boundaries of the large unrecrystallized grains. Recrystallization at low angle grain boundaries was not observed.

Some examples of recrystallization within mother grains were found (Figure 4-29). This is possibly linked to the formation of carbides. [17]

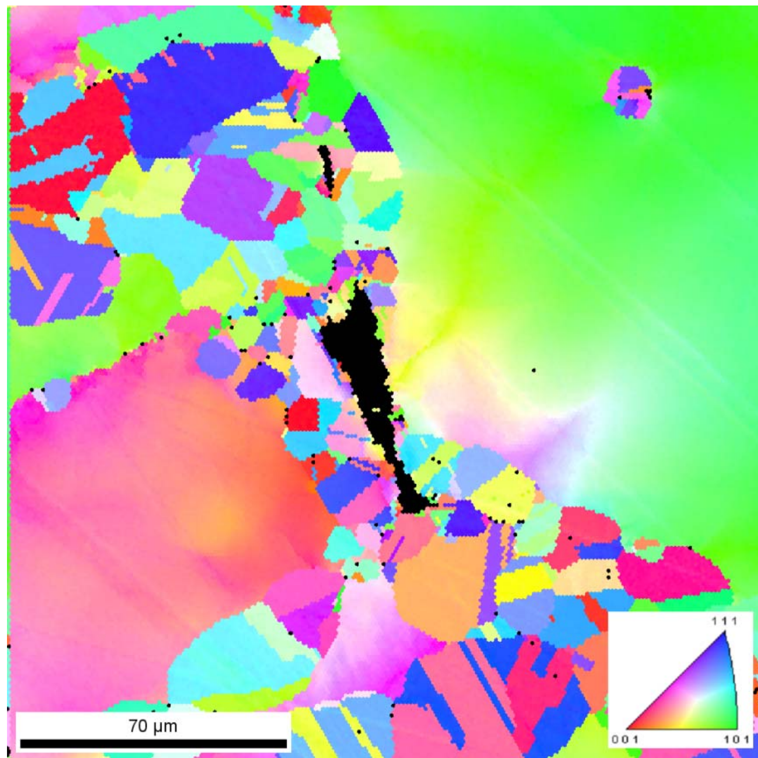

Figure 4-29: Inverse pole figure map of the area surrounding crack C4 at step 13; inset: color code for crystal orientations.

Similar to this, seemingly isolated recrystallized grains formed in the interior of original grains were observed in step 10 of crack C3. Looking at the other scans of this area, it is clear that these grains are linked to a larger assembly of interconnected recrystallized grains contacting somewhere near the grain boundary of the original unrecrystallized grain. Thus the progress of the recrystallization in this case would not follow a necklace type route. This is another example showing the advantages of a 3D-representation of the interior structure of the material under investigation.

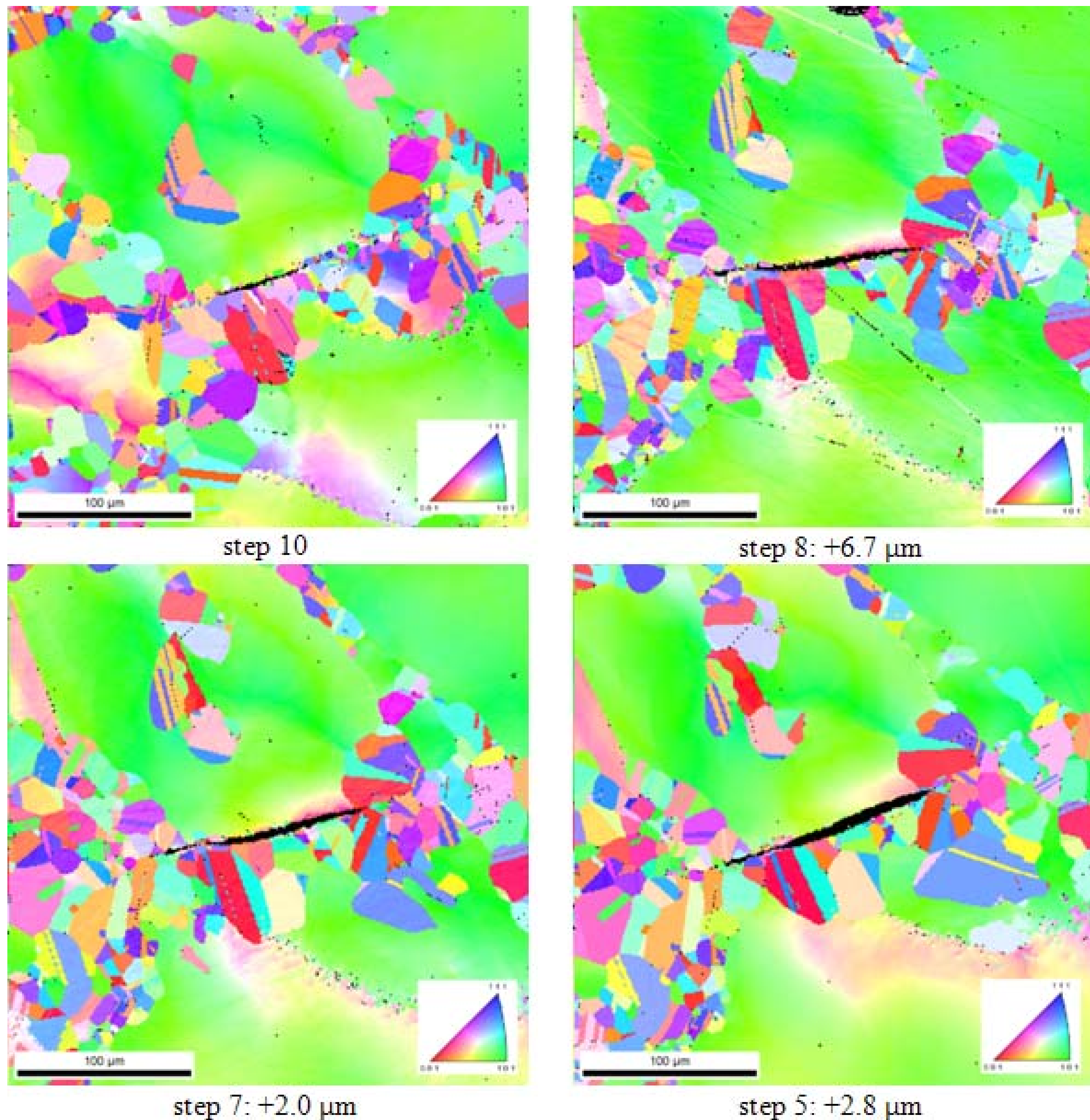

Figure 4-30: Inverse pole figure maps of the area surrounding crack C3 at step 5, 7, 8 and 10; inset: color code for crystal orientations.

3D EBSD

Finally it has to be added that a 3D rendering of the cracks and the surrounding grains was not possible because of some experimental problems. On the one hand the thicknesses of the sectioning steps varied too much and on the other hand the single maps showed distortions probably linked to slight errors of the tilt and rotation angles during measurement (see chapter 2.1.2).

5 Summary

The scope of this master thesis was to investigate both fundamental and experimental problems arising in connection with electron backscatter diffraction measurements (EBSD) in a scanning electron microscope (SEM). Another aim was to explore the accuracy of the measured and calculated data in dependence on the chosen instrumental parameters. Parameters that are necessary for the data analysis - and can be freely chosen – can also substantially influence the outcome. A variety of materials was used to find the basic limitations of the method and determine the minimum size of structures that can be analyzed by EBSD in SEM. Also a preparation method was developed and tested to extend the measurements from two to three dimensions.

A basic investigation of EBSD showed some problems which arise in all measurements. It was shown that small changes of parameters determining the orientation of the specimen surface relative to the phosphor screen can cause severe distortions in orientation imaging microscopy (OIM) and considerable inaccuracies of the measured crystallographic orientations. Such variations can, apart from an inaccurate adjustment of the experimental parameters, for example also be caused by a rough specimen surface.

The investigation of the processing of the data of OIM maps focused on grain size determination. Three parameters were varied: step size (distance between the measured points in the map), minimum grain boundary misorientation angle (used for definition of the grain boundaries) and minimum number of points per grain. For a fixed magnification the step size and the number of grains are of course connected with each other. It was studied how variations of these parameter affected the measured grain sizes.

The minimum grain boundary misorientation angle was varied between 5° and 25°. The results of the measured steel and ferrite samples showed a maximum variation of the calculated average grain diameter of 18%. It seems obvious that there should be a standard value for the minimum grain boundary misorientation angle which should be used in all analyses, but which at present does not exist. This would improve the comparability of different measurements.

The variation of the step size parameter showed two basic problems. A very large step size could cause small grains to be excluded from the analysis, whereas a very small step size would cause long measurement times. The goal of this investigation was to find rules to choose an ideal step size for the grain size determination of a given sample. The analysis of a ferrite sample showed another unexpected problem. At very small step sizes, the orientation of points close to grain boundaries could not be determined accurately due to the superposition of diffraction patterns from the two neighboring grains. Therefore they were sometimes interpreted as very small grains and this greatly affected the measured mean grain diameter. But this problem itself is correlated with the choice of the minimum number of points per grain and can be avoided by choice of a sufficiently high value for this parameter. Finally, an approximately ideal step size was proposed for samples with a given grain size distribution.

Part of the experimental studies was to find the minimum size of particles that can be analyzed by EBSD. Measurements of different mineral particles proved to be problematic for several reasons. Production of small particles by ball milling induced high stresses in the particles. But also specimen damage caused by electron irradiation can prevent the recording of useable EBSD patterns.

Nickel particles from wire explosions on different substrates, both crystalline and amorphous ones, were investigated. It was possible to index the diffraction patterns of particles with diameters as small as 80 nm. Finally nickel nanowires (diameter ~ 60nm) in a porous silicon matrix were investigated. The goal of these measurements was to clarify if the nanowires are mono- or polycrystalline. Pattern analysis had to be done manually because the quality of the diffraction patterns was too poor both due to the small diameters of the nanowires and the superposition with the EBSD pattern produced by the silicon substrate. Nevertheless, it was possible to prove that the nanowires were polycrystalline. Finally the investigation of micro-cracks in a partially recrystallized nickel based alloy was performed. Questions to be answered were, amongst others, whether the endpoints of these cracks generally stop in recrystallized areas and whether cracking or recrystallization started first. But to solve problems like these, OIM maps of just one single cross section were not sufficient and a 3D representation of the material was necessary. Therefore, a serial sectioning method for large specimen areas had to be developed. A thin layer of the specimen surface was removed by grinding and polishing. The thickness of this layer was determined by the

measurement of Vickers indentations in the surface before and after sectioning. It emerged that the abrasion values for identically performed steps varied substantially. Also the abrasion values across the surface varied. Error calculations proved that the measurement of the thickness of the removed layers was quite exact with an error of around 0.6 μm. The results seem to prove that the recrystallized grains have a stopping effect on the crack propagation and the recrystallization occurred before the cracking. Some of the scans indicated an irregular recrystallization process, in contrast to the models for recrystallization of Ni-based alloys presented in literature. But additional investigations would be necessary to corroborate these results.

6 Literature

[1] Reimer L., 1998. Scanning Electron Microscopy - Physics of Image Formation and Microanalysis, Springer Verlag, Berlin Heidelberg

[2] Manual - TSL OIM Data Collection

[3] Randle V., Engler O., 2000. Texture Analysis – Makrotexture, Microtexture & Orientation Mapping, Gordon and Breach Science Publishers

[4] Reimer L., Kohl H., 2008. Transmission Electron Microscopy – Physics of Immage Formation, Springer Verlag, Berlin Heidelberg

[5] Williams D. B., Carter C. B., 2009. Transmission Electron Microscopy, Springer Verlag, Berlin Heidelberg

[6] Joy D. C., 1994. Channeling in and channeling out: The origins of electron backscattering and electron channeling contrast, Proc EMSA, 592-593

[7] Wells O. C., 1999. Comparison of Different Models for the Generation of Electron Backscattering Patterns in the Scanning Electron Microscope, Scanning, Vol. 21, 368-371

[8] Sicherheitsdatenblatt OP-U Suspension

[9] Sharma H., van Bohemen S. M. C., Petrov R. H., Sietsma J., 2010. Three-dimensional analysis of microstructures in titanium, Acta Materialia, Vol. 58, 2399-2407

[10] Gottstein G., 2007. Physikalische Grundlagen der Materialkunde, Springer Verlag, Berlin Heidelberg

[11] Drouin D., Couture A. R., Gauvin R., Hovington P., Horny P., Demers H., 2002. Casino: monte CArlo SImultaion of electroN trajectory in sOlids, v2.42, Universite de Sherbrooke, Quebec

[12] Small J. A., Michael J. R., Bright D. S., 2002. Improving the quality of electron backscatter diffraction (EBSD) patterns from nanoparticles, Journal of Microscopy, Vol. 206, 170-178

[13] Granitzer P., Rumpf K., Pölt P., Krenn H., 2009. Porous silicon/metal nanocomposite with tailored magnetic properties, Physica Status Solidi (A) Applications and Materials, Vol. 206, Issue 6, 1264-1267

[14] Granitzer P., Rumpf K., Pölt P., Reichmann A., Hofmayer M., Krenn H., 2007. Magnetization of self-organized Ni-nanowires with peculiar magnetic anisotropy, Journal of Magnetism and Magnetic Materials, Vol. 316, Issue 2, 302-305

[15] Khorashadizadeh A., Raabe D., Winning M., Pippan R., 2011. Recrystallization and Grain Growth in Ultrafine-Grained Materials Produced by High Pressure Torsion, Advanced Engineering Materialsm Vol. 13, Issue 4, 245-250

[16] Steyskal E., 2010. Untersuchung freier Volumen in submikrokristallinem nickel mit der Methode der Dilatometrie, Masterarbeit, TU Graz

[17] Sommitsch C., Pölt P., Rüf G., Mitsche S., 2006. On the modelling of the interaction of materials softening and ductile damage during hot working of Alloy 80A, Journal of Materials Processing Technology, 177, 282-286

[18] Sakai T., Jonas J. J., 1984. Dynamic recrystallization: mechanical and microstructural considerations, Acta metall. Vol. 32, No. 2, 189-209

Appendix

Complete series of the inverse pole figure maps of the area surrounding crack C1:

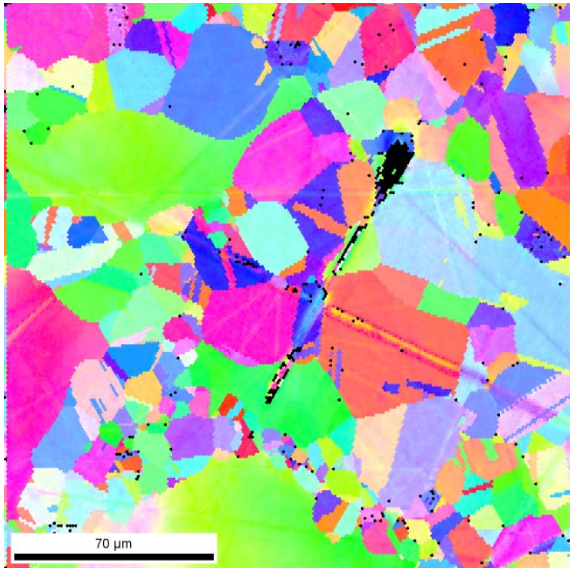

step 0

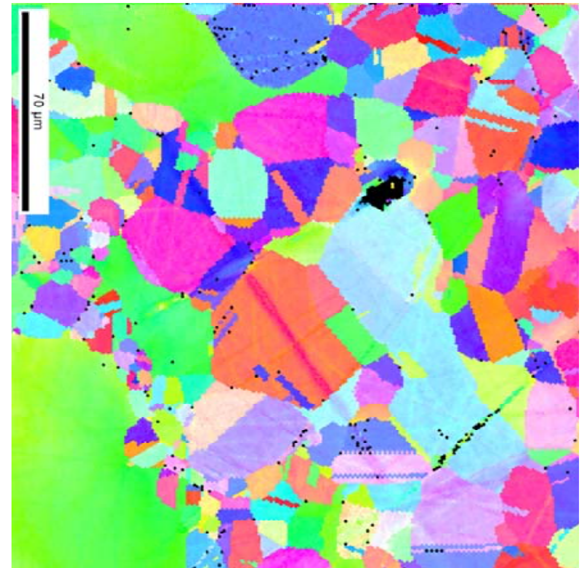

step 1: -3.0 µm

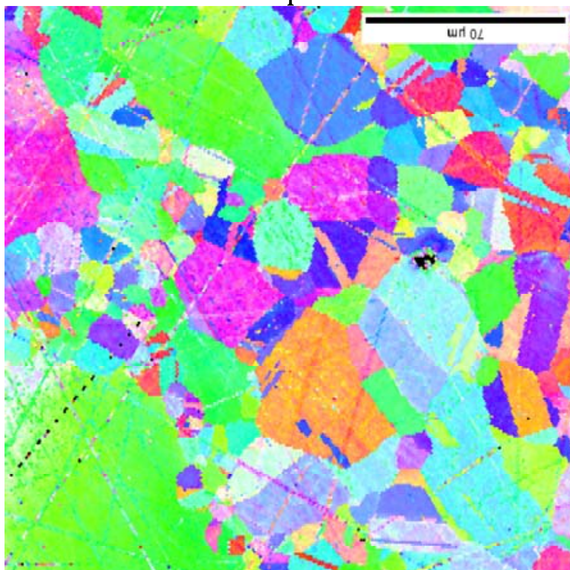

step 2: -1.3 µm

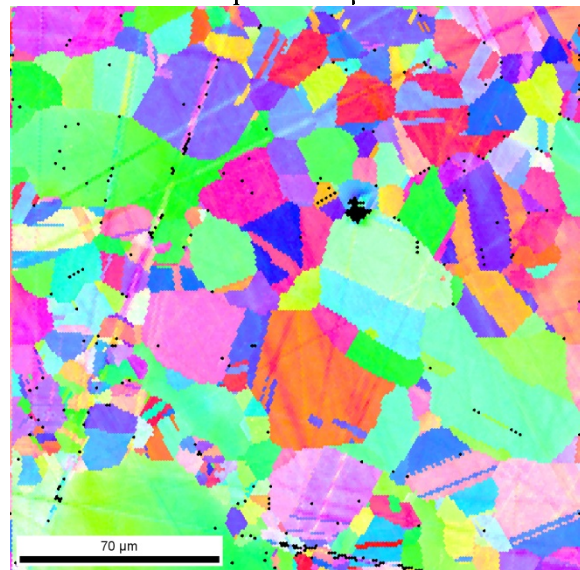

step 3: -1.7 µm

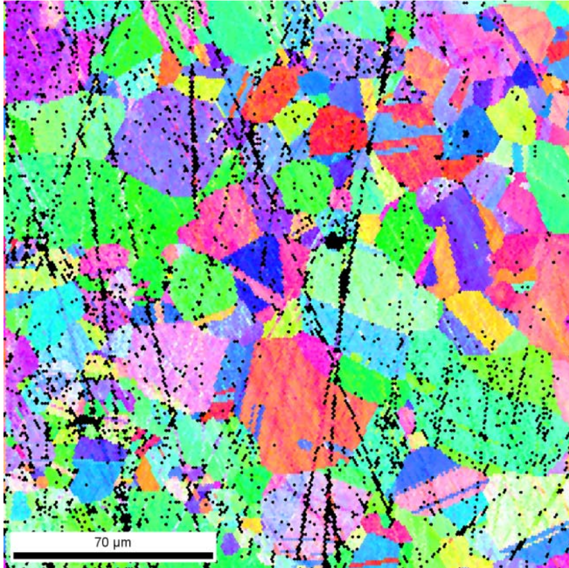

step 4: -0.4 µm

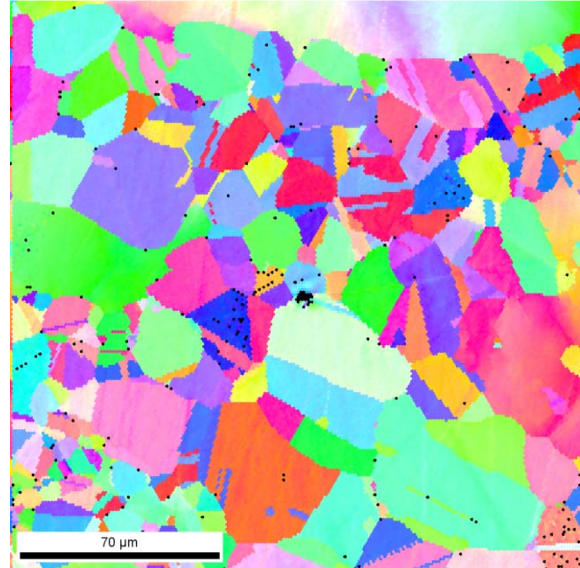

step 5: -1.4 µm

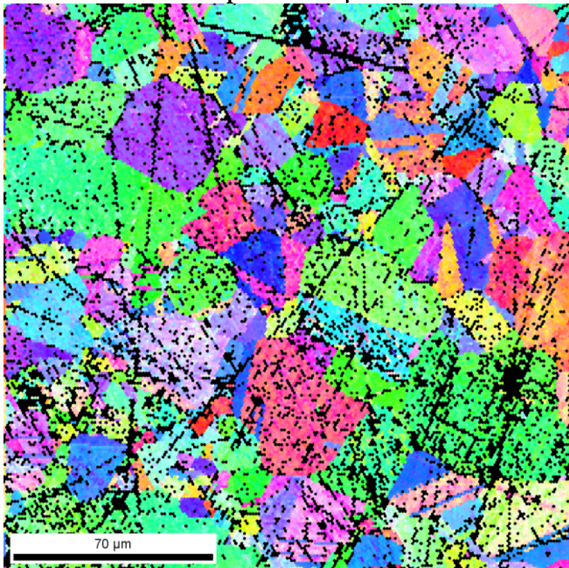

step 6: -0.4 µm

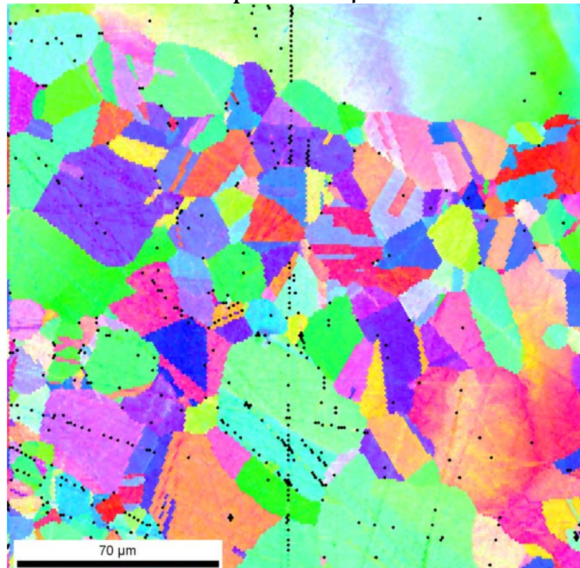

step 7: -0.3 µm

Complete series of the inverse pole figure maps of the area surrounding crack C2:

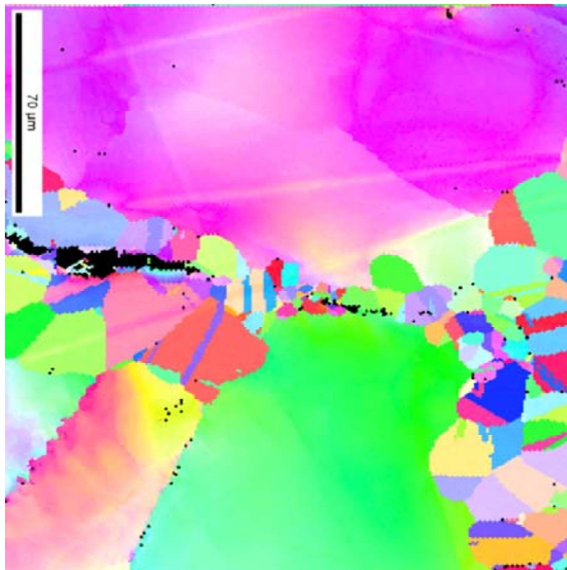

step 1

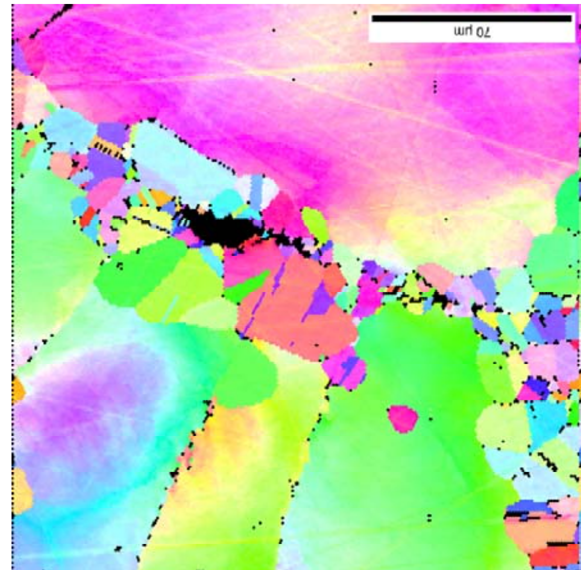

step 2: -5.3 µm

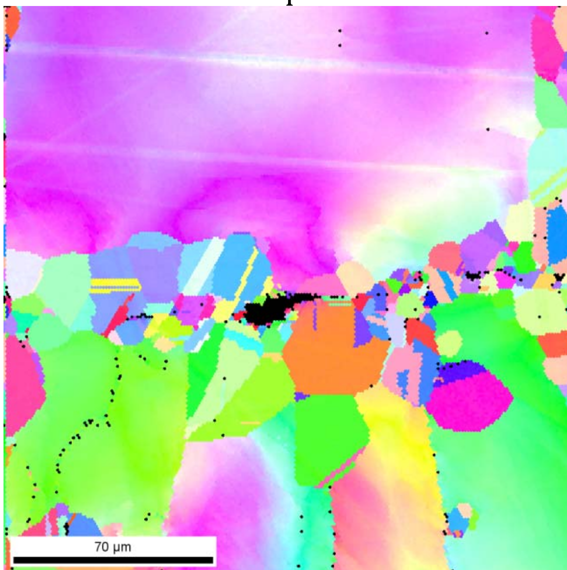

step 3: -4.5 µm

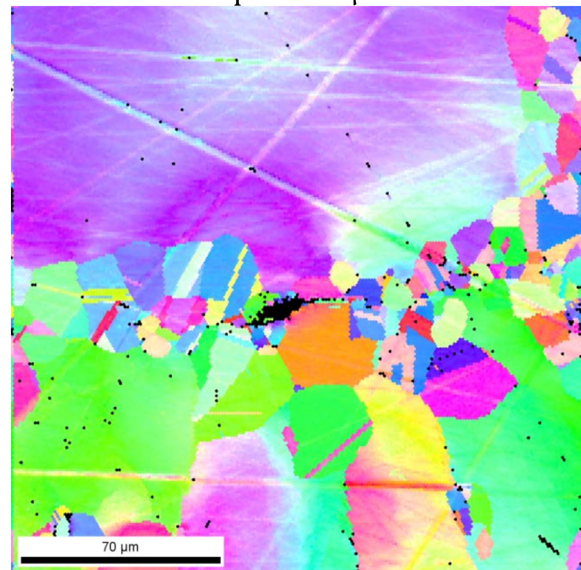

step 4: -1.7 µm

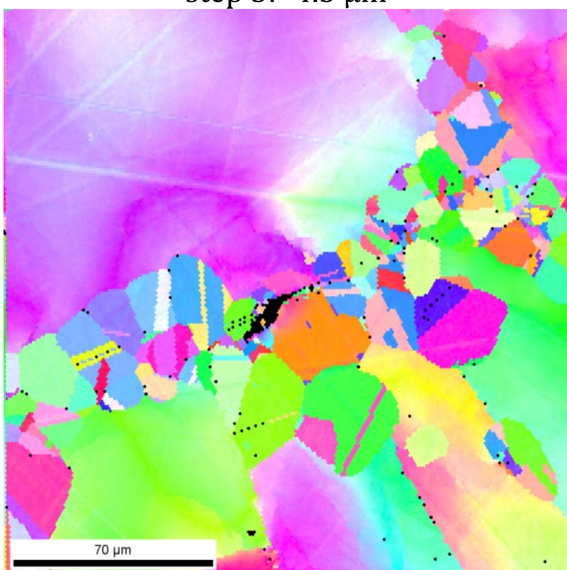

step 5: -2.0 µm

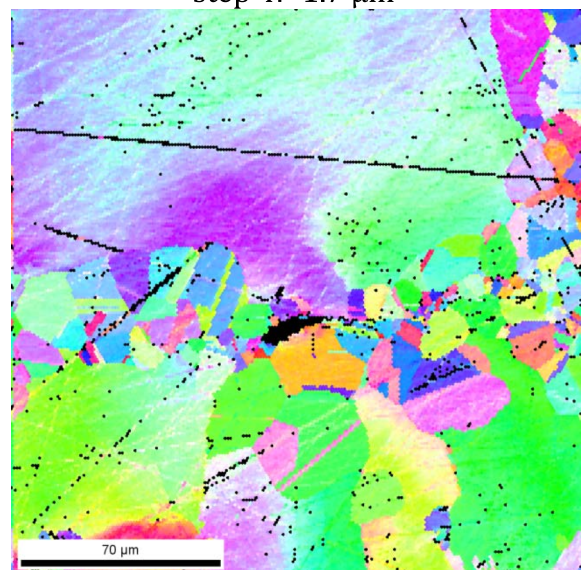

step 6: -1.8 µm

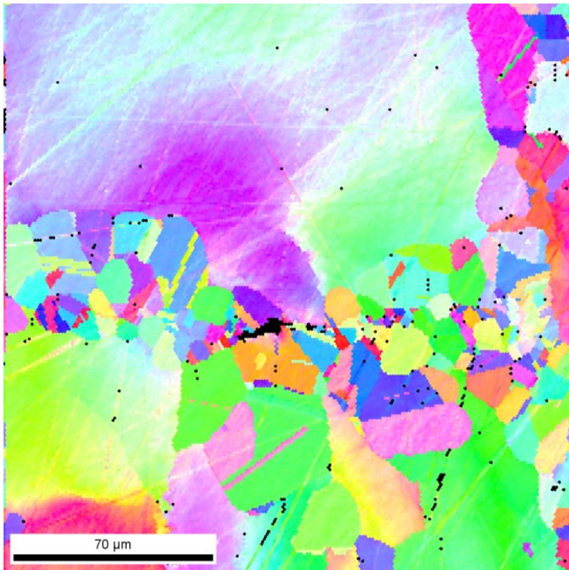

step 7: -1.5 µm

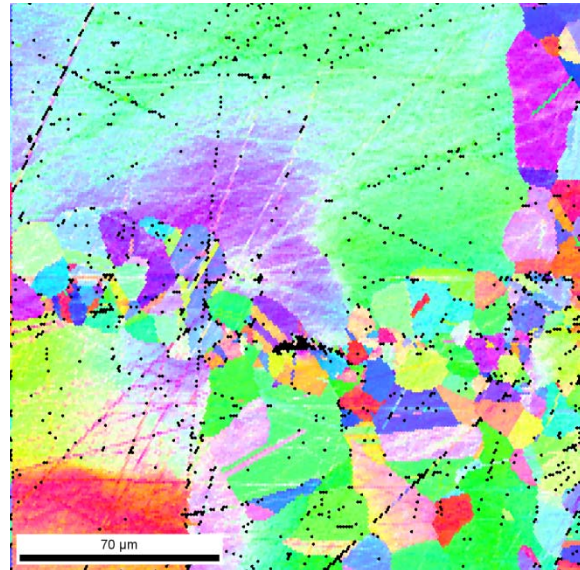

step 8: -1.7 µm

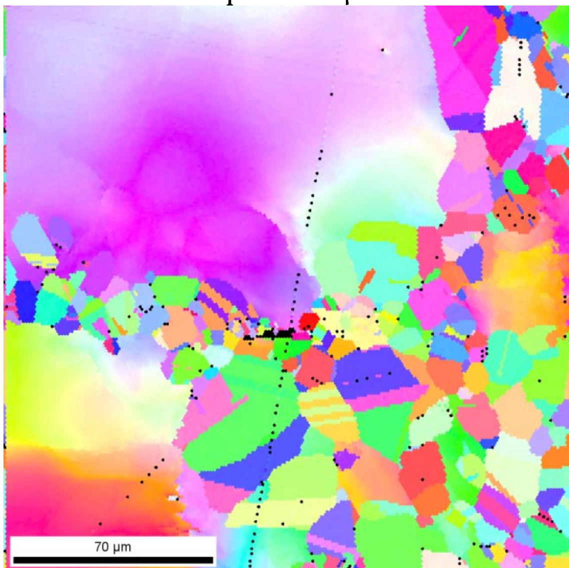

step 9: -3.7 µm

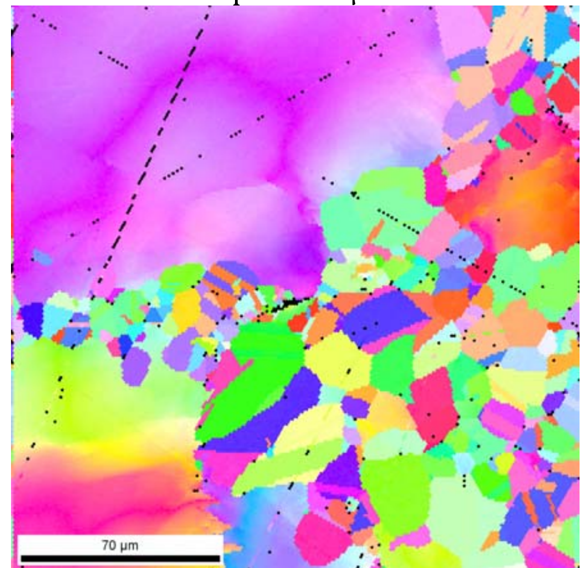

step 10: -1.2 µm

Complete series of the inverse pole figure maps of the area surrounding crack C3:

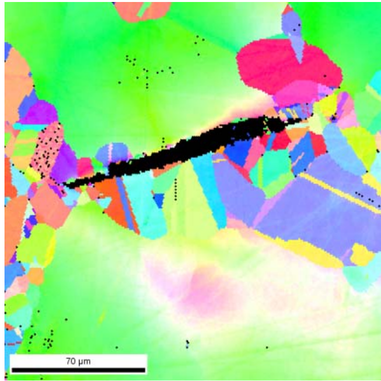

step 1

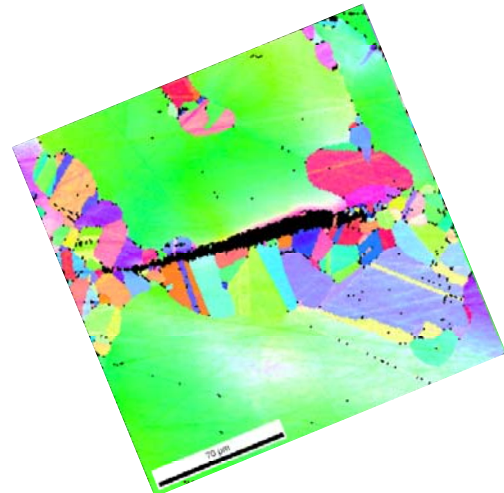

step 2: -1.3 µm

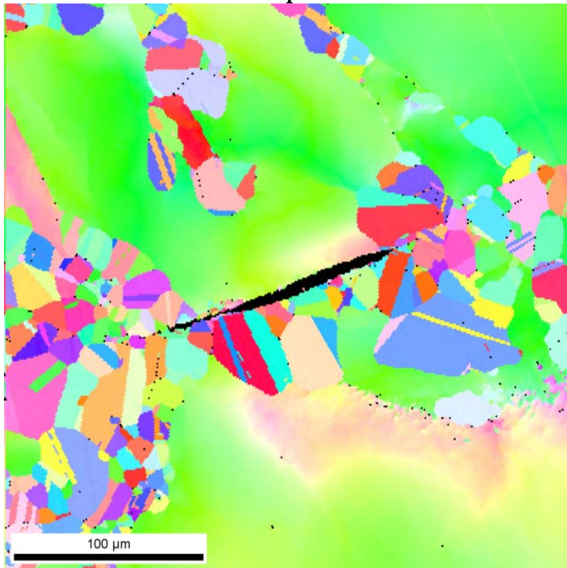

step 5: -3.3 µm

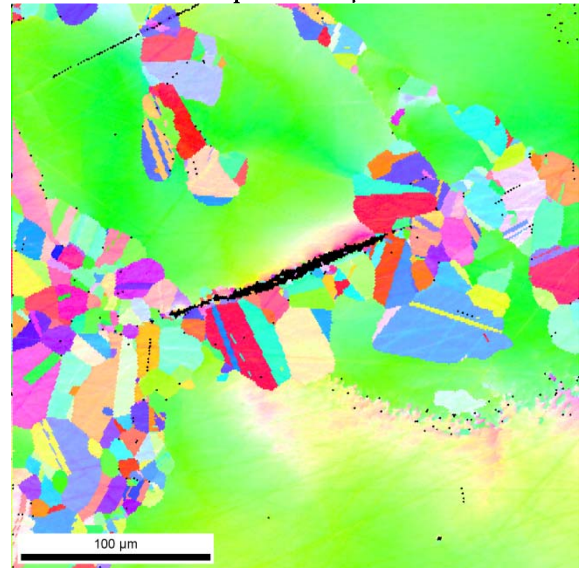

step 6: -0.2 µm

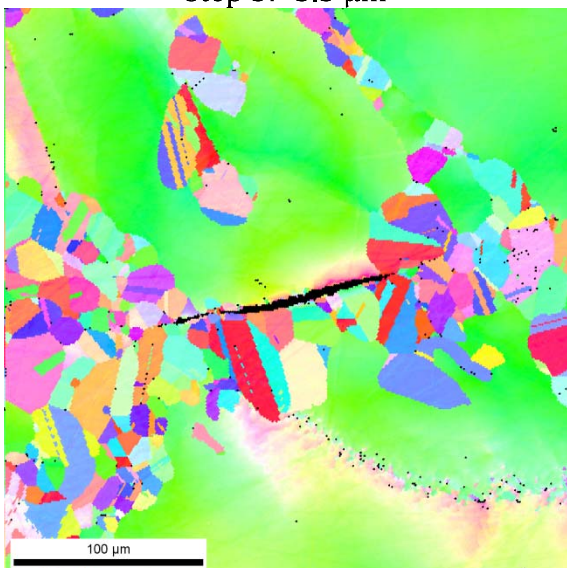

step 7: -2.6 µm

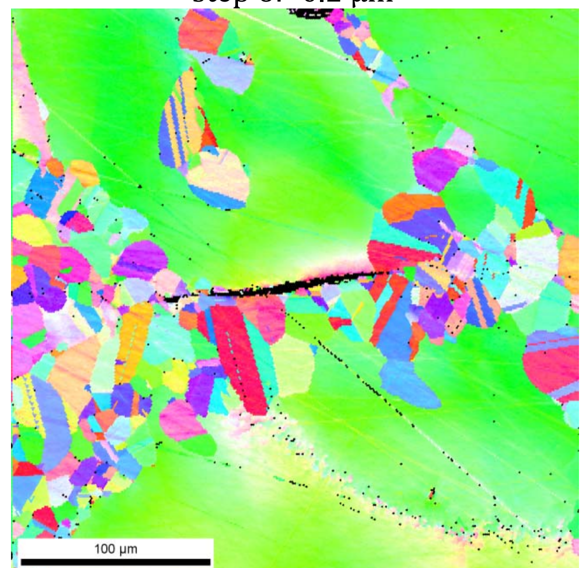

step 8: -2.0 µm

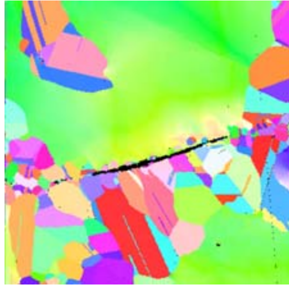

step 9: -4.4 µm

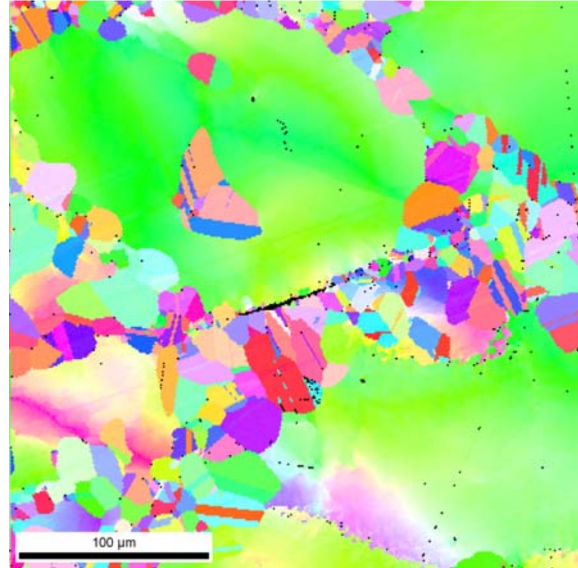

step 10: -2.3 µm

Complete series of the inverse pole figure maps of the area surrounding crack C4:

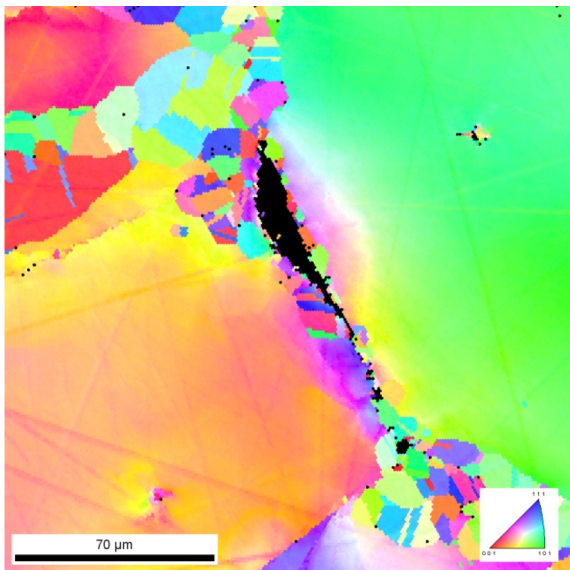

step 1

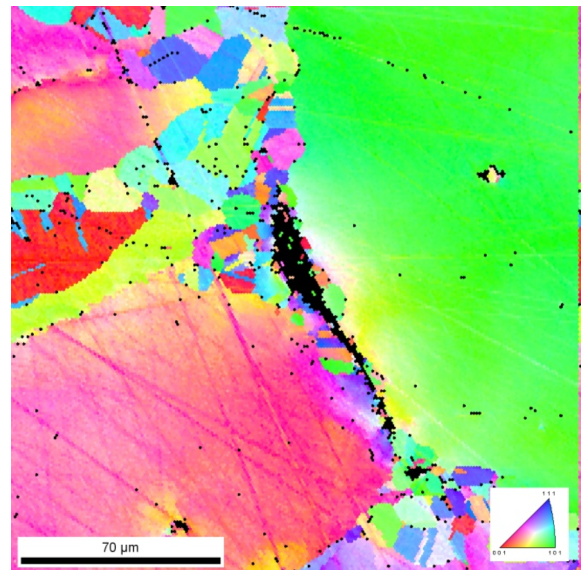

step 2: -2.9 µm

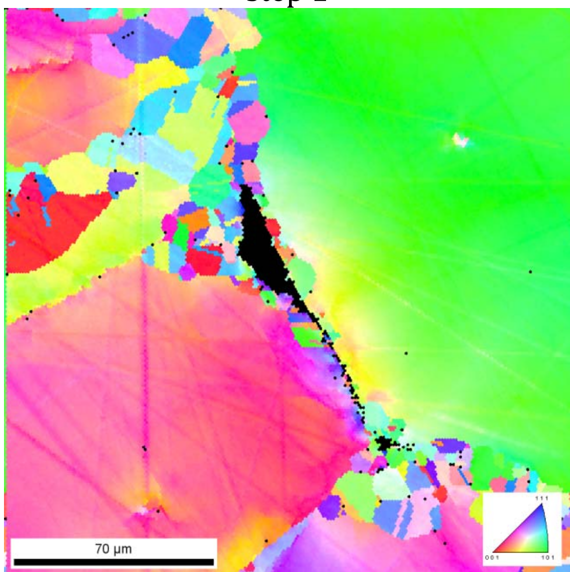

step 3: -2.8 µm

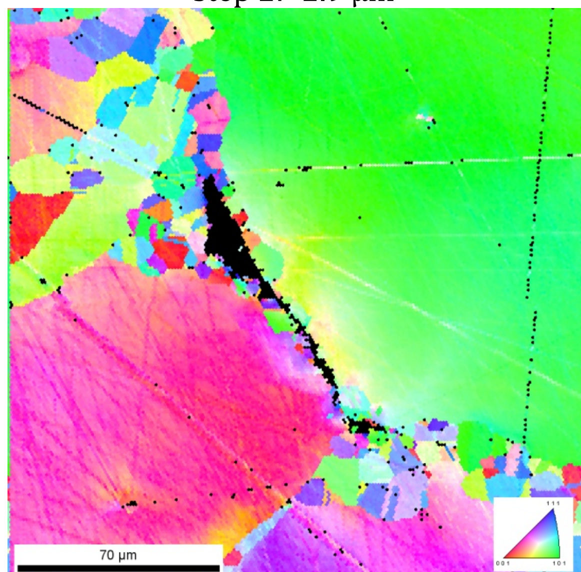

step 4: -1.2 µm

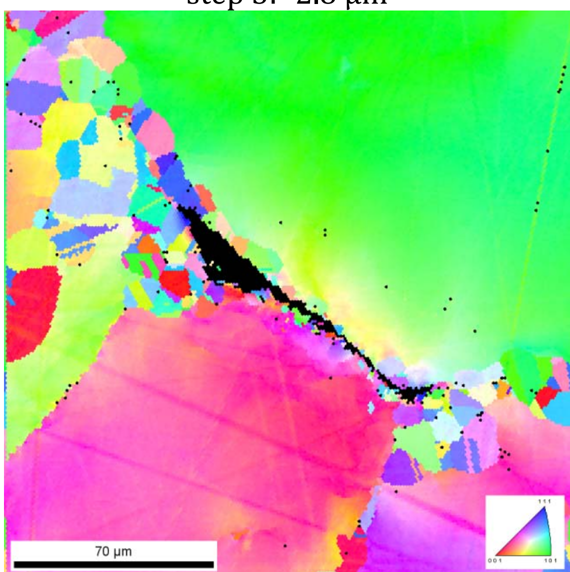

step 5: -1.9 µm

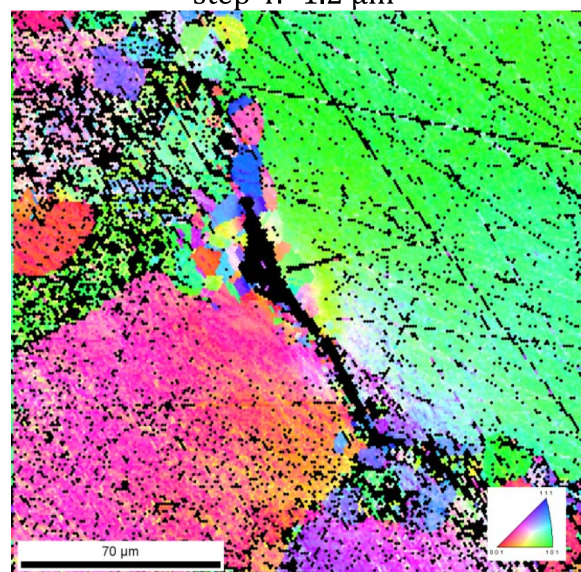

step 6: -1.0 µm

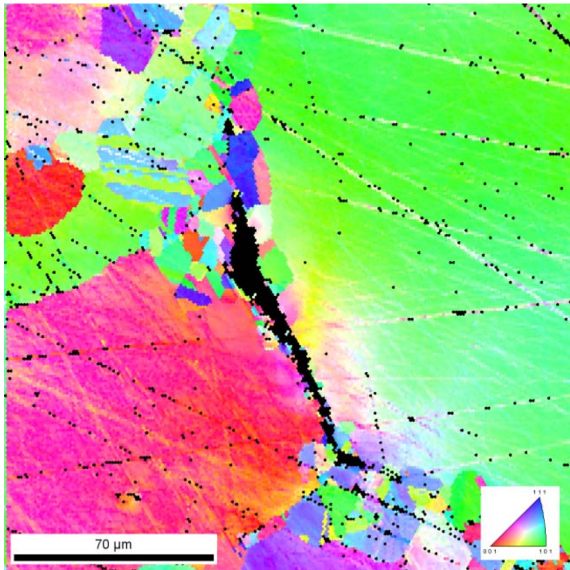

step 7: -0.5 µm

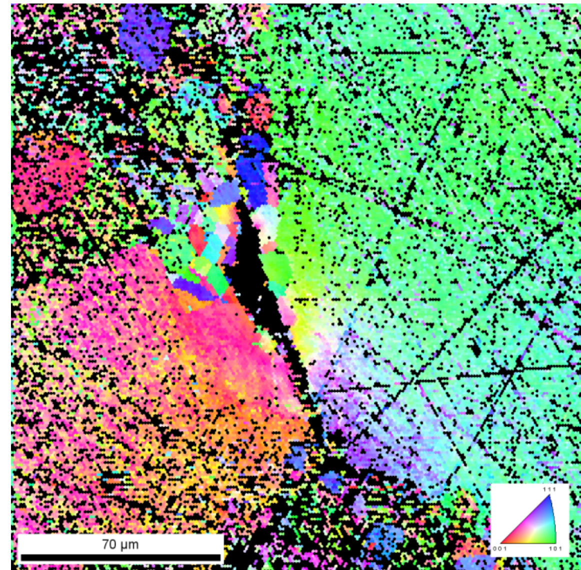

step 8: -0.6 µm

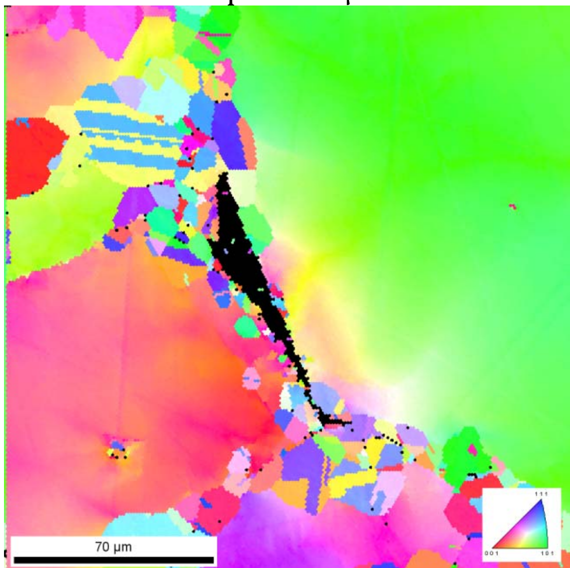

step 9: -2.6 µm

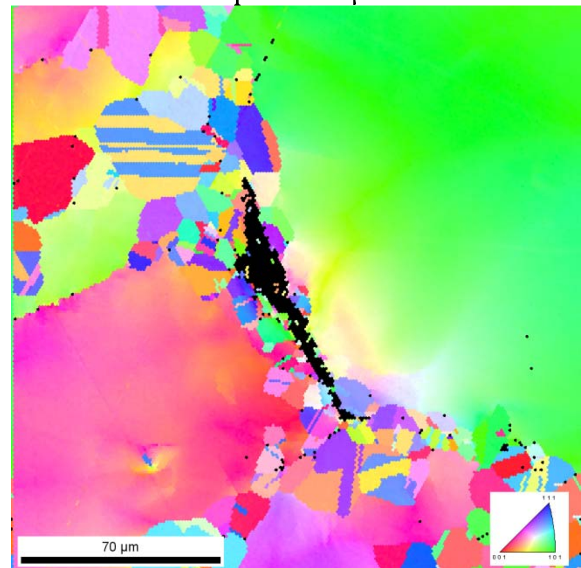

step 10: -1.0 µm

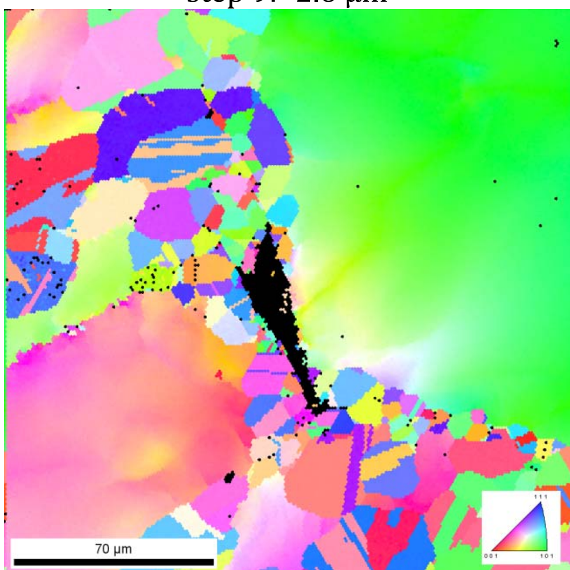

step 11: -5.3 µm

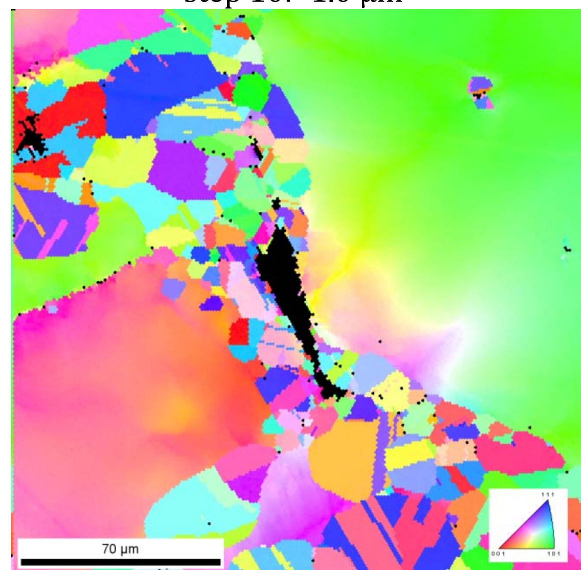

step 12: -3.5 µm

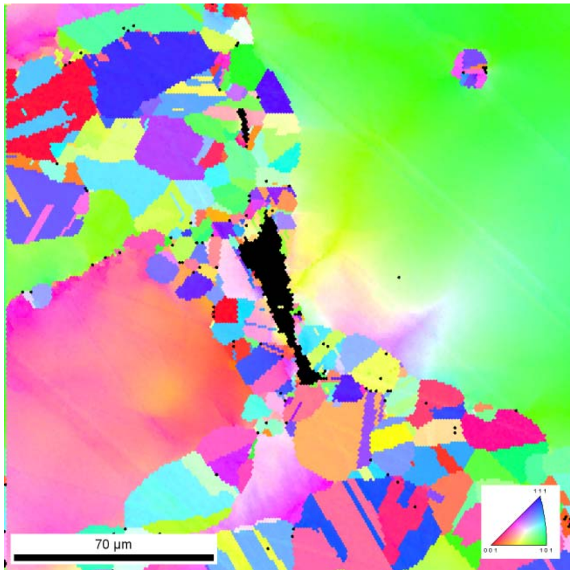

step 13: -1.2 µm

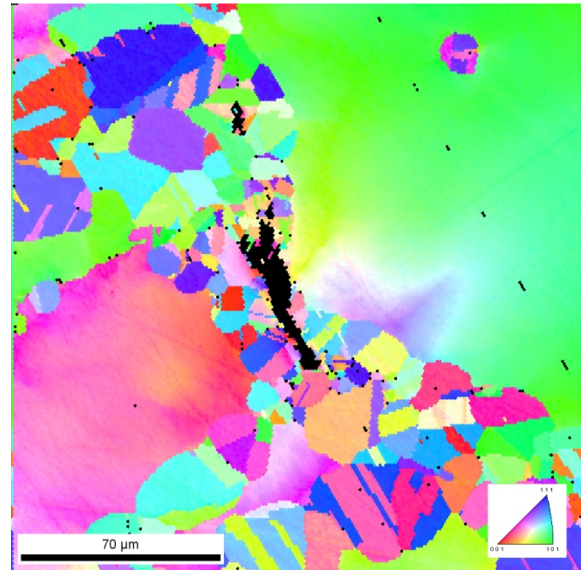

step 14: -0.8 µm

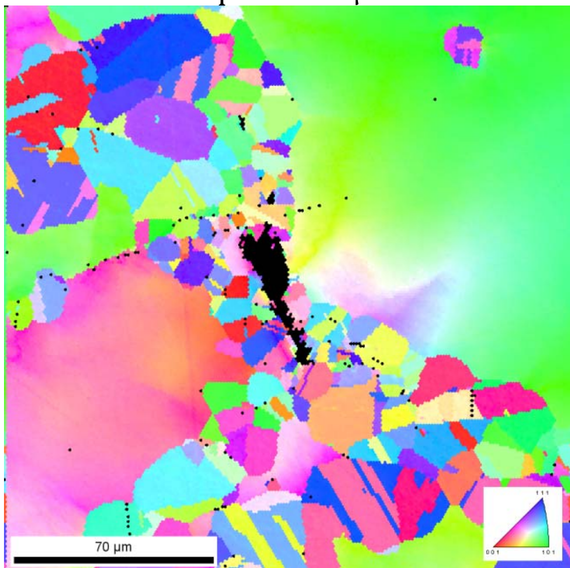

step 15: -0.7 µm

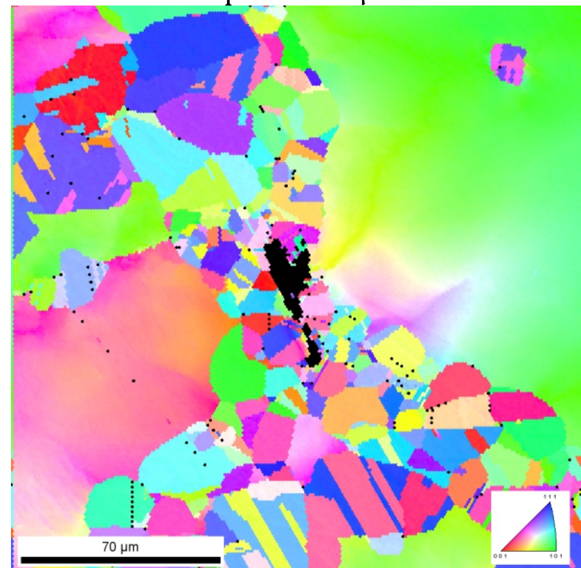

step 16: -2.3 µm

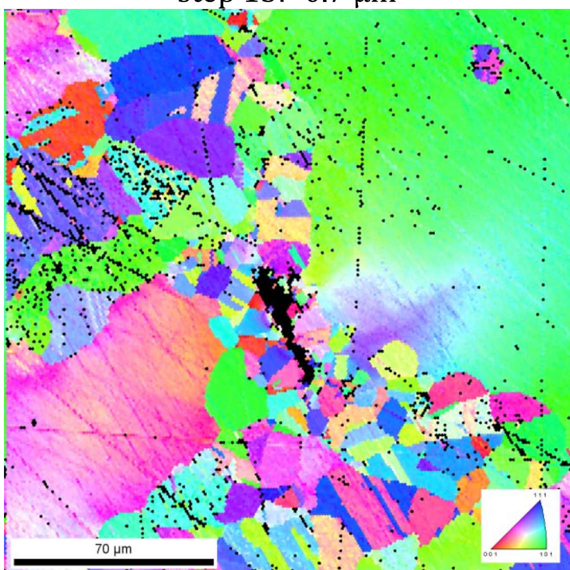

step 17: -0.9 µm

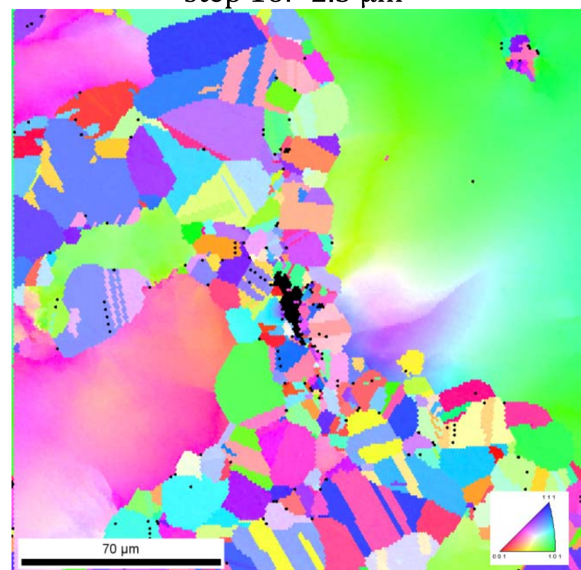

step 18: -1.5µm

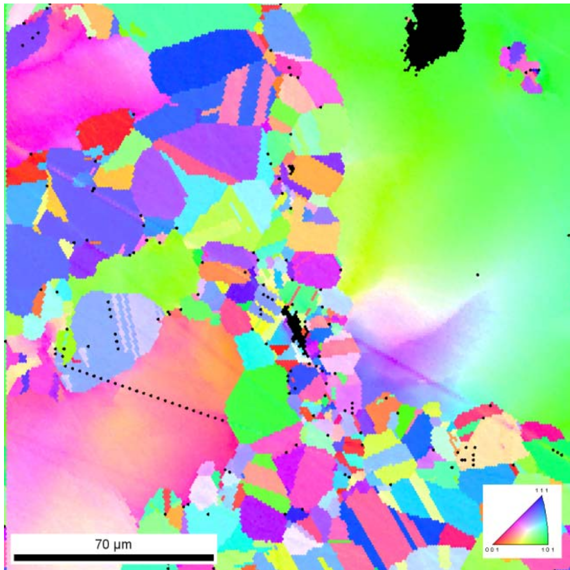

step 19: -2.2 µm

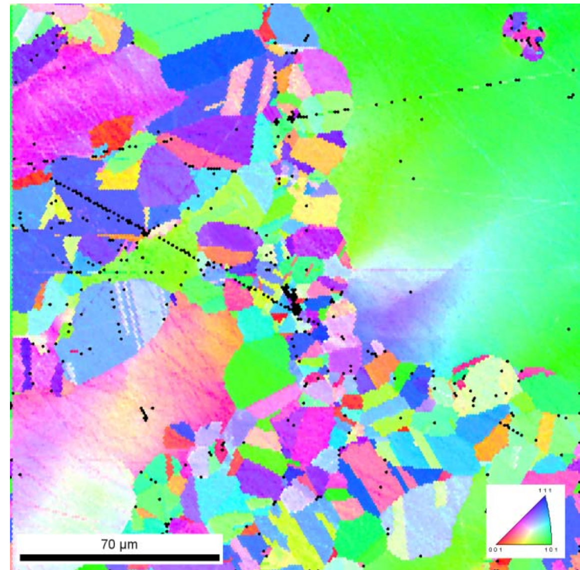

step 20: -0.7 µm:

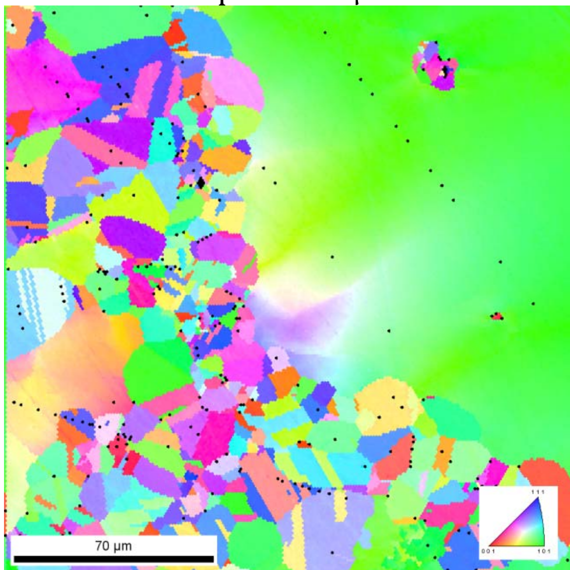

step 21: -1.7 µm

Complete series of the inverse pole figure maps of the area surrounding crack C5:

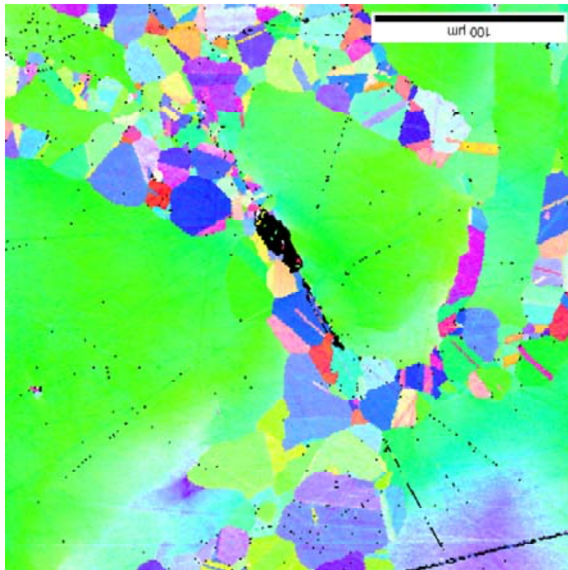

step 2

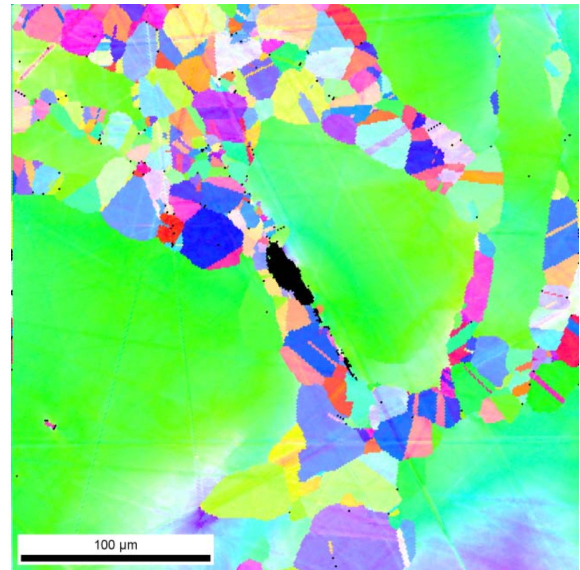

step 3: -1.5 µm

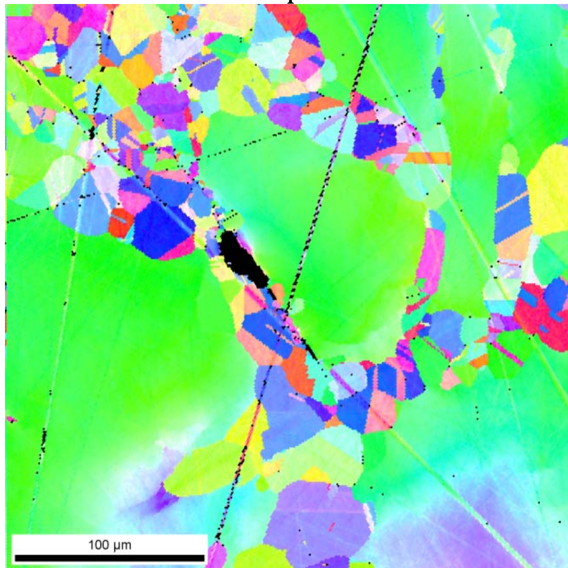

step 4: -0.5 µm

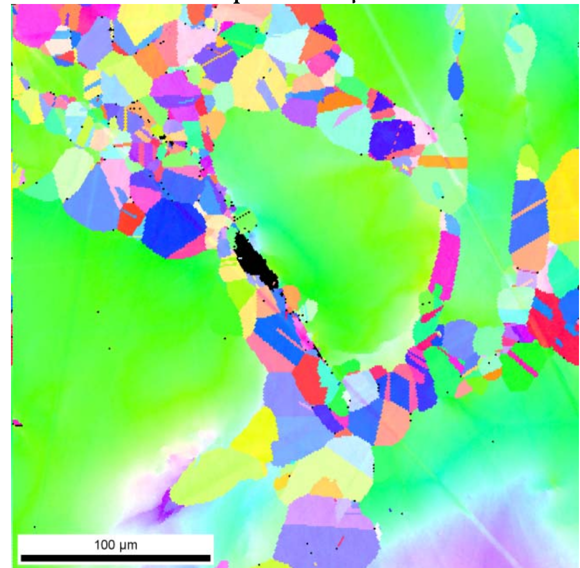

step 5: -1.3 µm

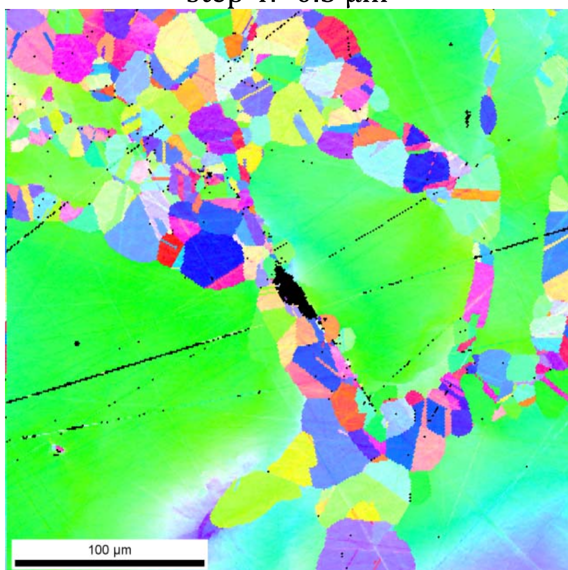

step 6: -0.2 µm

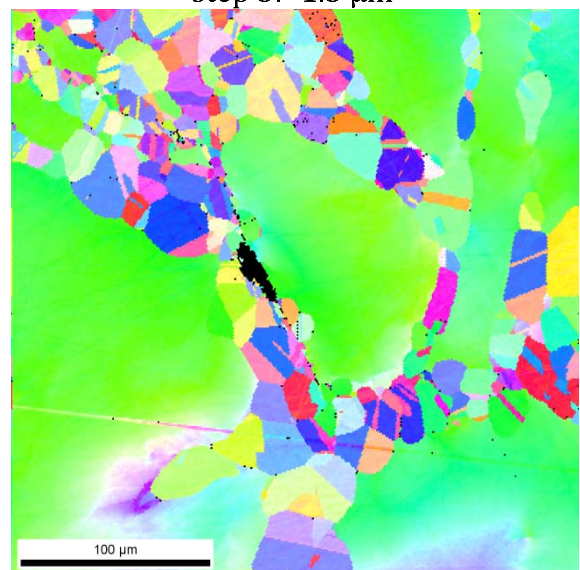

step 7: -0.8 µm

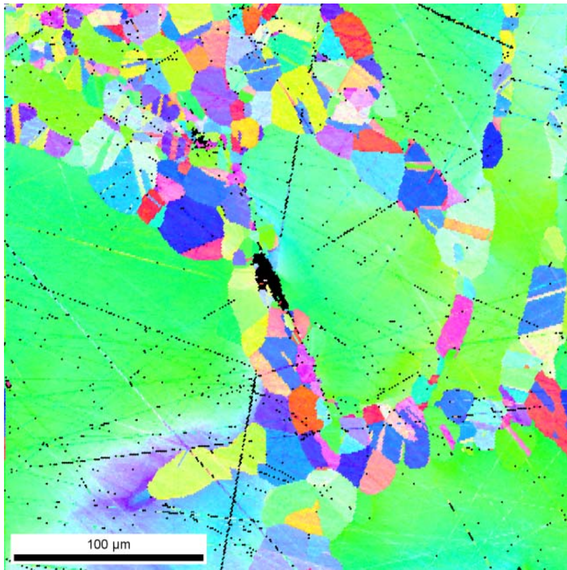

step 8: -0.8 µm

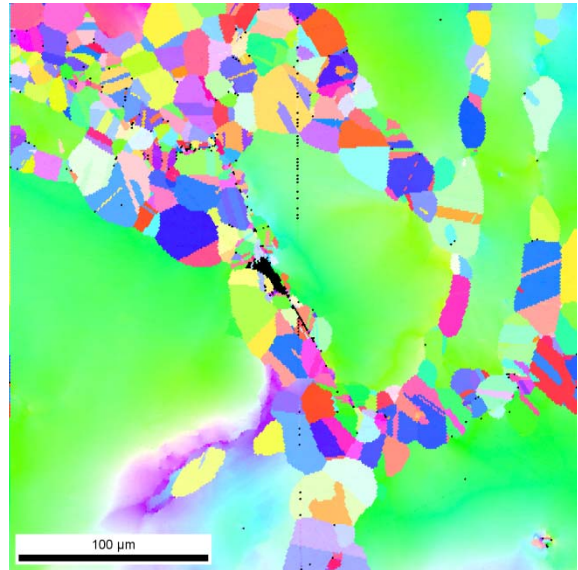

step 9: -1.9 µm

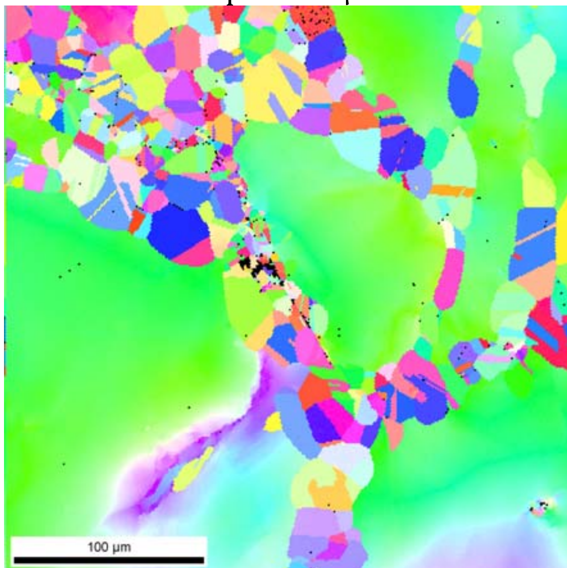

step 10: -1.6 µm

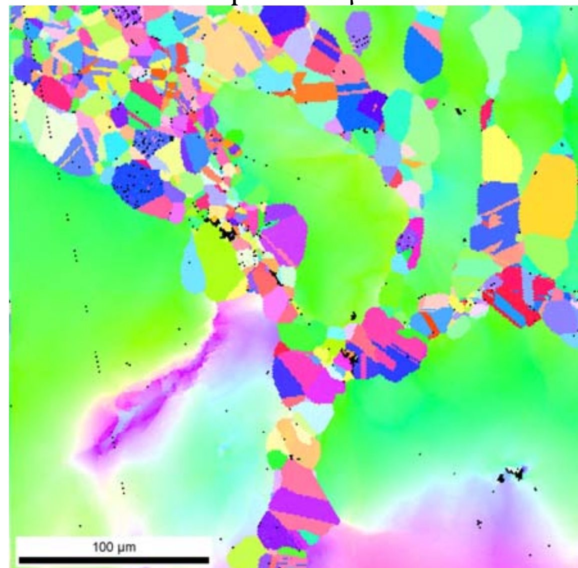

step 11: -3.5 µm

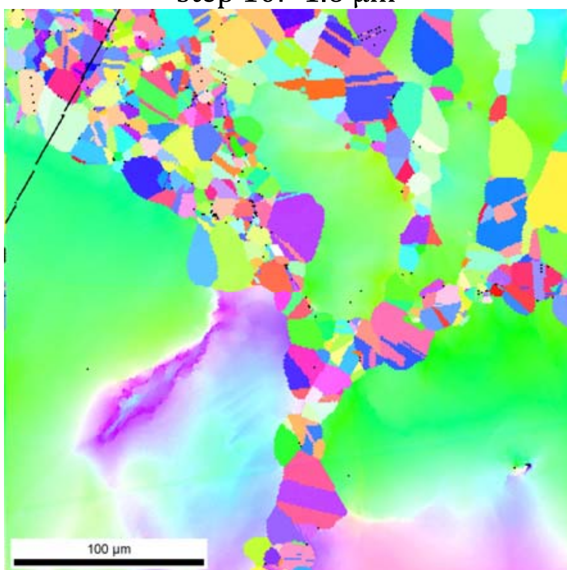

step 12 -3.8 µm

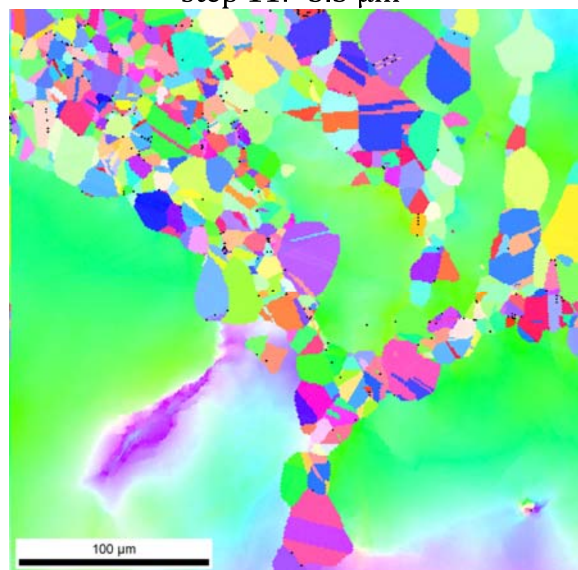

step 13: -1.4 µm

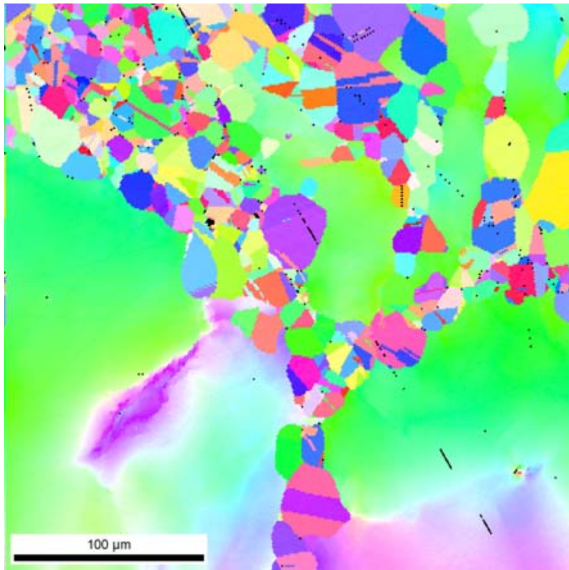

step 14 -0.3 µm

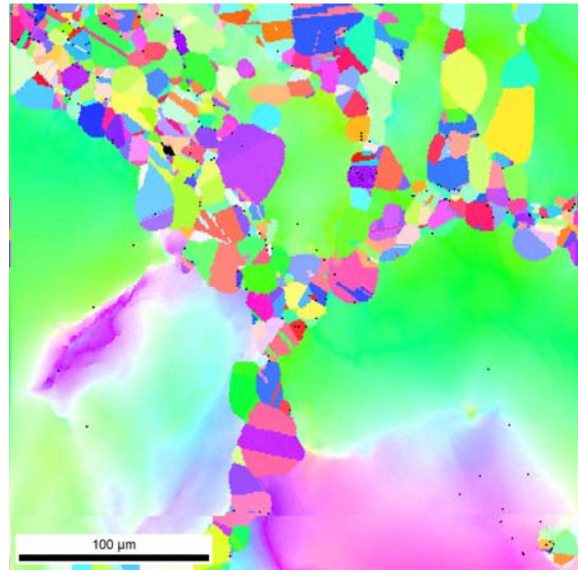

step 15: -1.3 µm

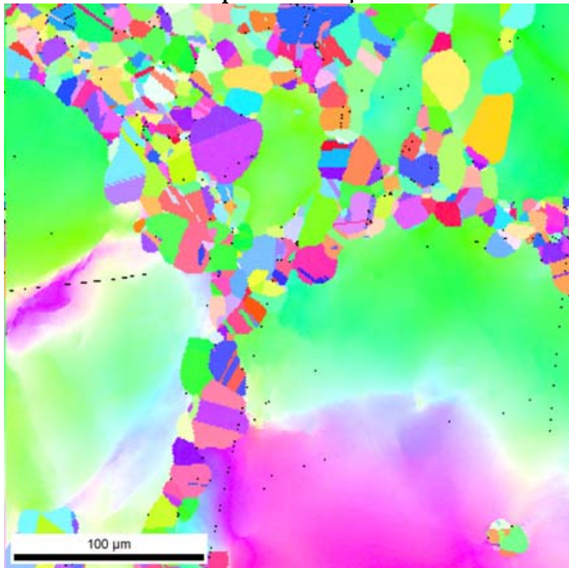

step 16: -2.7 µm

Complete series of the inverse pole figure maps of the area surrounding crack C6:

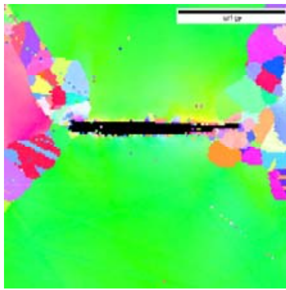

step 1

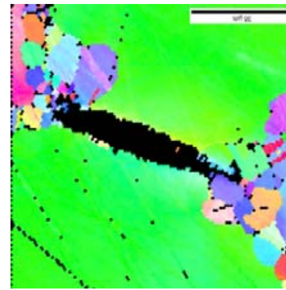

step 2: -4.6 µm

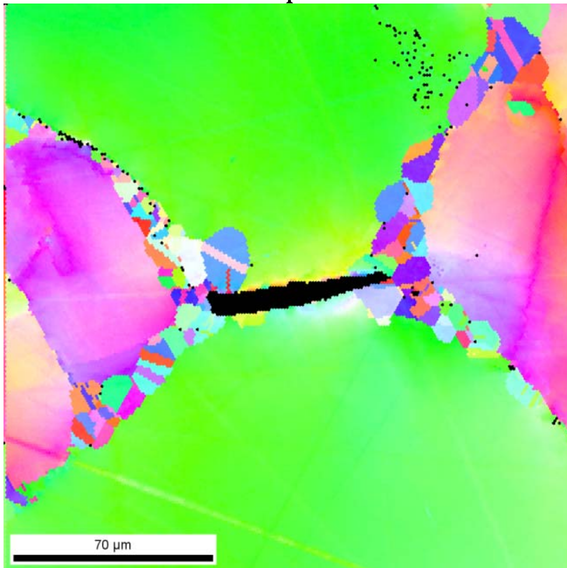

step 3: -3.8 µm

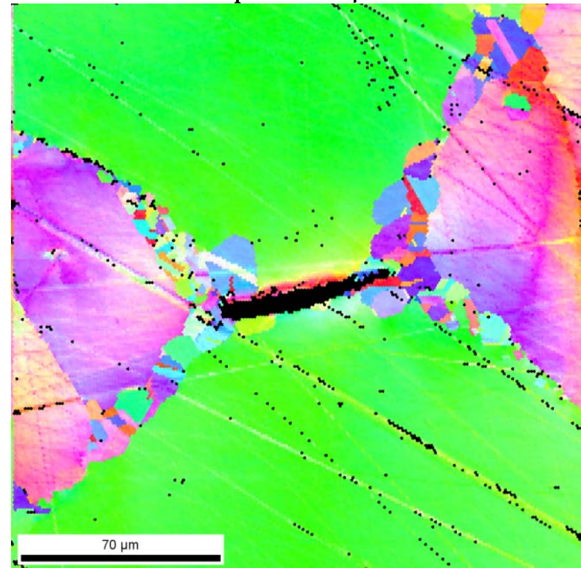

step 4: -1.7 µm

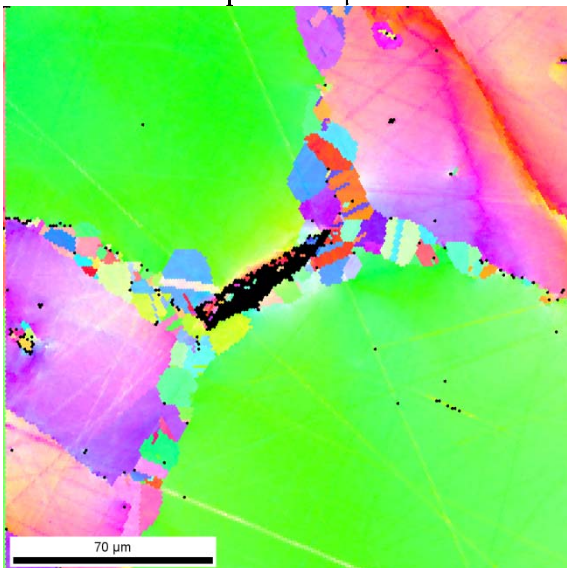

step 5: -2.1 µm

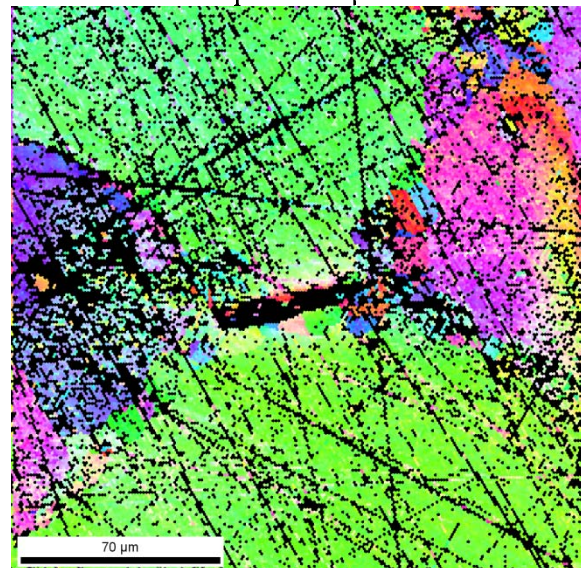

step 6: -1.6 µm

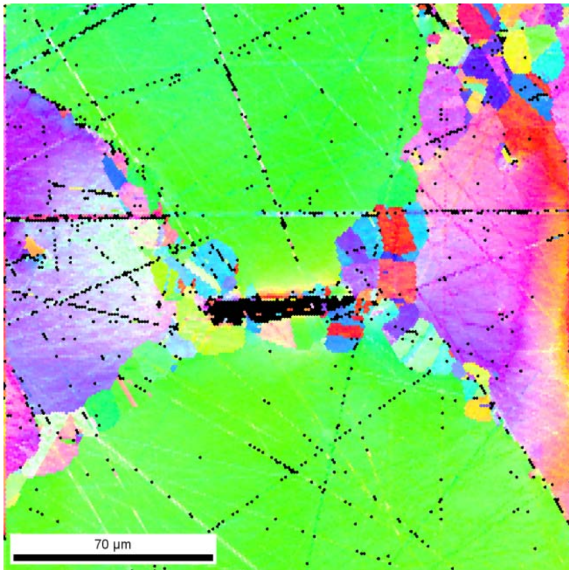

step 7: -0.6 µm

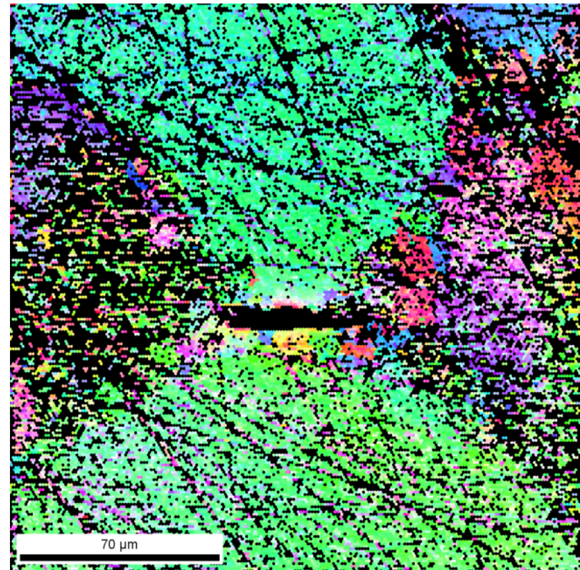

step 8: -1.1 µm

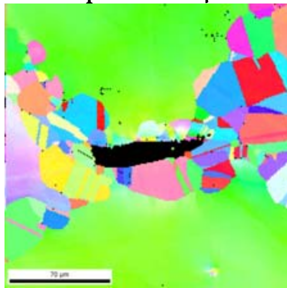
step 9: -2.9 µm

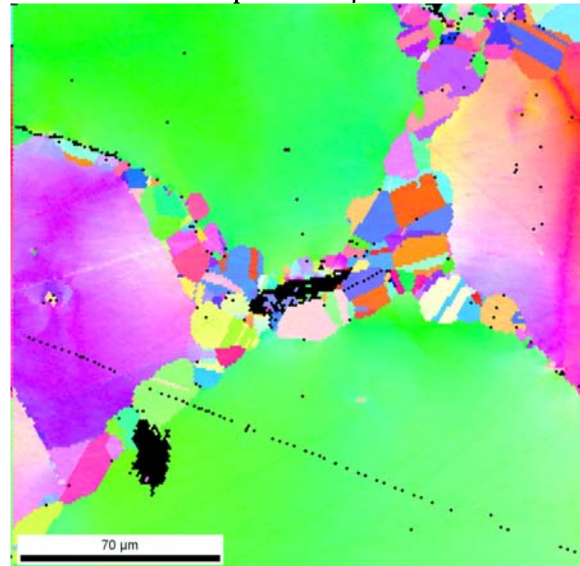

step 10: -0.9 µm

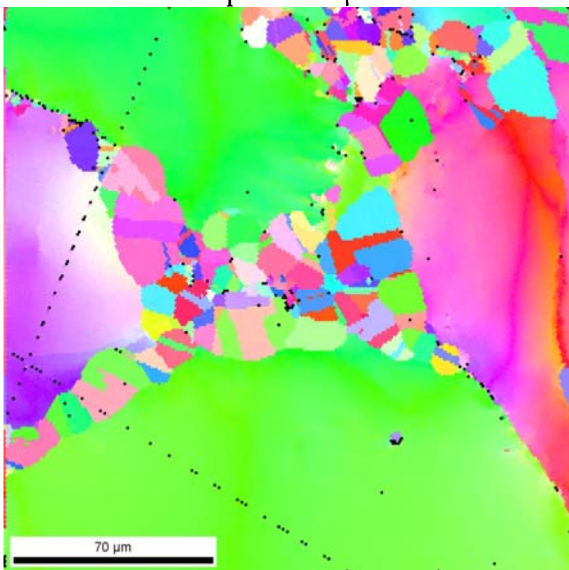

step 11: -7.1 µm

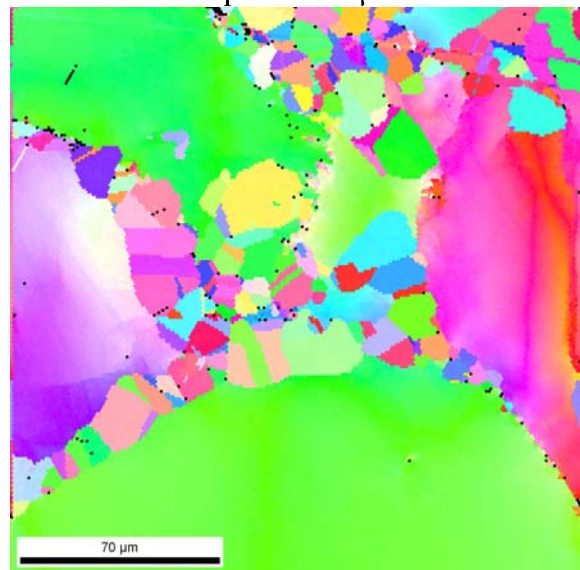

step 12: -3.9 µm

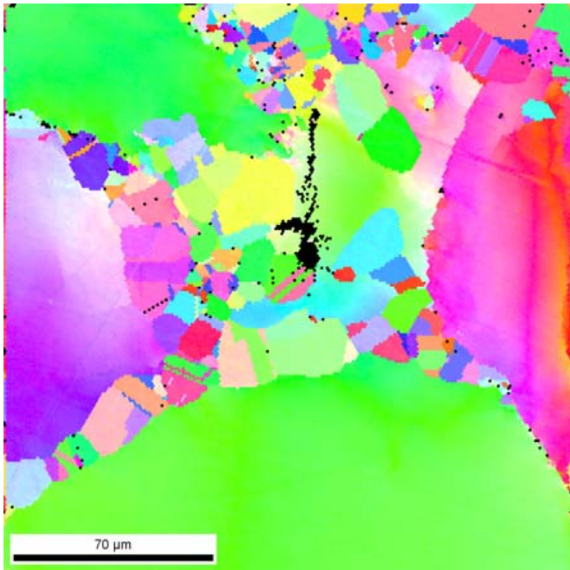

step 13: -1.9 µm

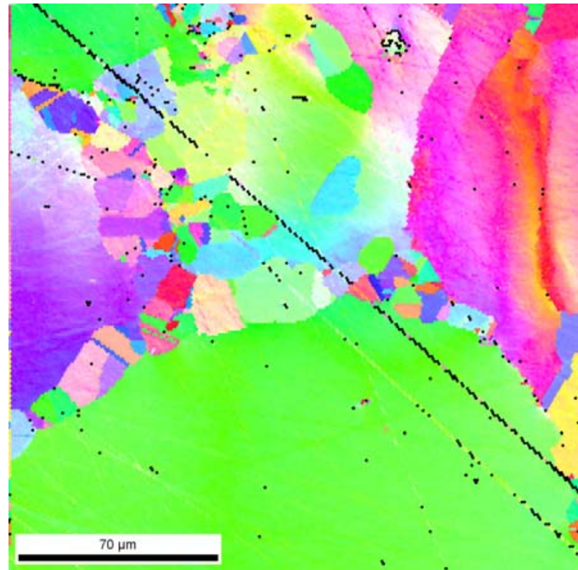

step 14: -1.1 µm

Complete series of the inverse pole figure maps of the area surrounding crack C7:

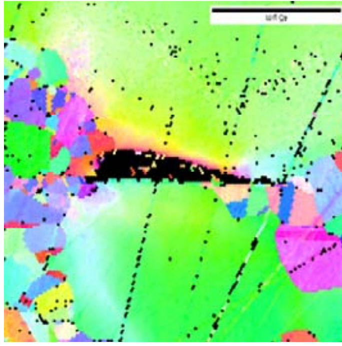

step 2

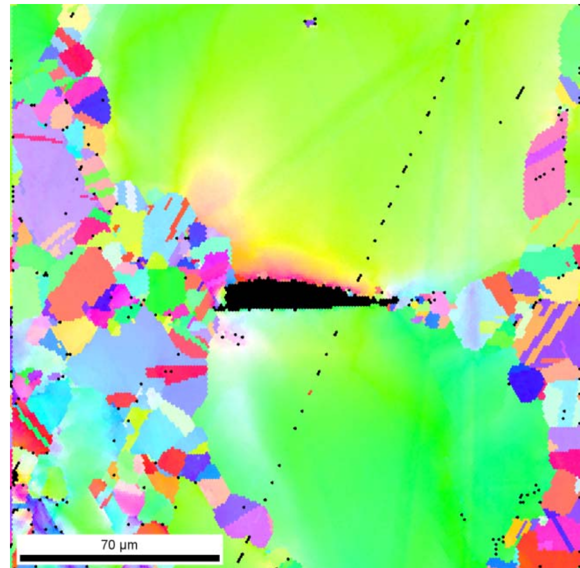

step 3: -4,5 µm

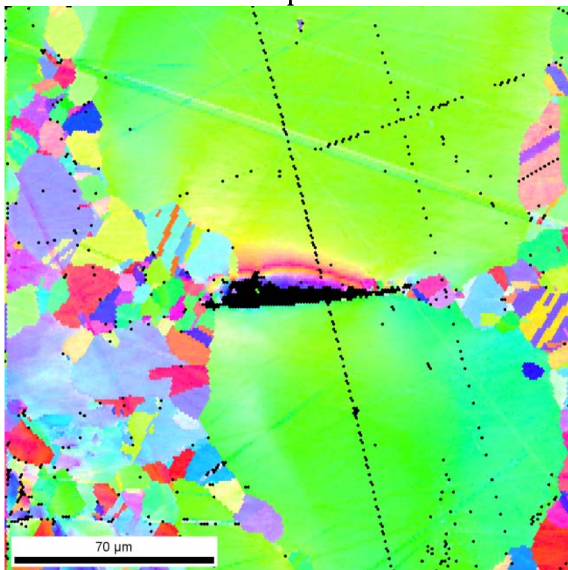

step 4: -2,0 µm

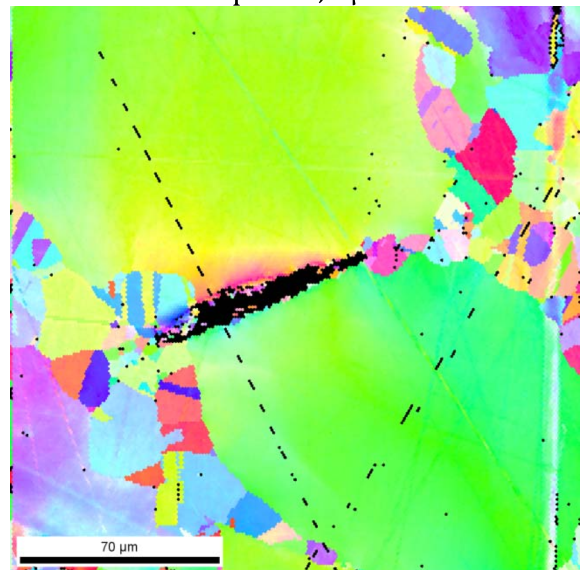

step 5: -2,3 µm

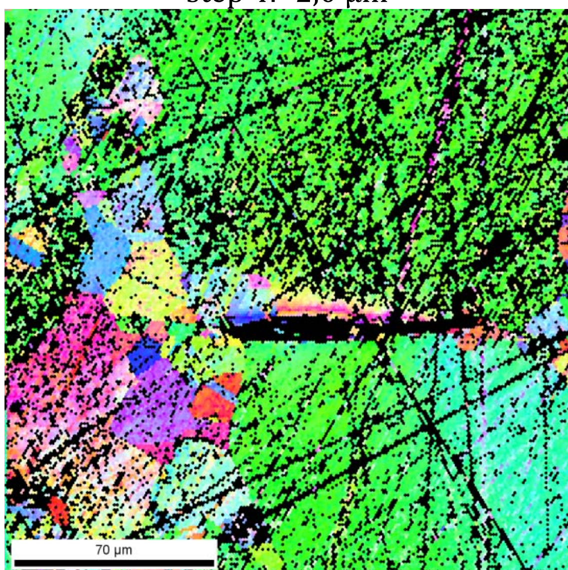

step 6: -1,9 µm

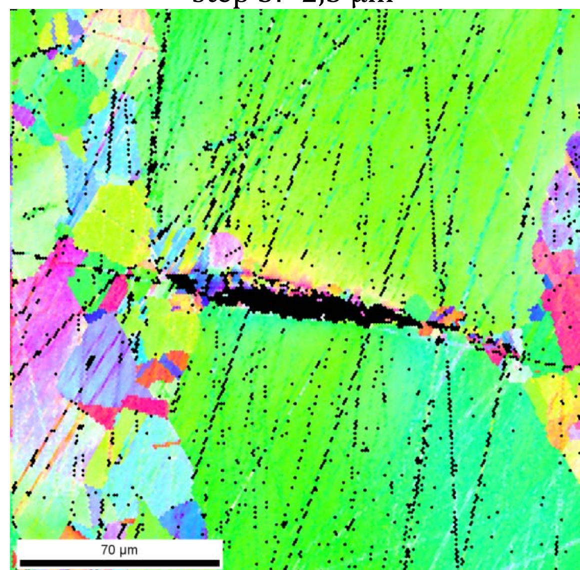

step 7: -0,8 µm

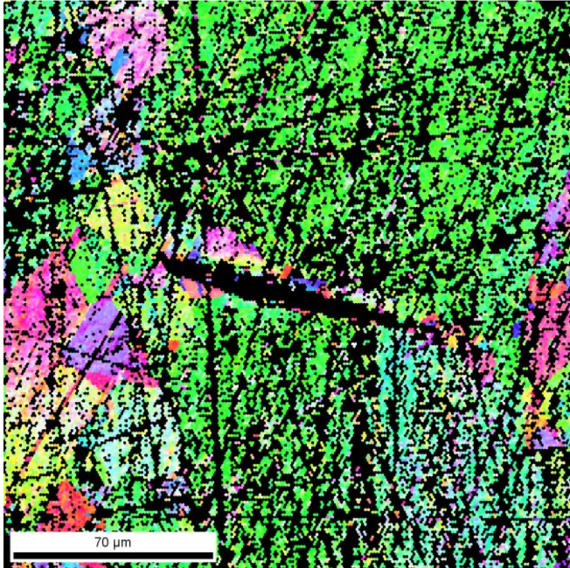

step 8: -2,0 µm

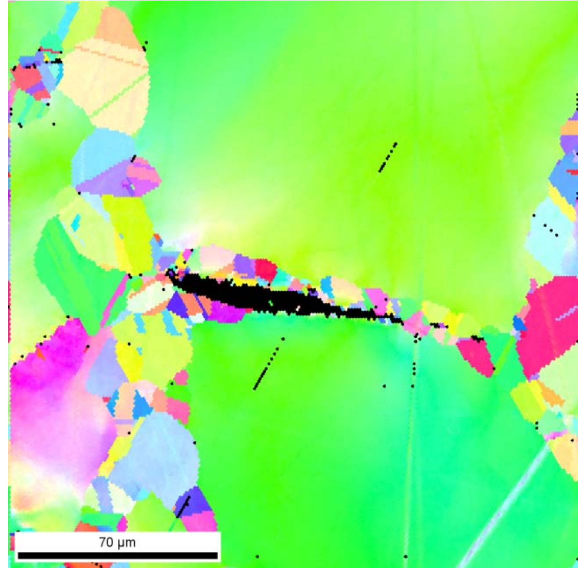

step 9: -3,3 µm

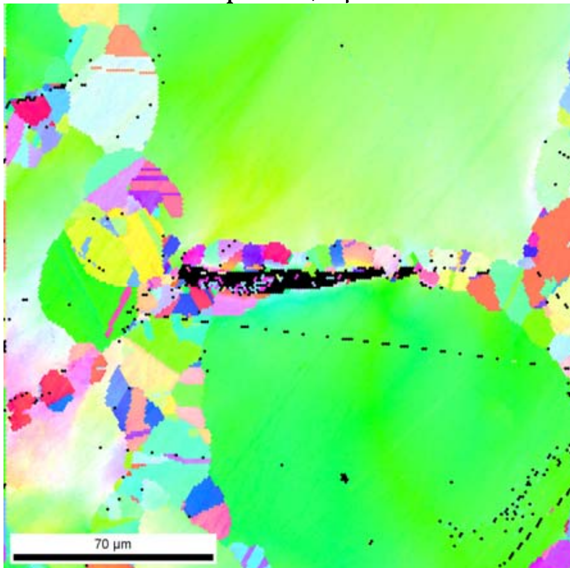

step 10: -1,6 µm

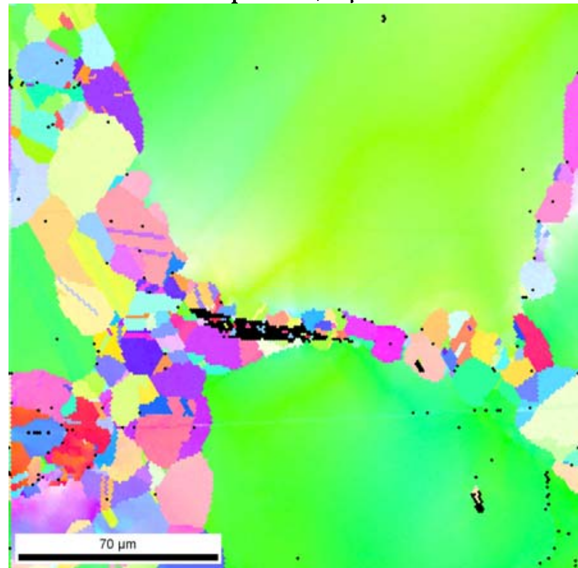

step 11: -8,2 µm

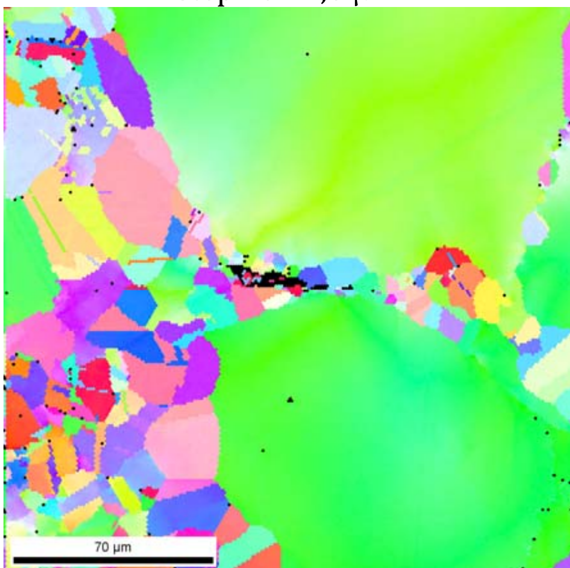

step 12 -4,2 µm

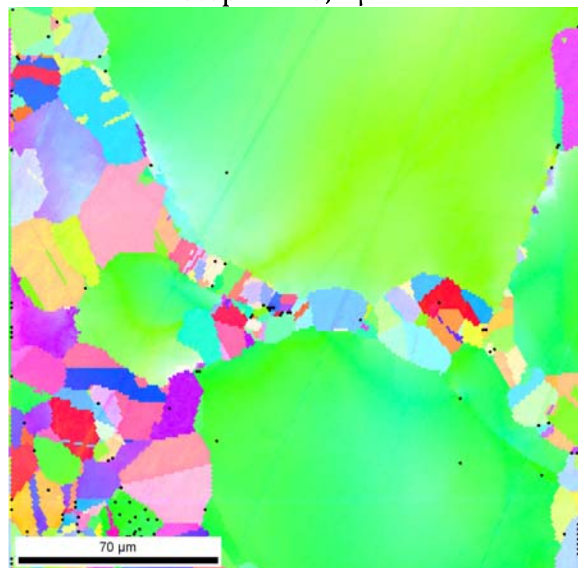

step 13: -2,9 µm

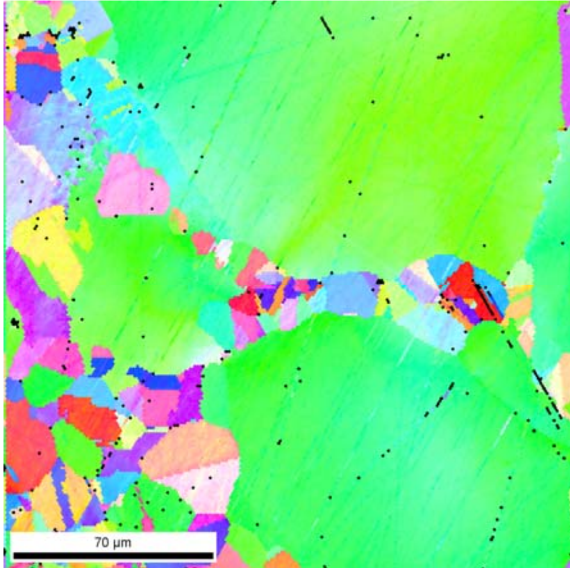

step 14 -1,5 µm

Complete series of the inverse pole figure maps of the area surrounding crack C8:

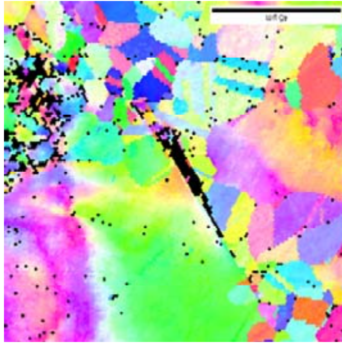

step 2

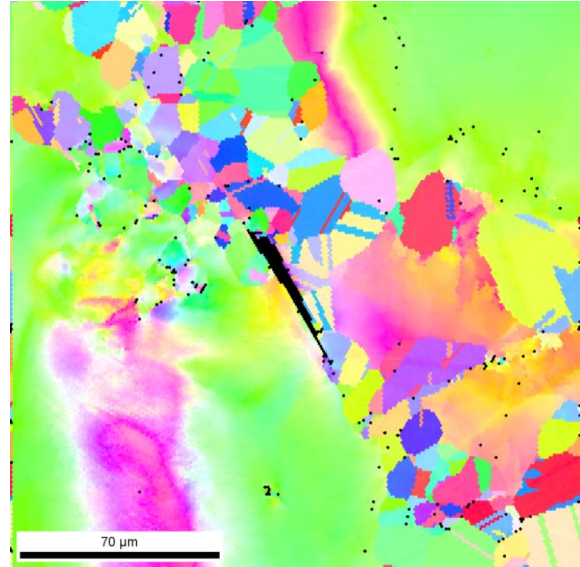

step 3: -4.7 µm

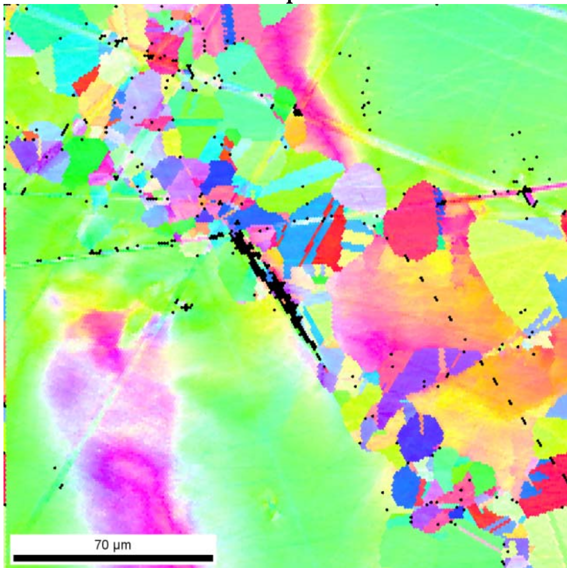

step 4: -1.7 µm

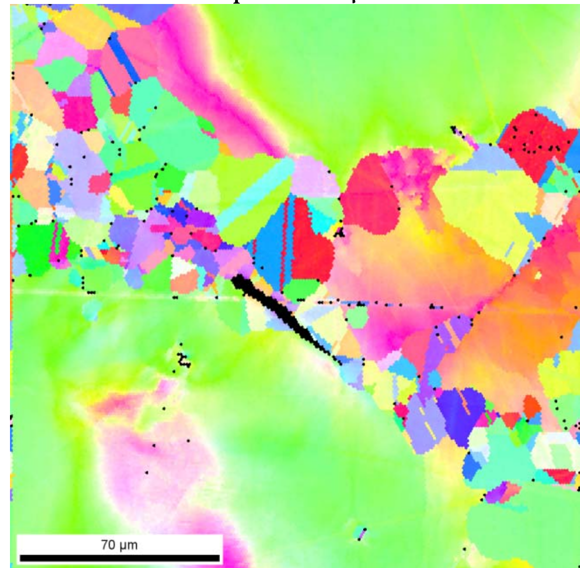

step 5: -2.3 µm

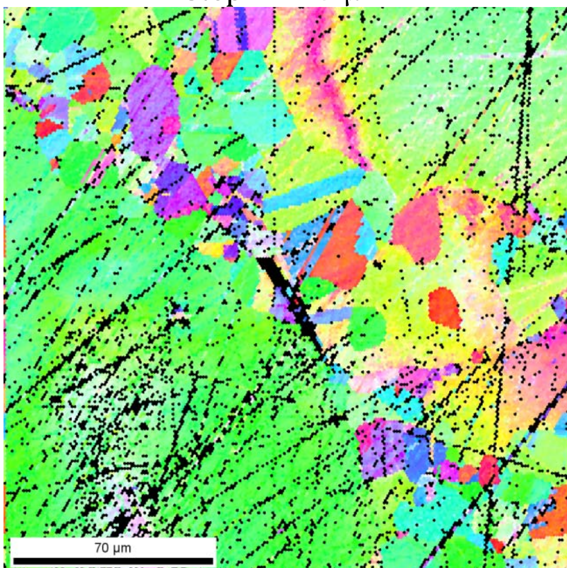

step 6: -2.2 µm

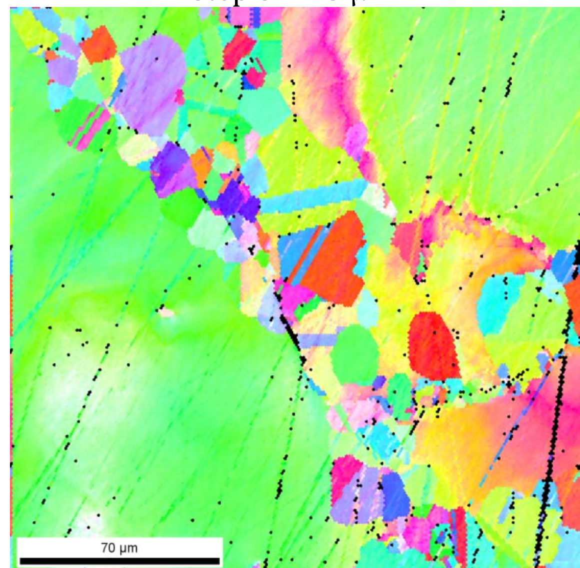

step 7: -2.0 µm

Complete series of the inverse pole figure maps of the area surrounding crack C9:

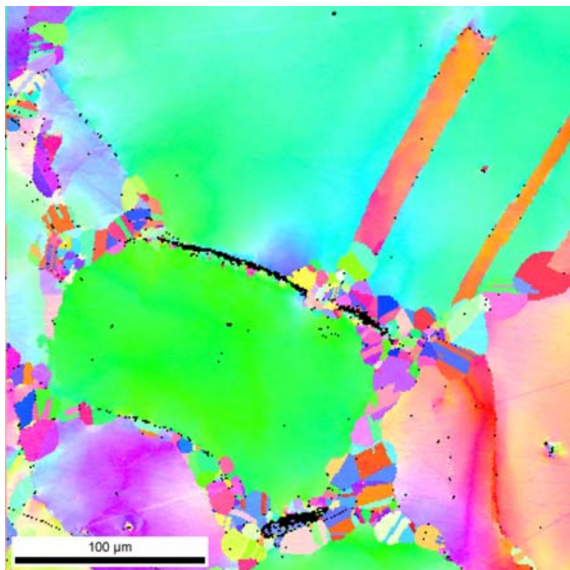

step 10

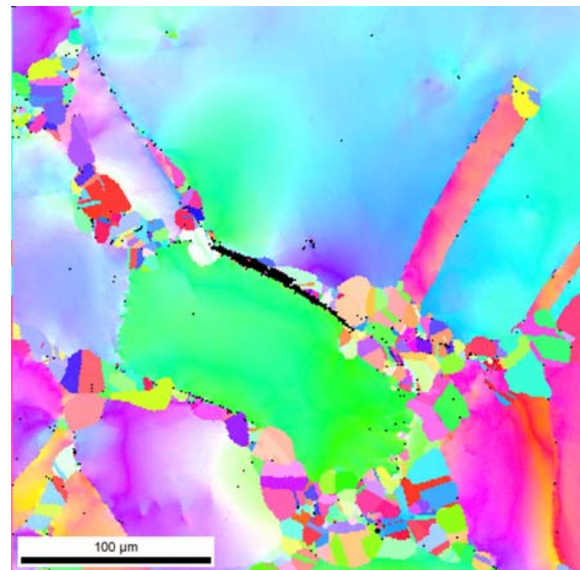

step 11: -7.1 µm

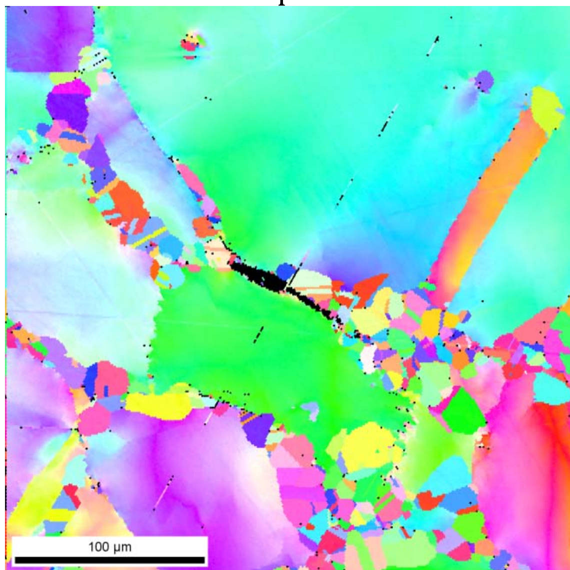

step 12 -3.9 µm

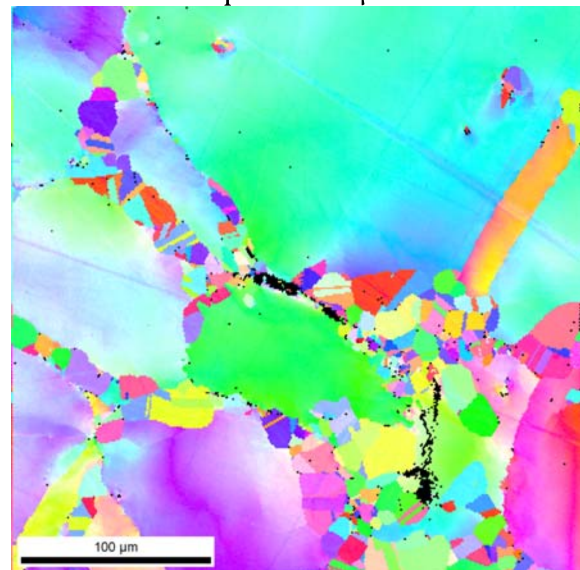

step 13: -1.9 µm

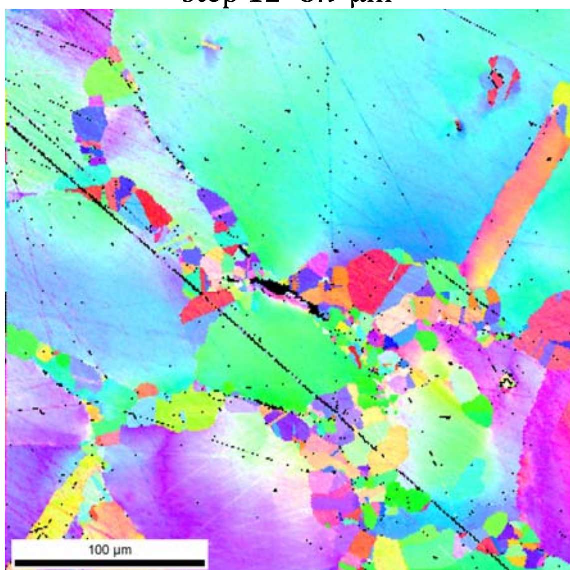

step 14 -1.1 µm

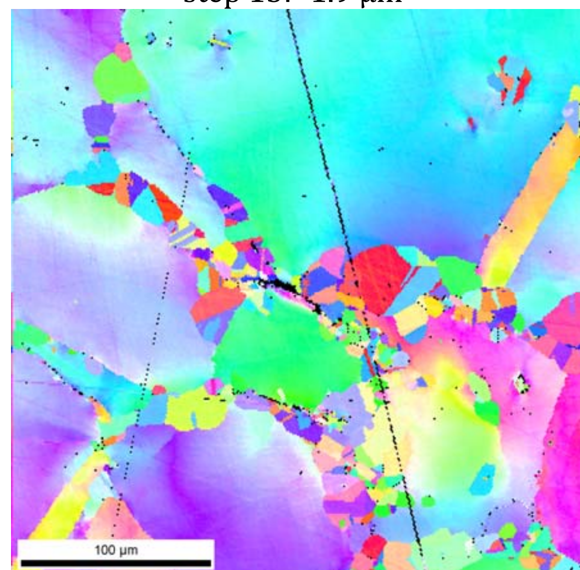

step 15: -1.6 µm

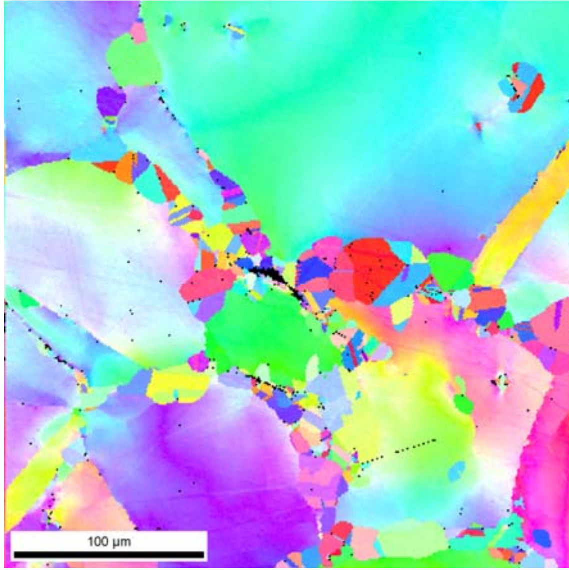

step 16 -2.3 µm

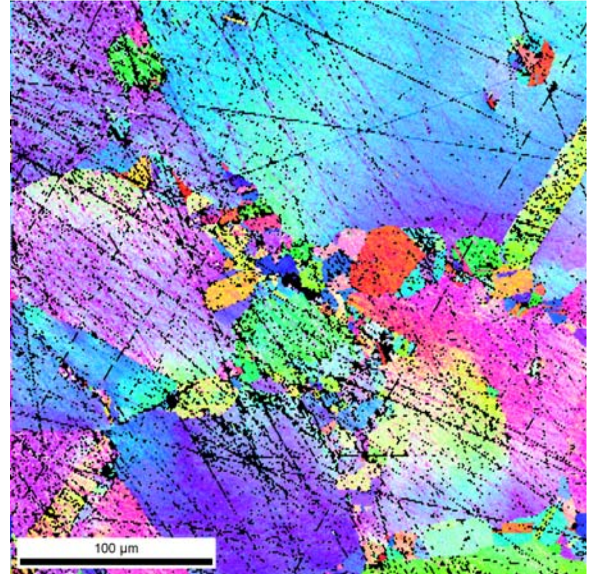

step 17: -1.1 µm

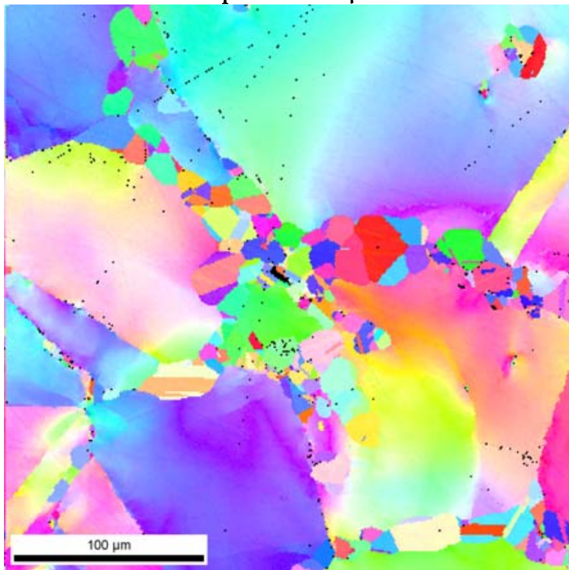

step 18 -2.5 µm

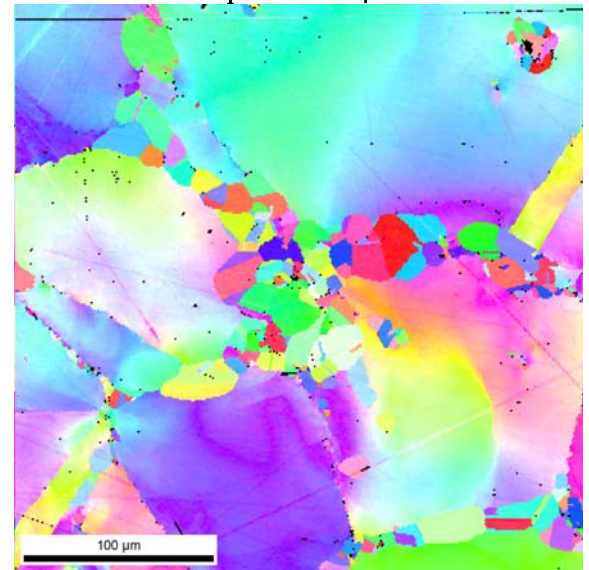

step 19: -2.3 µm

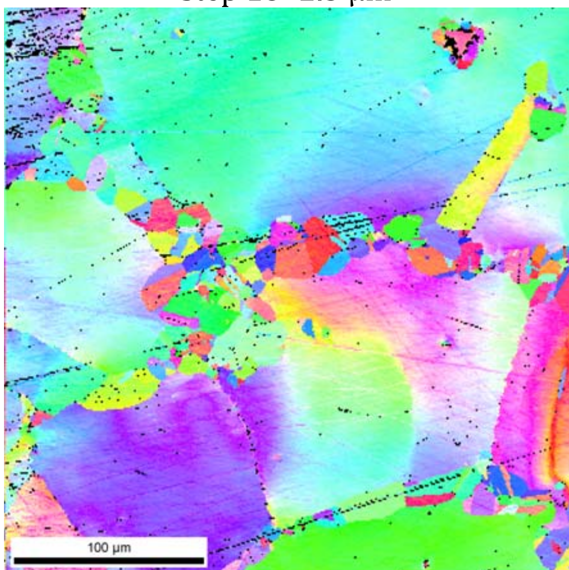

step 20: -1.0 µm